Title
THEORETICAL AND OBSERVATIONAL ANALYSIS OF INDIVIDUAL IONIZING PARTICLE EFFECTS IN BIOLOGICAL TISSUE.

Permalink
https://escholarship.org/uc/item/9rq2758v

Author
Nelson, Alan Caril

Publication Date
1980-11-01

Fish card missing

LBL-11147 Rev.
c.2

Lawrence Berkeley Laboratory
UNIVERSITY OF CALIFORNIA

THEORETICAL AND OBSERVATIONAL ANALYSIS OF INDIVIDUAL IONIZING PARTICLE EFFECTS IN BIOLOGICAL TISSUE

Alan Caril Nelson
(Ph.D. thesis)

November 1980

Donner Laboratory

Biology & Medicine Division

LBL-11147 Rev.
c.2

Prepared for the U.S. Department of Energy under Contract W-7405-ENG-48

Theoretical and Observational Analysis of Individual Ionizing Particle Effects in Biological Tissue

by

Alan Caril Nelson

Lawrence Berkeley Laboratory
University of California
Berkeley, CA 94720

I warmly dedicate this dissertation to

Sharon Everson

the uncertified genius who made
this episode of life a joy
and an accomplishment.

TABLE OF CONTENTS

List of Data Tables

Main Body

LIST OF FIGURES

Main Body

Appendix A

ACKNOWLEDGMENTS

It is my pleasure to show appreciation to those who were of greatest assistance in my graduate program at Berkeley and who more importantly share with me a quality of friendship that is enduring.

Professor Cornelius Tobias was most instrumental in my current success and is largely responsible for shaping my professional life. I still feel like the hours between 5 and 7 p.m. are reserved for our conversations though I do not know how he finds the time.

Professor Tom Hayes can be blamed for converting me from geophysics to biophysics, a decision I have never regretted. His kindness and amiability kept me from growing cynical about graduate work.

Professor Ed Alpen was outspoken and principled with me. It is important to have at least one frank person to keep one alert. I listened closely to his wisdom.

Professor Alex Nichols drew me out and allowed me to talk freely. I often found myself in his office when my spirits needed boosting.

Professor Owen Chamberlain had the patience to wade through my mathematics step by step. His input made my work more professional.

In classes we took together I knew Carl Perez as "the competition." Since I got to know him I discovered a person whose generosity toward friends is astounding. Carl's high energy level keeps me awake.

Chris Cullander and Greg Hook are two completely different people with whom I share a similar rapport of constant good humor. If not for humor I would be inclined toward melancholia.

I want to thank Marilyn Nichols and Elena Vasquez who made the biophysics program a fine place to be.

Without the cheerful and patient help of Diana Morris, this dissertation would not have been completed so handsomely or on schedule.

This work was supported in part by the U. S. Department of Energy under Contract No. W-7405-ENG-48. The author was an NIH trainee during his entire graduate program in biophysics.

Theoretical and Observational Analysis of Individual Ionizing Particle Effects in Biological Tissue

Alan Caril Nelson

Lawrence Berkeley Laboratory
University of California
Berkeley, California 94720

Abstract

This investigation was conducted in an effort to gain a deeper understanding of the microstructural damage to living tissue caused by heavy ion radiation. Preliminary tests on rat corneal tissue, rat cerebellar tissue grown in culture, and rat retinal tissue indicated that of these three tissues the best assay for heavy ion damage might be the rat cornea. The anterior surface of the cornea consists of squamous epithelial cells whose plasma membrane morphology is readily characterized under high resolution scanning electron microscopy (SEM). Thus any structural changes leading to alterations in corneal morphology should be relatively easy to detect if they are within the resolution capability of the SEM. Prior to this work, biological lesions caused by ionizing radiation were almost never observed shortly after a dose was delivered even if the dose was lethal.

The corneal tissue of the living rat was exposed to various charged particle beams at different energies. These included beams of carbon at 474 MeV/amu, neon at 8.5 MeV/amu, argon at 8.5 MeV/amu, iron at 500 MeV/amu, and iron at 600 MeV/amu. The heavy ions were accelerated by the Lawrence Berkeley Laboratory 88" Cyclotron, Super Hilac, and Bevalac. Additionally, x-rays were used on corneas to compare with

the heavy ion irradiated corneas. In all, 84 cornea samples were irradiated with heavy ions, 50 samples were irradiated with x-rays, and 52 samples were non-irradiated controls.

A chemical fixation protocol was developed to crosslink the membrane proteins within a few seconds post-irradiation. The samples were then subjected to graded ethanol dehydration and liquid carbon dioxide critical point drying. All cornea samples were treated identically in preparation for microscopy.

Scanning electron microscopy of corneal epithelium revealed some provoking features of heavy ion irradiation of the tissue. Lesions with circular symmetry were found to occur on the external plasma membranes of corneal epithelium which had been irradiated with heavy ions, but similar lesions were not observed on the plasma membranes of x-ray irradiated or non-irradiated control samples. These data yield experimental verification of the special way in which heavy ions interact with matter: each ion interacts coulombically with electrons all along its trajectory to generate a track. The dose from heavy ion radiation is not distributed homogeneously on a tissue microstructural scale but is concentrated along the individual particle track with regions between separate tracks which receive relatively little dose. Even along a single particle track the dose is discontinuous except at the Bragg peak when the LET is maximum.

The scanning electron micrographs of heavy ion irradiated corneas demonstrated two significant correlations with the heavy ion beam:

1. The average number of plasma membrane lesions per unit area of cornea surface was correlated with the particle fluence of the beam.
2. The diameters of the plasma membrane lesions were nearly linearly related to the energy loss or LET of the individual particle at the cornea surface.

These observations corroborate what has already been suggested theoretically about heavy ion tracks and what has been shown experimentally through etched plastics, developed emulsions, and bubble chambers. But the new data indicate that particle tracks occur in biological tissues as well, and that a single heavy ion is responsible for each membrane lesion.

This kind of information will help guide our thinking on heavy ion interactions with biological tissues and perhaps lead to a more fundamental understanding of the nature of cell damage and cell killing by heavy ion irradiation.

I. FORWARD AND MOTIVATION

Heavy ion beams may eventually supplant the more traditional x-ray and γ-ray beams in various radiographic and therapeutic medical applications. An advantage of the heavy ion beam in radiography is that it is more sensitive to electron density than the photon beam, and this attribute becomes particularly important in attempting to distinguish between adjacent tissues which display only subtle differences in composition (Tobias, et al, 1978). For therapy the heavy ion beam transfers energy to surrounding tissue along the so called "Bragg curve" which means that proportionately more dose is delivered at depth in the tissue relative to the tissue surface (Tobias, et al, 1979a). This is in contrast to the generally exponential energy transfer characteristic of photon beams which deliver a maximum dose closer to the tissue surface than at depth in the tissue (Chase and Rabinowitz, 1967). Heavy ion treatment of localized tumors, for example, can be achieved with less dose to normal tissue and consequently lower associated morbidity (Tobias, et al, 1979a). But dose is a macroscopic unit of energy absorption and assumes that energy is distributed homogeneously in a given volume increment. This assumption is not suitable for photon radiation at a microscopic level, and for heavy ion radiation it is an even more misleading measure of energy deposition (Brandt and Ritchie, 1974). And since the ionization along the trajectory of a heavy ion can be extremely dense (Fleischer, et al, 1975), creating a very high dose in a small local volume, one might expect the mechanisms for cell damage and subsequent cell death by heavy ions to differ markedly from those associated with photon radiation on a microscopic scale. Hence, I have undertaken to explore whether, in a general way, heavy ions are capable of creating lesions in cell plasma membranes and to determine whether lesions are characteristic of heavy ion irradiation. With the insights gained from this investigation, I hope to facilitate a more lucid understanding of heavy ion damage to living tissue.

II. INTRODUCTION AND ORIENTATION

The principle goal of this research is to illustrate that relativistic charged particles of mass greater than or equal to a proton mass, termed "heavy ions," are capable of generating plasma membrane lesions which can be detected with high resolution scanning electron microscopy. The membrane lesions will be characterized in terms of their size, shape, and number per unit area of membrane surface, and these characteristics will be correlated with the nature of the irradiating heavy ion beam. The emphasis throughout the experimentation is on microscopic morphological alterations of the plasma membrane surface at approximately ten seconds post-irradiation, the earliest sampling time I have been able to achieve.

Several experimental difficulties are immediately evident. The theoretical approach developed in the next section does not predict the occurrence of physical membrane lesions as such but merely describes an initial average energy deposition along the heavy ion trajectory. The trail of ionization in the wake of a passing particle is termed the "track," and heavy ion tracks may be only a few nanometers in diameter (Brandt and Ritchie, 1974; Magee and Chatterjee, 1977). The limit of resolution for a standard scanning electron microscope is about ten nanometers point to point (Hayes, 1973) which would seem to be inadequate for the detection of heavy ion tracks in matter. Furthermore, the theoretical development does not guarantee that dense ionization along a particle track will give rise to a morphological alteration in the irradiated material. Since heavy ion tracks may persist no longer than a microsecond in diffusible media (Magee and Chatterjee, 1980), one can expect to visualize the track at a later time, about ten seconds for this work, only if there remains some relatively irreversible damage.

Finally, the biological tissue selected for observation should be uncomplicated enough to expedite the observation of this irreversible radiation damage if such damage is within the resolving power of the scanning electron microscope.

Each of these difficulties is dealt with in successive sections to yield a protocol which permits one to view the microscopic heavy ion track in an irradiated tissue. An analysis of the data will significantly shape our comprehension of biological tissue damage due to heavy ion radiation.

III. HISTORICAL PERSPECTIVE

A. Theoretical Developments

1. Coulombic Interactions

Several scientists have made significant contributions to the theory of charged particle interactins with matter, but four individuals in particular have had major impact on this branch of atomic physics; they are Earnest Lord Rutherford, Neils Bohr, Hans Bethe, and Felix Bloch. Toward the end of the nineteenth century Rutherford had put forward his theory for the elastic scattering of charged particles, alpha rays, about target nuclei (Rutherford, 1906a, 1906b). The particles were found to follow hyperbolic orbits around charge centers whose interaction force was purely coulombic. From this geometrical analysis, Rutherford then derived the differential cross section for elastic scattering by coulombic forces, and this became the cornerstone of the theory for energy loss of a heavy ion passing through matter. One of Rutherford's students, Neils Bohr, took up the challenge to explain why Rutherford's scatter formula did not perfectly fit the scatter data. By 1915 Bohr had published a major series of articles which clarified the problem of elastic scattering by coulombic forces and gave rise to the early non-relativistic form of the energy loss equation (Bohr, 1913a, 1913b, 1915). Several years later Bethe added the fine touches of relativity to the energy loss equation (Bethe, 1930; Segré, 1959) and along with Bloch (Bloch, 1933a, 1933b; Segré, 1959) corrected the expression to its current detailed form. The Bethe/Bloch energy loss equation, as it is now called, is the best formulation available to quantitatively describe the amount of energy transferred by a moving charged particle to surrounding matter (Williams, 1945; Segré, 1959). Unfortunately, the Bethe/Bloch equation is technically valid only at the instant of physical energy deposition; this is an extremely rapid process occurring in less than 10^{-16} seconds (Brandt and Ritchie, 1974). Of course, if one is interested in learning about the effects of this initial energy deposition on biological tissues, one must consider the entire range of time from 10^{-16} seconds to about 10^{7} seconds. No single theory even approximates the course of events over such an enormous time scale, and except for some models which are relevant in the microsecond diffusion rate domain, the time parameter does not enter into the physical formulations. This report does not attempt to supply information regarding changing events in time but rather looks closely at the single time period of ten seconds after the initial deposition of energy in biological tissue.

It will be instructive to carry through the derivation of the energy loss expression starting, as Rutherford did, with a consideration of elastic scattering. This requires some basic principles regarding the equation of a hyperbola in rectangular and polar coordinates which are presented in Appendix A. Also in Appendix A are Figs. A1 and A2 which define the notation used throughout this section.

Let us consider the elastic interaction of two charged particles, one of mass M and charge Ze located at the origin of a polar coordinate system as shown in Fig. A2 of Appendix A, and the other of mass m and charge ze moving with some velocity V. In the direction of increasing r and increasing θ, the components of the vector velocity are

$$v_r = \frac{dr}{dt} \text{ and } v_\theta = r\frac{d\theta}{dt} \tag{1}$$

where v_r is the radial component and v_θ is the angular component. The acceleration vector can also be represented by its radial and angular components as

$$a_r = \frac{d^2r}{dt^2} - r\left(\frac{d\theta}{dt}\right)^2 \tag{2}$$

where the term $-r\left(\frac{d\theta}{dt}\right)^2$ is called the centripetal acceleration, and

$$a_\theta = r\frac{d^2\theta}{dt^2} + 2\left(\frac{dr}{dt}\right)\left(\frac{d\theta}{dt}\right) = \frac{1}{r}\frac{d}{dt}\left(r^2\frac{d\theta}{dt}\right) \tag{3}$$

where the term $2\left(\frac{dr}{dt}\right)\left(\frac{d\theta}{dt}\right)$ is called the Coriolis acceleration (Evans, 1955).

Because the entire force of the coulombic central force system is directed along r, the angular component of the acceleration, equation (3), must be zero

$$a_\theta = \frac{1}{r}\frac{d}{dt}\left(r^2\frac{d\theta}{dt}\right) = 0 \quad ,$$

and this implies that

$$d\left(r^2 \frac{d\theta}{dt}\right) = 0 \quad . \tag{4}$$

Integration of equation (4) yields

$$r^2 \frac{d\theta}{dt} = C_1 \tag{5}$$

where C_1 is a constant of integration. The coulombic force between the two particles will be

$$F = \frac{(ze)(Ze)}{r^2}\left(\frac{M}{m+M}\right)^2 = \frac{zZe^2}{r^2}\left(\frac{M}{m+M}\right)^2 \quad , \tag{6}$$

and the force will be attractive if negative and repulsive if positive. Here the unit of electrical charge e is in esu. The radial component of acceleration along r of the particle m is

$$a_r = \frac{F}{m} = \frac{zZe^2}{mr^2}\left(\frac{M}{m+M}\right)^2 \quad , \tag{7}$$

and we remember from above that the angular component of acceleration is zero. Equation (2) and equation (7) can now be combined to give

$$\frac{d^2r}{dt^2} - r\left(\frac{d\theta}{dt}\right)^2 = \frac{zZe^2}{mr^2}\left(\frac{M}{m+M}\right)^2 \quad . \tag{8}$$

The motion of particle m is restricted according to equations (5) and (8), and it is necessary to eliminate the time variable t between these expressions in order to write the equation of the particle trajectory in terms of r and θ alone. To simplify matters we will take advantage of the substitution (Evans, 1955)

$$r \equiv \frac{1}{\mu} \quad .$$

With this substitution, equation (5) becomes

$$\frac{d\theta}{dt} = C_1\mu^2 \quad . \tag{9}$$

We can further write

$$\frac{dr}{dt} = \frac{d}{dt}\left(\frac{1}{\mu}\right) = \frac{-1}{\mu^2}\left(\frac{d\mu}{dt}\right) = \frac{-1}{\mu^2}\left(\frac{d\mu}{d\theta}\right)\left(\frac{d\theta}{dt}\right) \quad . \tag{10}$$

Substituting equation (9) into equation (10) gives

$$\frac{dr}{dt} = \frac{-1}{\mu^2}\left(\frac{d\mu}{d\theta}\right) C_1\mu^2 = -C_1\left(\frac{d\mu}{d\theta}\right) \quad . \tag{11}$$

The second derivative of equation (11) is

$$\frac{d^2r}{dt^2} = -C_1\left(\frac{d^2\mu}{d\theta^2}\right)\left(\frac{d\theta}{dt}\right) = -C_1{}^2\mu^2\left(\frac{d^2\mu}{d\theta^2}\right) \tag{12}$$

after substituting in equation (9) again. Looking back at equation (8) we can conveniently insert equation (12), make the substitution $r = 1/\mu$ where needed, and also insert equation (9) to yield

$$-C_1{}^2\mu^2\left(\frac{d^2\mu}{d\theta^2}\right) - \frac{1}{\mu}\left(C_1{}^2\mu^4\right) = \mu^2\,\frac{zZe^2}{m}\left(\frac{M}{m+M}\right)^2 \quad , \tag{13}$$

and upon simplification this becomes

$$\frac{d^2\mu}{d\theta^2} + \mu = \frac{-zZe^2}{C_1{}^2 m}\left(\frac{M}{m+M}\right)^2 \quad . \tag{14}$$

Equation (14) is the sought after differential equation which describes the motion of particle m in the coulombic force system. The solution to this equation is easily obtained (Spiegel, 1967) in terms of trigonometric functions as

$$\mu = \frac{1}{r} = -\frac{zZe^2}{C_1{}^2 m}\left(\frac{M}{m+M}\right)^2 + C_2\cos(\theta - \theta_o) \tag{15}$$

where C_2 and θ_o are constants of integration. Now inverting equation (15) to solve explicitly for r gives

$$r = \frac{-mC_1{}^2}{zZe^2\left(\frac{M}{m+M}\right)^2 - mC_1{}^2C_2\cos(\theta - \theta_o)} \quad . \tag{16}$$

If the numerator and denominator of equation (16) are multiplied by

$\frac{1}{zZe^2}\left(\frac{m+M}{M}\right)^2$ we obtain the form

$$r = \frac{\left(\frac{-mC_1^{\,2}}{zZe^2}\right)\left(\frac{m + M}{M}\right)^2}{1 - \left(\frac{mC_1^{\,2}C_2}{zZe^2}\right)\left(\frac{m + M}{M}\right)^2\cos(\theta - \theta_0)} \quad . \tag{17}$$

Equation (17) is the equation of an hyperbola as can be verified by comparing it to equations (A14) and (A15) in Appendix A. We can immediately write the eccentricity as

$$\varepsilon = \frac{mC_1^{\,2}C_2}{zZe^2}\left(\frac{m + M}{M}\right)^2 , \tag{18}$$

and because the smallest value of r occurs at $\theta = 0$ we must have $\theta_0 = 0$. From equation (18) we have

$$(1 - \varepsilon^2) = 1 - \left[\frac{mC_1^{\,2}C_2}{zZe^2}\left(\frac{m + M}{M}\right)\right]^2 , \tag{19}$$

and this will help us determine the value of the constant a in equations (A14) and (A15). We can observe from the numerator of equation (17) that

$$a(1 - \varepsilon^2) = \left(\frac{-mC_1^{\,2}}{zZe^2}\right)\left(\frac{m + M}{M}\right)^2 , \tag{20}$$

and solving explicitly for a gives

$$a = \left(\frac{-mC_1^{\,2}}{zZe^2(1-\varepsilon^2)}\right)\left(\frac{m + M}{M}\right)^2 \quad . \tag{21}$$

Substituting equation (19) into the denominator of equation (21) gives

$$a = \left(\frac{-mC_1^{\,2}}{zZe^2}\right)\left(\frac{m + M}{M}\right)^2 \quad \frac{1}{1 - \left[\frac{mC_1^{\,2}C_2}{zZe^2}\left(\frac{m + M}{M}\right)^2\right]^2}$$

and with some simplification yields finally

$$a = \frac{mC_1^{\,2}zZe^2M^2(m + M)^2}{(mC_1^{\,2}C_2)^2(m + M)^4 - (zZe^2)^2M^4} \quad . \tag{22}$$

Having defined $a(1-\varepsilon^2)$ in equation (20) with the formula for a in equation (22) and the formula for ε in equation (18), we can write equation (17) in the form which is identical to equation (A14)

$$r = \frac{a(1 - \varepsilon^2)}{1 - \varepsilon\cos\theta} \quad .$$

This proves that the trajectory of charged particle m follows an hyperbolic path during an elastic collision with another charged particle M when the only force involved is coulombic (Evans, 1955).

We shall now introduce two additional parameters for the collision of two particles. First, the collision diameter b is defined by the equation

$$b = \frac{2\,|zZ\,|e^2}{V^2}\left(\frac{m + M}{mM}\right) \qquad (23)$$

where V is the velocity of particle m. This is simply the ratio of charges to particle kinetic energy in the reduced mass system.

Second, the impact parameter x, shown in Fig. A2 of Appendix A, is defined as the closest distance that would be achieved between the two approaching particles if no interaction forces existed. The angular momentum J of the two particle system is constant (Blass, 1962), since no external torques act on the system. Thus we can write

$$J = \frac{mMxV}{(m + M)} \qquad (24)$$

where x is the impact parameter (Evan, 1955). The moment of inertia of the system is given by (Fowles, 1962)

$$I = -r^2 m^2\left(\frac{m + M}{mM}\right) \quad . \qquad (25)$$

The angular velocity dθ/dt when multiplied by the moment of inertia I will yield the angular momentum (Blass, 1962)

$$J = I\left(\frac{d\theta}{dt}\right) = -r^2 m^2\left(\frac{m + M}{mM}\right)\left(\frac{d\theta}{dt}\right) \quad . \qquad (26)$$

Now we can equate equations (24) and (26) and rearrange to give

$$r^2\left(\frac{d\theta}{dt}\right) = -\left(\frac{Vx}{m^2}\right)\left(\frac{mM}{m + M}\right)^2 = -\,Vx\left(\frac{M}{m + M}\right)^2 \quad . \qquad (27)$$

From equation (5) we see that equation (27) can be written

$$C_1 = -Vx \left(\frac{M}{m + M}\right)^2 \quad . \tag{28}$$

For the instantaneous velocity v we take the sum of the squares of the radial and angular components given by equation (1)

$$v^2 = v_r{}^2 + v_\theta{}^2 = (\frac{dr}{dt})^2 + (\frac{rd\theta}{dt})^2$$

$$= (\frac{dr}{d\theta})^2 \; (\frac{d\theta}{dt})^2 + r^2(\frac{d\theta}{dt})^2 = \left[(\frac{dr}{d\theta})^2 + r^2\right] (\frac{d\theta}{dt})^2 \quad . \tag{29}$$

If we differentiate equation (16) with respect to θ, with $\theta_0 = 0$, and substitute that expression for $dr/d\theta$ into equation (29) and use equation (9) for $d\theta/dt$ we get finally

$$v^2 = \frac{C_1{}^2}{r^2} + C_1{}^2 C_2{}^2 \sin^2\theta \quad . \tag{30}$$

Recall that the potential energy of the coulombic force system is (Richtmyer, et al, 1969)

$$PE = \frac{zZe^2M}{r(m + M)} \quad . \tag{31}$$

Conservation of energy dictates that the sum of the potential energy and the particle kinetic energy at any instant will equal the initial kinetic energy

$$\frac{1}{2}\, mV^2\left(\frac{M}{m + M}\right) = \frac{zZe^2}{r}\left(\frac{M}{m + M}\right) + \frac{1}{2}mv^2\left(\frac{m + M}{M}\right) \quad .$$

Or by rearranging terms

$$V^2\left(\frac{M}{m + M}\right)^2 = \frac{2zZe^2}{rm}\left(\frac{M}{m + M}\right)^2 + v^2$$

and now using equation (30) for v^2 and substituting into the above yields

$$V^2\left(\frac{M}{m + M}\right)^2 = \frac{2zZe^2}{rm}\left(\frac{M}{m + M}\right)^2 + \frac{C_1^{\,2}}{r^2} + C_1^{\,2}C_2^{\,2}\sin^2\theta \quad . \tag{32}$$

We substitute equation (16) for r into equation (32) and simplify to get

$$V^2\left(\frac{M}{m + M}\right)^2 = C_1^{\,2}C_2^{\,2} - \left[\frac{zZe^2}{mC_1}\left(\frac{M}{m + M}\right)^2\right]^2 \quad . \tag{33}$$

The importance of this equation is that it is independent of r and θ and expresses the integration constant C_2 in terms of other constants of the system. Let us solve equation (33) for C_2 explicitly

$$C_2 = \frac{1}{C_1}\left(\frac{M}{m + M}\right)\left[V^2 + \frac{1}{C_1^{\,2}}\left(\frac{zZe^2}{m}\right)^2\left(\frac{M}{m + M}\right)^2\right]^{1/2} \quad . \tag{34}$$

With equation (28) for C_1 and equation (34) for C_2 to enter back into equation (17), we have completely solved the two particle problem (Evans, 1955).

We are now prepared to solve equation (18) for the eccentricity simply by inserting equations (28) and (34) to yield

$$\varepsilon = \left[V^2 \left(\frac{mVx}{zZe^2} \right)^2 \left(\frac{M}{m + M} \right)^2 + 1 \right]^{1/2} , \qquad (35)$$

and furthermore

$$\varepsilon = \left[\left(\frac{2x}{b} \right)^2 + 1 \right]^{1/2} \qquad (36)$$

when the collision diameter b is defined as in equation (23). Equation (36) can be rewritten as

$$\varepsilon^2 - 1 = \left(\frac{2x}{b} \right)^2 . \qquad (37)$$

Notice the location of angle Θ between the two asymptotes shown in Fig. A2 of Appendix A. The angle Θ is called the deflection angle (Evans, 1955) and is given by

$$\Theta = \pi - 2\theta_\infty \text{ or } \theta_\infty = \frac{\pi}{2} - \frac{\Theta}{2} , \qquad (38)$$

and taking the cosine of both sides gives

$$\cos\theta_\infty = \cos\left(\frac{\pi}{2} - \frac{\Theta}{2} \right) = \sin \frac{\Theta}{2} . \qquad (39)$$

Substituting equation (A16) into equation (39) leaves

$$\frac{1}{\varepsilon} = \sin\left(\frac{\Theta}{2}\right) \quad \text{or} \quad \varepsilon = \csc\left(\frac{\Theta}{2}\right) \quad ,$$

and then squaring both sides and subtracting 1 provides

$$\varepsilon^2 - 1 = \csc^2\left(\frac{\Theta}{2}\right) - 1 = \cot^2\left(\frac{\Theta}{2}\right) \quad . \tag{40}$$

Equation (40) is an alternative general equation of an hyperbola. A comparison of equations (37) and (40) leads to

$$\left(\frac{2x}{b}\right)^2 = \cot^2\left(\frac{\Theta}{2}\right) \quad ,$$

and upon simplification and solving for x we have

$$x = \frac{b}{2}\cot\left(\frac{\Theta}{2}\right) \quad . \tag{41}$$

We are now prepared to write the expression for the cross section for elastic scattering by coulombic forces as established by Rutherford (Rutherford, 1906a, 1906b). The differential cross section of particle m being scattered by particle M for an impact parameter between x and x + dx is just the area of the ring of radius x and width dx (Evans, 1955). Thus,

$$d\sigma = 2\pi x dx \quad . \tag{42}$$

Equation (41) with its derivative can be substituted into equation (42) to give

$$d\sigma = 2\pi \left[\frac{b}{2} \cot\left(\frac{\Theta}{2}\right)\right] \frac{b}{2} \csc^2\left(\frac{\Theta}{2}\right) \frac{d\Theta}{2}$$

which can be simplified to yield

$$d\sigma = \frac{\pi b^2}{4} \frac{\cos(\Theta/2)}{\sin^3(\Theta/2)} d\Theta \quad . \qquad (43)$$

Equation (43) is one form of the Rutherford formula for elastic scatter by coulombic forces (Evans, 1955; Richtmyer, et al, 1969).

We are ready to discuss the energy transfer which occurs as particle m passes into a medium of coulomb scatter centers each of mass M. During a collision, the particle M will be given a velocity V' if it is initially at rest and unbound. The kinetic energy of the struch particle M will equal the kinetic energy lost by the striking particle m and will be

$$Q = \frac{1}{2} MV'^2 \quad . \qquad (44)$$

Referring again to Fig. A2 and applying the law of cosines for the velocities we have

$$V'^2 = 2V^2 \left(\frac{m}{m + M}\right)^2 (1 - \cos\Theta) = 4V^2 \left(\frac{m}{m + M}\right)^2 \sin^2 \left(\frac{\Theta}{2}\right) \quad . \qquad (45)$$

Substituting equation (45) into equation (44) gives

$$Q = 2MV^2 \left(\frac{m}{m + M}\right)^2 \sin^2\left(\frac{\Theta}{2}\right). \qquad (46)$$

The differential of equation (46) is

$$dQ = 2MV^2 \left(\frac{m}{m + M}\right)^2 \sin\left(\frac{\Theta}{2}\right) \cos\left(\frac{\Theta}{2}\right) d\,\Theta \quad . \tag{47}$$

Let us solve equation (47) for the cosine term

$$\cos\left(\frac{\Theta}{2}\right) d\,\Theta = \frac{dQ}{2MV^2\left(\frac{m}{m + M}\right)^2 \sin\left(\frac{\Theta}{2}\right)} \quad , \tag{48}$$

and we can solve equation (46) for the sine term

$$\sin^2\left(\frac{\Theta}{2}\right) = \frac{Q}{2MV^2\left(\frac{m}{m + M}\right)^2} \quad . \tag{49}$$

If we use the quantities expressed in equations (48) and (49) in the differential cross section equation (43) we get

$$d\sigma = \frac{\pi b^2}{4}\left[2MV^2\left(\frac{m}{m + M}\right)^2\right]\frac{dQ}{Q^2} \quad , \tag{50}$$

and recalling the definition of the collision diameter b from equation (23), we can write equation (50) as

$$d\sigma = \frac{2\pi z^2 Z^2 e^4}{MV^2}\,\frac{dQ}{Q^2} \quad . \tag{51}$$

A frequently employed form for equation (51) pertains to the case of electrons being scattered by the moving particle. In this case $M = m_0$ and $Z = 1$ so that

$$d\sigma = \frac{2\pi z^2 e^4}{m_o V^2} \frac{dQ}{Q^2} \qquad \text{cm}^2/\text{electron} \tag{52}$$

and this is a most important result.

After Rutherford's pioneering work, his friend Bohr carried the theory to the next important level (Bohr, 1913a). Bohr derived the original energy loss expression for a charged particle traveling along a trajectory x. Here "x" refers to a line in space and not the Rutherford impact parameter mentioned earlier.

Equation (52) is the differential cross section per electron. In order to write the differential cross section per atom, we realize that for a neutral atom there are Z electrons. Furthermore, if we say there are N atoms per cubic centimeter of target material, then the quantity NZ is the number of electrons per cubic centimeter. When the quantity NZ in multiplied into equation (52) we get units of inverse centimeters, and this operation converts equation (52) into a different cross section which is interpreted as the change in the number of interaction events per increment of distance (Setlow and Pollard, 1962)

$$d\sigma = d\left(\frac{dn}{dx}\right) = \frac{2\pi z^2 e^4}{m_o V^2} NZ \frac{dQ}{Q^2} \quad . \qquad \text{cm}^{-1} \tag{53}$$

Since Q is the amount of energy transferred per event, then the quantity d(dn/dx) represents the rate of energy transfers per unit path length. To express the rate of energy lost by the striking particle we simply multiply both sides of equation (53) by the energy lost per event Q to yield

$$Qd\left(\frac{dn}{dx}\right) = \frac{2\pi z^2 e^4}{m_o V^2} NZ \frac{dQ}{Q} \quad . \qquad \frac{\text{energy per event}}{\text{cm}} \tag{54}$$

To obtain the total incremental energy lost per unit path length we integrate equation (54) from some minimum energy transfer per event Q_{min} to some maximum energy transfer per event Q_{max} to get a more familiar expression

$$\begin{aligned} \frac{-dE}{dx} &= \int_{Q_{min}}^{Q_{max}} Qd\left(\frac{dn}{dx}\right) = \int_{Q_{min}}^{Q_{max}} \frac{2\pi z^2 e^4}{m_o V^2} NZ \frac{dQ}{Q} \\ &= \frac{2\pi z^2 e^4}{m_o V^2} NZ \int_{Q_{min}}^{Q_{max}} \frac{1}{Q}\, dQ = \frac{2\pi z^2 e^4}{m_o V^2} NZ \ln\left(\frac{Q_{max}}{Q_{min}}\right) \quad . \end{aligned} \tag{55}$$

The maximum energy transfer per event is just (Richtmyer, et al, 1969)

$$Q_{max} = \frac{2m_o M^2 V^2}{(m_o + M)^2} \tag{56}$$

where M is the mass of the striking particle. If the striking particle happens to be an electron ($M = m_o$) then

$$Q_{max} = \frac{1}{2} m_o V^2 \quad . \tag{57}$$

However, if the mass of the striking particle is on the order of a heavy ion ($M >> m_o$) then

$$Q_{max} = 2m_oV^2 \quad . \tag{58}$$

We are most concerned with the energy lost by heavy ions in passing through matter, so equation (58) will serve as our definition of Q_{max}. The minimum energy transfer per event is difficult to determine. Let us write the geometric mean (Setlow and Pollard, 1962; Lyman, 1967) of the minimum and maximum energies transferred per event as

$$I_o^2 = (Q_{min})(2m_oV^2)$$

$$\text{or } Q_{min} = \frac{I_o^2}{2m_oV^2} \quad . \tag{59}$$

Substituting Q_{max} and Q_{min} from equations (58) and (59) into equation (55) we obtain

$$\frac{-dE}{dx} = \frac{2\pi z^2e^4}{m_oV^2} NZ \ln\left(\frac{2m_oV^2}{I_o}\right)^2 = \frac{4\pi z^2e^4}{m_oV^2} NZ \ln\left(\frac{2m_oV^2}{I_o}\right) \quad . \tag{60}$$

Here I_o is the average excitation potential of a target atom and will be discussed later. Equation (60) is often called the Bohr equation for energy loss per unit path length by a particle of charge z moving with velocity V which strikes the target material with an electron density of NZ (Williams, 1945; Evans, 1955). Notice that equation (60) is valid for non-relativistic particles only. Even though Bohr attempted to correct this equation for relativistic particles (Bohr, 1915) he did not quite succeed (Bethe, 1930). The classical energy loss equation (60) is valid however when the de Broglie wavelength of the particle is small compared to the collision diameter b (Evans, 1955) of equation (23)

$$\lambda = \frac{h}{p} = \frac{h}{V}\left(\frac{m + M}{mM}\right) << b = \frac{2zZe^2}{V^2}\left(\frac{m + M}{mM}\right)$$

or by rearranging terms and cancelling

$$V << \frac{2zZe^2}{h} \qquad (61)$$

where h is Plank's constant. Dividing both sides of equation (61) by the velocity of light in vacuum c and lumping some constants $\frac{2\pi e^2}{hc} = \frac{1}{137}$ to substitute into equation (61) we get

$$\beta = \frac{V}{c} << \frac{zZ}{137\pi} \quad . \qquad (62)$$

And for a target of biological material with $Z \cong 7$ and a heavy ion beam of carbon $z = 6$, the Bohr equation (60) will be approximately valid for particle velocities $V << \frac{1}{10}c$.

Before leaving the Bohr equation there remains a feature which provides insight into the way energy is deposited along the particle path. Let us integrate equation (53) directly from a minimum energy transfer Q_{min} to a maximum energy transfer Q_{max}

$$\int_{Q_{min}}^{Q_{max}} d\left(\frac{dn}{dx}\right) = \int_{Q_{min}}^{Q_{max}} \frac{2\pi z^2 e^4}{m_o V^2} NZ \frac{dQ}{Q^2}$$

so that after integrating and rearranging terms we have

$$dn = \frac{2\pi z^2 e^4}{m_o V^2} NZ \left(\frac{1}{Q_{min}} - \frac{1}{Q_{max}}\right) dx \quad . \tag{63}$$

This is an expression for the number dn of energy transfers along the path dx for energy transfers between a minimum Q_{min} and maximum Q_{max}. The insight provided by equation (63) is that low energy transfers are more numerous than high energy transfers (Setlow and Pollard, 1962). This is an important point and will be raised again in the discussion of the structure of energy deposition along a particle path.

The Bohr energy loss equation serves as a good approximation for particles with $\beta < 0.1$, but in many interesting situations we have $\beta > 0.1$ and therefore must use a corrected energy loss equation. The proper formulation for relativistic particles was put forward by Bethe and Bloch independently. Bethe's relativistic equation for energy loss is (Bethe, 1930; Segre, 1959)

$$\frac{-dE}{dx} = \frac{4\pi z^2 e^4}{m_o V^2} NZ \left[\ln\left(\frac{2m_o V^2}{I_o}\right) - \ln(1 - \beta^2) - \beta^2\right] \quad , \tag{64}$$

and we observe that for non-relativistic particles, $\beta^2 \cong 0$, equation (64) reduces exactly to the Bohr equation (60). Bloch's result (Bloch, 1933a, 1933b; Segré, 1959) is by way of a quantum mechanical derivation and can be expressed as

$$\frac{-dE}{dx} = \frac{4\pi z^2 e^4}{m_o V^2} NZ \left[\ln\left(\frac{2m_o V^2}{I_o}\right) + \phi(1) - R\phi\left(1 + i\,\frac{2\pi z e^2}{hV}\right)\right] \qquad (65)$$

where ϕ is the logarithmic derivative of the gamma-function, $R\phi$ denotes the real part of ϕ, and h is Plank's constant. Bloch's equation (65) is the most general expression for energy loss along the particle path and will reduce to Bohr's equation (60) when (Segré, 1959)

$$\frac{2\pi z e^2}{hV} \cong 0.$$

The average excitation potential I_o, sometimes referred to as the mean ionization potential, is a centrally important parameter for the Bohr, Bethe, and Bloch equations for energy loss. Unfortunately, except in the simplest case of hydrogen target atoms it cannot be calculated from first principles (Segré, 1959). But the parameter has been determined experimentally by measuring the energy loss $-dE/dx$ for known velocity particles in a target material of known composition (Kahn, 1953). Then any of equations (60), (64), and (65) can be used appropriately to calculate I_o. For target materials of high Z, Bloch has shown that $I_o \cong kZ$ (Bloch, 1933a, 1933b) where k is an emperical constant whose value is about 11.5 eV (Wheeler and Ladenburg, 1941). Obviously, the average excitation potential I_o has units of energy. The table below displays some measured values of I_o for different target materials (Setlow and Pollard, 1962).

Target Material	I_o, eV
H	16.0
C	64.0
N	81.0
O	99.0
P	165.0

In dealing with target materials which are composed of several elements, no matter how they are chemically bound in molecules, a law known as the Bragg Additive Law simplifies the calculation of energy loss (Setlow and Pollard, 1962). The law states that chemical combinations can be ignored, and an estimate of energy loss can be made as if each atom contributes separately to the total energy loss. Thus, for example, the Bohr equation (60) for a target composed of elements hydrogen (H) and oxygen (Ox), as in water, can be written

$$\frac{-dE}{dx} = \frac{4\pi z^2 e^4}{m_o V^2}\left[N_H Z_H \ln\left(\frac{2m_o V^2}{I_H}\right) + N_{ox} Z_{ox} \ln\left(\frac{2m_o V^2}{I_{ox}}\right)\right], \qquad (66)$$

where the subscripts refer to the particular elements involved. Calculations made in this way can be experimentally tedious but are mathematically straightforward.

When energy from a heavy ion is transferred to the target material, conservation of energy dictates that the particle velocity must decrease. Since V^{-2} varies much more rapidly than $\ln(V^2)$ for large velocities, a glance at any of the energy loss equations will reveal that energy loss per unit path length increases as velocity decreases, and the energy loss per unit path length is approximately proportional to V^{-2}. In order to calculate $-dE/dx$ we typically use an instantaneous velocity in the energy loss equations. But at any instant in time the particle occupies only a point in space, within the limitations imposed by the Heisenberg uncertainty principle $\Delta x \Delta p \geq \hbar$, so that we are really determining the energy loss at a point. In practice $-dE/dx$ represents an average energy loss over some unit distance. To properly calculate $-dE/dx$ as a particle passes through matter, we must know how the particle velocity V is functionally related to the energy lost by the particle in the previous instant. The relativistic functional relationship between particle energy E and its velocity V is given by (Richtmyer, et al, 1969)

$$E = m_o c^2 \left[\left(1 - V^2/c^2 \right)^{-1/2} - 1 \right] \qquad (67)$$

where here m_o is the particle rest mass. By rearranging terms using $c = 3 \times 10^{10}$ cm/sec, expressing energy in MeV, and solving equation (67) for velocity explicitly we obtain

$$V = \left\{9 \times 10^{20} - \frac{2 \times 10^{15}}{\left[\left(E \text{ in MeV}\right)\left(1.602 \times 10^{-6}\right) + 0.0015\right]^{2}}\right\}^{1/2} . \quad (68)$$

With this expression for velocity substituted back into the energy loss equations (60), (64), and (65), we realize that the resulting equations are transcendental and cannot be solved in closed form. Fortunately, several computer programs have been developed to solve the energy loss equations with good accuracy (Williamson and Boujot, 1962; Barkas and Berger, 1964; Berger and Seltzer, 1966; Northcliffe and Schilling, 1970). These programs, to give valid results for lower velocities, must also include a function to describe the changes in particle charge z resulting from increased electron attachment as the particle slows down. This change in effective charge on the heavy ion is given by (Pierce and Blann, 1968)

$$z_{eff} = z \left\{1 - \exp\left[-\frac{0.95h}{2\pi e^{2}}\left(Vz^{-2/3}\right)\right]\right\} \quad (69)$$

where V is the particle velocity, h is Plank's constant, and e is the electron charge. A formulation for an equilibrium charge distribution in the heavy ion beam has also been developed (Nikolaev and Dmitriev, 1968).

The data produced by such calculations are usually presented in tables or, if expressed as $-dE/dx$ vs. particle penetration distance x, can be shown graphically as a Bragg curve. Figure 1 illustrates the important features of a typical Bragg curve. We see that the heavy ions have a definite range or length of the particle track. All along

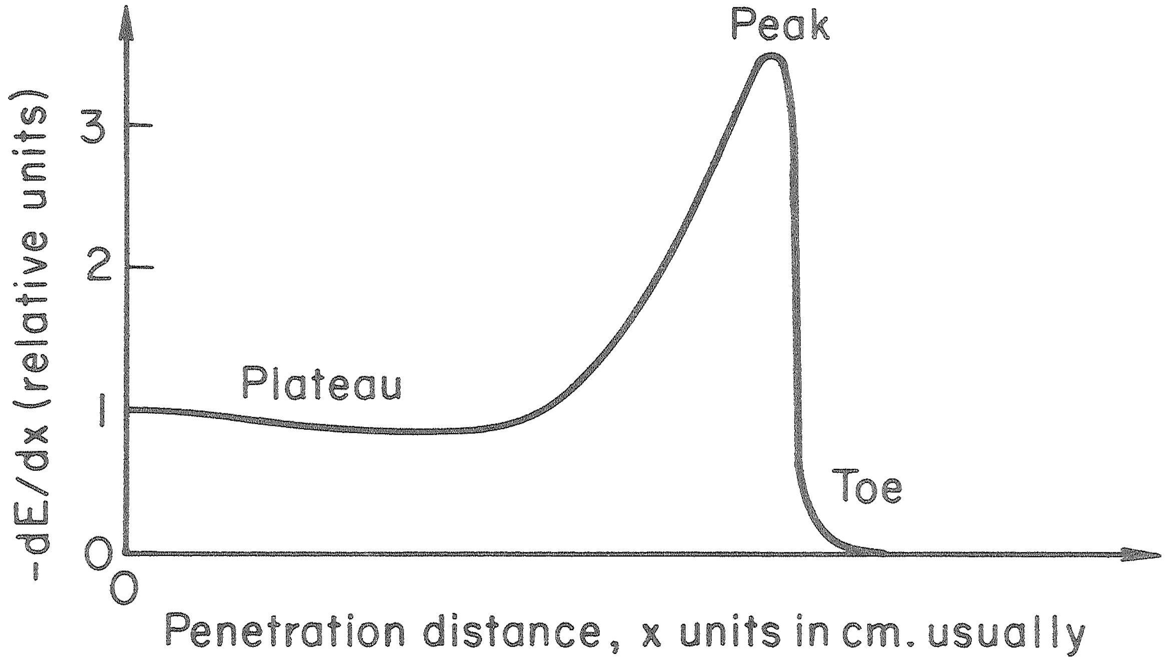

XBL806-3407

Figure 1. An example of a Bragg curve. The energy loss per unit penetration distance changes slowly in the plateau region and is maximum at the peak. The toe region is due mostly to range straggling and beam fragmentation.

the particle track, the energy loss per unit path length is changing. In the plateau region the $-dE/dx$ is changing slowly, and at the Bragg peak it is maximum. The plateau and the peak will be used in this work.

Finally a few remarks on terminology will be beneficial. The term $-dE/dx$ besides being called the energy loss per unit length is also known as the stopping power when expressed in units of MeV cm^2/g or as the linear energy transfer (LET) when expressed in units of keV/μm. The stopping power unit has been divided by the average density of the target material, so to express the linear stopping power in MeV/cm one must multiply by the density of the target material. For water with density = 1 g/cm^3, the stopping power is ten times the LET. In equations (60), (64), and (65) all terms to the right of "N" are lumped together and called the stopping number.

2. Tracks in Condensed Phases

We will use the term "track" to signify in particular the radiation induced structural alterations in target material which have some duration following the passage of swiftly moving charged particles. Whenever a heavy ion loses energy in the target material, there is a possibility that a track will arise. Some established techniques for visualizing particle tracks in different media will be discussed in the following section. In biological material or any fluid like system the structure of particle tracks can be expected to change temporally due in part to diffusion of radiation products (Magee and Chatterjee, 1977, 1980). Track structure will also change when radiation products interact or decay to more stable states. It is the purpose of this research to investigate particle tracks in biological tissue, but first let us examine the nature of particle tracks in a condensed fluid such as water. We assume that water is homogeneous; that is, there are no structures except the configuration of condensed water molecules.

The energy loss equations (60), (64), and (65) would suggest that energy is lost by the charged particle moving through matter in a continuous fashion. This is actually not the case. Energy releases are discrete as we have learned from the atomic theory of matter and quantum mechanics (Gasiorowicz, 1974). In aqueous media the sites of energy release along the particle track are often referred to as spurs and blobs depending on their size, blobs being the larger events (Mozumder and Magee, 1972). Moreover, various experimenters have shown that the average energy released in a primary ionization is about 110 eV and that the spacing between events along the track is on the order of nanometers (Setlow and Pollard, 1962; Mozumder and Magee, 1972). Toward the end of a particle track the distance between events begins to overlap and this generates a cylindrical geometry of track structure (Mozumder and Magee, 1972). Any description of energy deposition will henceforth be referred to as "energy structure."

Within a narrow radius around the particle trajectory we can define a region called the "core" or "infra track" within which ionization is dense enough to be approximated by a plasma with associated frequency ω. Within this core the Bohr adiabatic cutoff criterion is satisfied (Bohr, 1913a), and the radius of the core r_c can be described as

$$r_c = \frac{V}{\omega} \tag{70}$$

where V is the particle velocity (Magee and Chatterjee, 1977). Energy is absorbed in the core directly, because near the particle the surrounding matter does not have time to adiabatically follow the impulse of the particle. Core radii are thought to be in the nanometer range (Brandt and Ritchie, 1974; Magee and Chatterjee, 1977). Beyond the core radius r_c, but still no further than the maximum radial distance of a secondary electron or delta ray, we can define another region of energy deposition called the "penumbra" or "ultra track." The penumbra radius r_p has been determined empirically as

$$r_p = 39.6\ V^{2.7} \tag{71}$$

where the particle velocity is in 10^9 cm/sec and r_p is in nanometers (Magee and Chatterjee, 1977). For near relativistic particle velocities the penumbra radius may be a few micrometers. Roughly half of the local energy deposit is distributed in the core of radius r_c and the other half is distributed outside the core primarily in the penumbra. This is consistent with the rule of equipartition (Chatterjee, et al, 1973; Magee and Chatterjee, 1977). Though the energy density within the core may be fairly uniform, such is not the case in the penumbra (Magee and Chatterjee, 1977, 1980). Since the energy density in the penumbra is due mostly to delta rays which move somewhat radially away from the particle trajectory (Katz and Kobetich, 1968), we expect the energy density in the penumbra to decrease roughly as r^{-2} away from center and beyond r_c. Expressions for the energy densities in the core ρ_c and penumbra ρ_p of the heavy ion track correspond to (Magee and Chatterjee, 1977)

$$\rho_c = \frac{(dE/dx)}{2\pi r_c^2} + \frac{(dE/dx)}{2\pi r_c^2 + 4\pi r_c^2 \ln(r_p/r_c)}, \quad 0 \leq r \leq r_c \tag{72}$$

$$\rho_p = \frac{(dE/dx)}{2\pi r^2 + 4\pi r^2 \ln(r_p/r_c)}, \qquad r_c < r \leq r_p \tag{73}$$

where energy density is expressed in any convenient units such as $\mathrm{keV}/\mu\mathrm{m}^3$. This distribution of energy is essentially the initial energy configuration of the track and corresponds to a time of approximately 10^{-16} seconds. For neon particles of different velocities the energy structure has been calculated according to equations (72) and (73) and is shown graphically in Fig. 2.

For each particle energy plotted in Fig. 2 we observe a dose discontinuity somewhere between a 10^{-3} and 10^{-2} micrometer radius away from the particle trajectory. There is some controversy concerning the existence of a sharp boundary between the core and penumbra, and it has been suggested that the core and penumbra might have no sharp separating boundary at all when energy density is the only criterion for establishing a boundary (Paretzke, 1979). Another

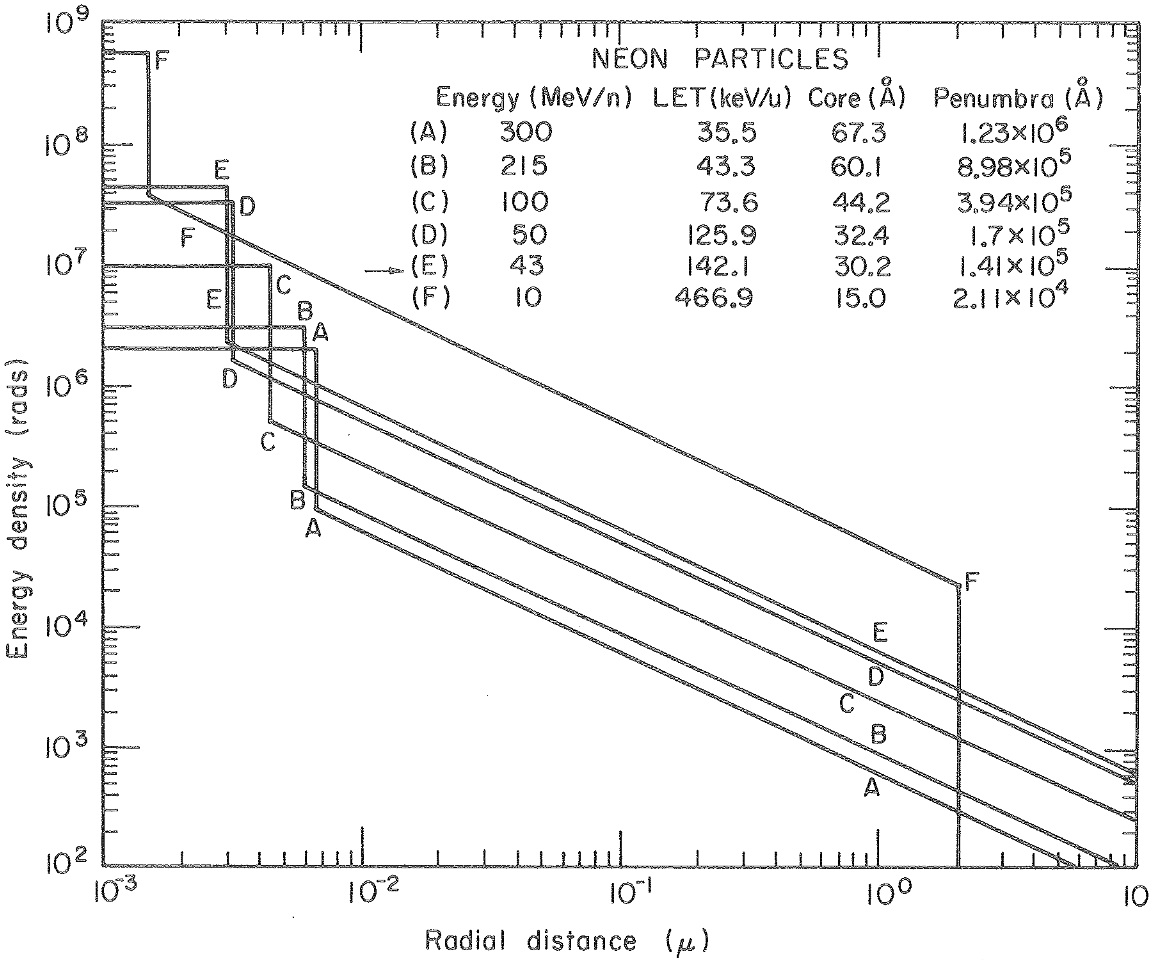

XBL772-3082

Figure 2. Diagram to show core regions and penumbra regions for tracks of neon particles at various energies. The core energy densities are to the left of the vertical discontinuity, and the penumbra energy densities are to the right. Each discontinuity is about 20 rads. Diagram reproduced from Magee and Chatterjee, 1977.

approach to the dose distribution problem is known as the delta ray model (Katz and Kobetich, 1968) and is illustrated in Fig. 3 for 1 MeV protons according to Paretzke's calculations. The delta ray model will be discussed in Section III.B.2. There are no dose discontinuities in this model though a core and penumbra might still be separable from a mechanistic viewpoint.

It is of interest to note that when Fig. 2 and Fig. 3 are superimposed, they are similar in the radial distance region less than 10^{-2} μm. The Paretzke plot follows the Magee and Chatterjee plot in that region but falls off early in the radial distance region greater than 10^{-2} μm. If we combined the data in Fig. 2 and Fig. 3 we would arrive at a plot which is a continuous line with two main regions of different slope, the steeper slope in the radial distance region less than 10^{-2} μm. Such a presentation of the data would suggest a core region with a relatively higher energy density gradient and a radius less than 10^{-2} μm beyond which is the penumbra with a lower energy density gradient. The break in slope would define the boundary between core and penumbra.

Data for these models is seriously lacking, so the models should be regarded only as guides for our thinking (Hasegan, et al, 1978; Paretzke, 1979). Though the existence of a sharp energy density boundary between core and penumbra is in dispute, there is general agreement concerning the radius of the penumbra (Brandt and Ritchie, 1974; Magee and Chatterjee, 1977; Paretzke, 1979). The penumbra radius is a measure of how far delta rays will travel away from the

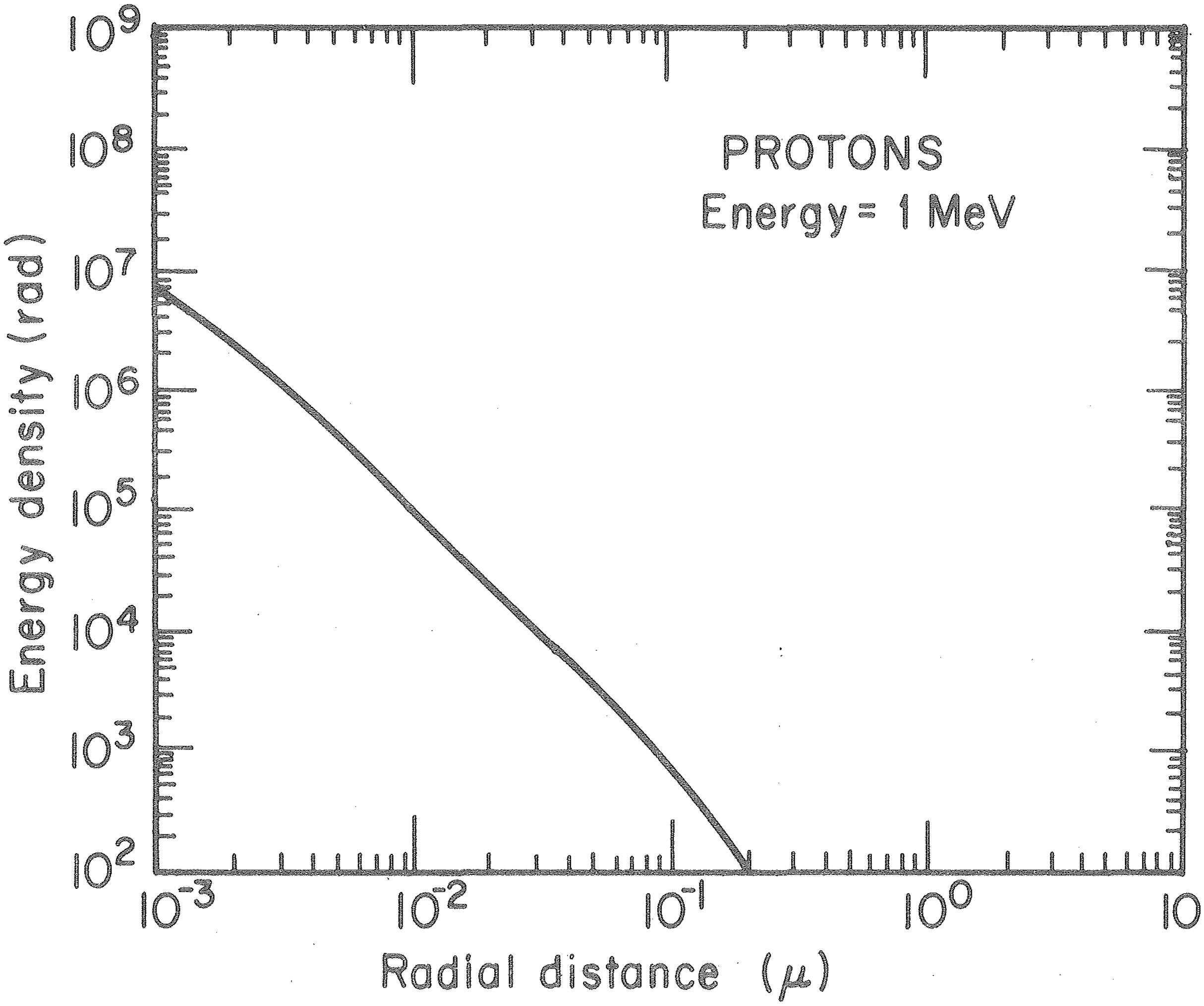

XBL807-3445

Figure 3. Diagram to show particle track energy density profile for 1 MeV protons. This diagram can be compared directly to Fig. 2. Redrawn from Paretzke, 1979.

particle trajectory. Since delta rays are charged particles (electrons), we expect their energy loss profile to follow the Bragg curve for electrons (Garcia, 1969). This implys a maximum penetration distance for the delta ray which is on the order of micrometers for energetic primary particles (Ritchie, et al, 1978). The track models predict penumbra radii to be on the order of micrometers. The experimental data reported here for heavy ion irradiated rat corneas show, in several cases, that plasma membrane lesions caused by the heavy ions also have radii on the order of micrometers.

Now if we inquire into the energy structure of a heavy ion track in biological tissue at some time, say a few seconds post irradiation, we must certainly discuss diffusion of ionization products through the aqueous milieu of cells (Tobias, et al, 1979b; Magee and Chatterjee, 1977). As a first approximation let us assume that the ionization products do not react but are free to diffuse with diffusion coefficient D. Then the concentration of ionization products c will be radially symmetric about the particle trajectory and will vary with time t as (Magee and Chatterjee, 1977)

$$c(r,t) = \frac{N_0 \exp[-r^2/(r_c{}^2 + 4Dt)]}{\pi(r_c{}^2 + 4Dt)} , \tag{74}$$

where N_0 is the number of ionization products formed per unit length of the particle track. Equation (74) is for an idealized 2-dimensional situation but is still useful as an approximation of energy structure through time. A more complicated 3-dimensional analysis has recently been presented (Magee and Chatterjee, 1980).

The ionization products which are subject to diffusion are due, in majority, to the radiolysis of water, (Mozumder and Magee, 1972; Magee and Chatterjee, 1979),

$$H_2O \rightsquigarrow \dot{H}, \dot{O}H, e_{aq} \quad .$$

These chemical species which are highly reactive are called free radicals and exhibit an unstable electron configuration with at least one unpaired electron. The free radicals will alter the energy structure of the track by reacting with surrounding molecules such as proteins, nucleic acids, and fatty acids in biological tissue (Henriksen, 1966). This situation is overwhelmingly complicated and does not as yet find description in a mathematical model. Only when we restrict our thinking to the transient intermediates due to water radiolysis, assume the target system is homogeneous and diffusable, and ignore the subsequent reactions which involve the free radicals can we approach the problem with solutions like equation (74). But equation (74) does permit an approximation to energy structure in the particle track up to times corresponding to milliseconds. One can convert the calculated initial energy transfer (-dE/dx) from the energy loss equations and from this number determine the initial number of ionization products N_0 based on some average amount of energy per ionization. In this case, 33 eV per ionization is frequently used (Setlow and Pollard, 1962). Having determined N_0 then equation (74) can be employed to advantage.

As mentioned earlier the actual energy deposition in the particle track is not continuous but occurs in spurs and blobs. The treatment for this more complicated affair has been developed and gives ionization product concentrations as functions of r, t, and z along the track (Magee and Chatterjee, 1980). The general form of the equations is similar to equation (74) however, and they also include the kinetics for reactions of the free radicals.

Before embarking on a search for single particle tracks in biological material, we should first examine evidence for single particle tracks in other systems. Some of the more established track detection methods will be discussed in the following section.

B. Empirical Work

1. Cloud and Bubble Chambers

The cloud chamber developed by C.T.R. Wilson (Wilson, 1897, 1899) was the first instrument used to detect and visualize the tracks of fast particles. For charged particles like alpha and beta rays a physical description of energy deposition had not been formulated; the physical treatment for charged particles had to await the insight of Bohr (Bohr, 1913a). But the theory of droplet formation and the mechanics of cloud chamber operation were well understood so that particle tracks could be studied with a degree of quantitation. The earliest cloud chambers employed a medium of air saturated by water or alcohol. A supersaturated vapor was created in an enclosing transparent jar by temperature and pressure manipulations. As a fast particle moved through the supersaturated vapor the ionized molecules along its trajectory became nucleation sites for condensation, and if temperature and pressure were properly adjusted, condensed droplets would become visible to reveal the particle track.

In a vaporous medium of dielectric constant ε_1, a charged condensed droplet with dielectric constant ε_2, radius r, and surface tension W will have a surface energy of

$$E_s = \left[4\pi r^2 W + \frac{\alpha^2}{2r}\left(\frac{1}{\varepsilon_1} - \frac{1}{\varepsilon_2}\right)\right] \qquad (75)$$

where α is the charge on the droplet (Wilson, 1951). A change in radius δr leads to a change in the surface energy which may be equated to the work required to bring the amount of vapor produced by evaporation at the vapor pressure p, in equilibrium with the droplet, to the saturation pressure p_o. This condition can be expressed as

$$\frac{d}{dr}\left[4\pi r^2 W + \frac{\alpha^2}{2r}\left(\frac{1}{\varepsilon_1} - \frac{1}{\varepsilon_2}\right)\right]\delta r = 4\pi r^2 \rho \delta r \, \frac{RT}{M} \ln p/p_o \qquad (76)$$

where ρ is the density of the droplet, R is the gas constant, T is absolute temperature, and M is the molecular weight of the vapor. After differentiation and rearranging terms in equation (76) we obtain

$$\frac{\rho RT}{M} \ln p/p_o = \frac{2W}{r} + \frac{dW}{dr} - \frac{\alpha^2}{8\pi r^4}\left(\frac{1}{\varepsilon_1} - \frac{1}{\varepsilon_2}\right) \quad . \qquad (77)$$

If we assume the surface tension is not a function of droplet radius then equation (77) is simplified since $dW/dr = 0$. Equation (77) is taken as the working equation for cloud chamber experiments and expresses the equilibrium condition for maintaining a droplet within the chamber (Wilson, 1951).

The major limitation of the Wilson cloud chamber is that the vapor density is low compared to condensed materials, so the detection efficiency is low for sparsely ionizing high energy particles. Glaser solved this difficulty by constructing a chamber filled with superheated condensed fluid rather than supersaturated vapor (Glaser and Rahm, 1955). Glaser's system, called the bubble chamber, permitted the detection of particle tracks which occurred rarely in the lower density cloud chamber (Glaser, et al, 1956). Following the introduction of the bubble chamber, several workers constructed bubble chambers which were more versatile and could detect low energy particles as well as high energy particles (Pless and Plano, 1956; Nagle, et al, 1956). The basic principle behind all bubble chambers is that, in the superheated and pressurized transparent chamber fluid, an ionizing particle will generate bubbles along its trajectory. The particle track is visualized as a series of micro-bubbles which can be enlarged by a momentary chamber expansion.

The theoretical description of bubble formation in a bubble chamber, also called cavitation, is far more complicated than the description of droplet formation in a cloud chamber. Several thermodynamical approaches have been attempted with some interesting results (Plesset and Zwick, 1952, 1954), and a fluid mechanical analysis provides still another important perspective (Seitz, 1958). Both the thermodynamical and fluid mechanical approaches suggest the existence of a critical bubble radius below which the bubble will collapse and disappear and above which the bubble will continue to expand. The critical radius is on the order of a few nanometers for several fluids (Seitz, 1958).

The main advantage of cloud and bubble chambers currently is that they permit one to observe particle tracks immediately as they occur. An analysis of the track is accomplished by photographing the track and making measurements on the photograph. However, most quantitative work is now carried out with different detection systems, some of which will be discussed shortly. Cloud and bubble chambers are of great historical importance, because they permitted the first visualization of particle tracks from nuclear decay and cosmic radiation (Pomerantz, 1971).

2. Emulsions

Perhaps the most widely used particle track detection methods are those which employ photographic emulsions. Various mixtures of gelatin and silver halide have been tested for detection efficiency, the most generally accepted emulsion being Ilford G5 nuclear emulsion sheets (Jensen and Matheisen, 1976). AgBr is the silver halide of choice for track detection emulsions. The Ilford G5 emulsion sheets are 0.6 mm thick, and fifty to one hundred sheets are mounted as a stack to attain a detector thickness of a few centimeters. As the charged particle traverses the emulsion detector, ionization occurs along the trajectory due primarily to delta rays (Katz and Kobetich, 1969). During development of the emulsion, silver ions near the regions of ionization are reduced to silver metal. The silver metal forms in grains along the particle tracks which are often measured photometrically (Behrnetz, 1976; Hasegan, et al, 1978).

The theory for particle track formation in emulsions was formulated by Katz and is known as the delta ray model or the Katz theory (Katz and Butts, 1965; Kobetich and Katz, 1968a, 1968b, 1969; Katz and Kobetich, 1969) with a concise formulation in (Katz, et al, 1972). The delta ray model has been expanded to cover low Z elements such as carbon particles (Behrnetz, 1976). But apparently the delta ray model does not explain track structure for ionizing particles of low velocity (Hasegan, et al, 1978). In any case, the delta ray model is useful in a multitude of track detection experiments and describes quite satisfactorily the majority of track data in emulsions.

The delta ray theory is a probabilistic approach to explain ionization along a particle track in a detector. The basic assumption of the theory is that a volume grain density in the developed emulsion at some radial distance r from the particle trajectory is given by

$$\langle n(r)\rangle = n_0[1 - \exp(-\bar{E}(r)/E_0)] \qquad (78)$$

where $\langle n(r)\rangle$ is the expectation of volume grain density as a function of r in the developed emulsion, n_0 is the volume grain density in the undeveloped emulsion, $\bar{E}(r)$ is the mean energy deposited by secondary electrons in a volume element V_0 as a function of r, and

E_o is the characteristic energy deposit which makes $n = 0.63\, n_o$. The numerical value of E_o depends on the particular emulsion and development conditions for an experiment. If we assume the emulsion is microscopically homogeneous, then the mean energy deposit will be

$$\bar{E}(r) = \frac{1}{V_o} \int_0^{r_o} E(r) 4\pi r^2 dr \tag{79}$$

where $V_o = \frac{4}{3}\pi r_o^3$ is the volume of an average emulsion grain with $r_o = 0.17\ \mu$m for Ilford G5 emulsion. The point dose distribution $E(r)$ is expressed as

$$E(r) = \frac{-Ne}{2\pi r} \int_I^{W_{max}} f(r,Q) \frac{d\sigma}{dW}\, dW \tag{80}$$

where Ne is the volume density of electrons in the emulsion, I is the mean excitation potential of the emulsion, $W_{max} = 2mc^2\beta^2/(1-\beta)^2$ is the maximum energy transferred to an electron of mass m, $f(r,Q)$ is the energy dissipated per unit length at a radial distance r due to an electron with initial kinetic energy $Q = W - I$, and $\frac{d\sigma}{dW}$ is the cross section for electron production (Jensen, et al, 1976).

Track detection by emulsions has advanced our understanding of heavy ion tracks and has been especially helpful in visualizing particle tracks and exploring energy structure along the particle trajectory.

3. Etched Plastics

Heavy ion tracks may be formed in bulk samples of virtually any insulating material but not in metals and other good conductors (Fleischer, et al, 1975). A great many track detectors in this category have been employed and include Lexan polycarbonate, cellulose nitrate, silver chloride crystals, cellulose triacetate, mica, phosphate glass, and many others (Fleischer, et al, 1975). Several different techniques can be useful in visualizing tracks in insulators once they have been etched or otherwise tagged, and these techniques include light microscopy, scanning and transmission electron microscopy, and electron diffraction. The most comprehensive list of protocols for the chemical etching and tagging of particle tracks is given in (Fleischer, et al, 1975).

The earliest observation of particle tracks in an insulator is attributed to Silk (Silk and Barnes, 1959) who analyzed mica samples with a transmission electron microscope in the electron diffraction mode of operation. Silk did not chemically prepare his mica samples but instead directly observed the crystal lattice dislocations along the particle tracks caused by fissioning elements. Following Silk's observations several workers began testing new insulating track detectors and developed improved methods of revealing and visualizing particle tracks (Fleischer, et al, 1975). The advantage of insulating track detectors over cloud chambers, bubble chambers, and emulsions is that they have superior detection efficiency, a wider range of energy sensitivity, and greater resolution for spacial detail.

The mechanisms by which tracks ultimately appear in insulating detectors are complex and depend on the particular detector and processing conditions. At a most basic level, the particle track consists of charged species resulting from ionizations which remain fixed locally for some time, because the detector substance is solid and does not rapidly anneal. The distribution of ionization and size of the track have been modeled with some success by applying the delta ray model to data obtained with Lexan polycarbonate, cellulose nitrate, and mica (Katz and Kobetich, 1968). The delta ray model predicts a threshold energy density below which a track will not be etched, and calculations based on cylindrical geometry indicate that the energy density drops below the threshold level at a critical radius of approximately 2 nanometers in the aforementioned detector materials.

Polycarbonate plastic was selected for use in the experiments reported here to measure the fluence (number of heavy ions per unit area) of the heavy ion beams which irradiated the cornea samples. The decision to employ polycarbonate plastic as a track detector is based mainly on the relative ease with which the plastic can be handled and etched. More details on the use of plastics will be given in Section V.C.

IV. CHOICE OF BIOLOGICAL TISSUE FOR THE ANALYSIS

One critical decision at the inception of this research concerned the choice of an appropriate biological tissue which would lend itself to experimentation with a minimum risk of artifact induction but which would be a sensitive indicator of the sought after effects. Initially, it seemed that neural tissue might be a sensitive indicator of radiation damage particularly since it had been established earlier (Mamoon, 1969) that inhibition of myelination of nerves resulted from doses as low as 200 rads of x-rays or heavy ions. Moreover, a reliable protocol for primary cultures of newborn rat cerebellar explants had been developed (Mamoon, 1969), and this protocol provided uniform tissue cultures on glass cover slips which could be handled easily during irradiation and subsequent preparation for scanning electron microscopy. Figure 4 is a micrograph taken with the scanning electron microscope (SEM) of a region of neuroglial cells from a 2 week old culture of rat cerebellum. This region of tissue consists mostly of microprocesses of about 1/2 micrometer in diameter and occasional cell bodies of about 5 micrometers in diameter. If single heavy ion tracks, whose radii would not be expected to exceed a micrometer (see Section III.A.2.), were to be observed in a network of glial cells like those of Fig. 4, they would be difficult to locate. The glial tissue already contains too many open spaces which occur normally between microprocesses in nonirradiated specimens. A more tightly packed tissue would seem appropriate.

Several of the nerve cell bodies in cerebellar neural networks are large; Purkinje cell bodies may be 20 micrometers in diameter, so that

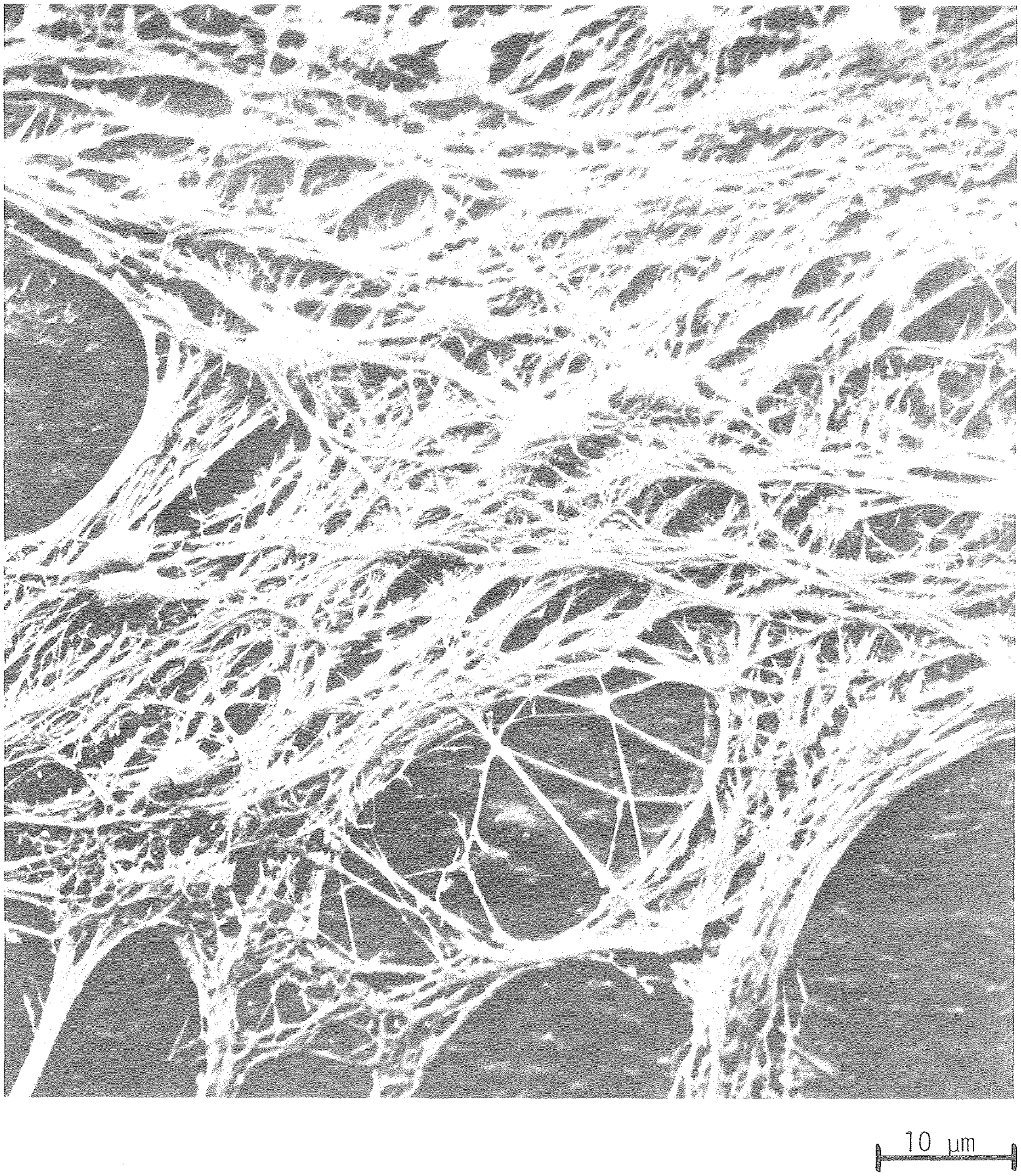

XBB 806-7683

Figure 4. SEM micrograph of glial cells from rat cerebellar tissue culture grown two weeks. This sample was not irradiated. The dark background is the plasma clot on which the tissue was grown.

they might manifest heavy ion lesions if their membrane surfaces were morphologically uncomplicated. This did not turn out to be the case. Figure 5 shows a Purkinje cell nested in granule cells and other nerve cells from the rat cerebellum (Diamond, 1980). We observe that the nerve cell membrane surfaces are morphologically quite complicated, and the membrane extensions are on the order of micrometers or less in diameter. Again, this level of membrane complexity would hinder a search for heavy ion lesions. For that reason alone it seemed prudent to abandone the cerebellar tissue culture as a test specimen for particle tracks.

The effects of heavy ion radiation on a highly specialized neural tissue, the retina, had been studied (Malachowski, 1978) with indication from transmission electron microscopy that particle tracks might possibly be recorded in the rod outer segments. However, membranous whorls found in irradiated rod outer segments occur frequently in normal retinas which have not been irradiated (Beatrice, 1980). But since the rod outer segments are tenuously connected to the cell body by a mere cilium, heavy ion irradiation could possibly disrupt this fragile connection and denude small regions of rod outer segments. Figure 6 is an SEM micrograph of a rat retina in cross section showing the various cell layers within the retina. The uppermost region is comprised mostly of rod outer segments. A higher magnification micrograph views the top of the rod outer segment layer with the pigment epithelium removed (Fig. 7). Each rod outer segment of rat retina measures about one micrometer in diameter. We observe that the

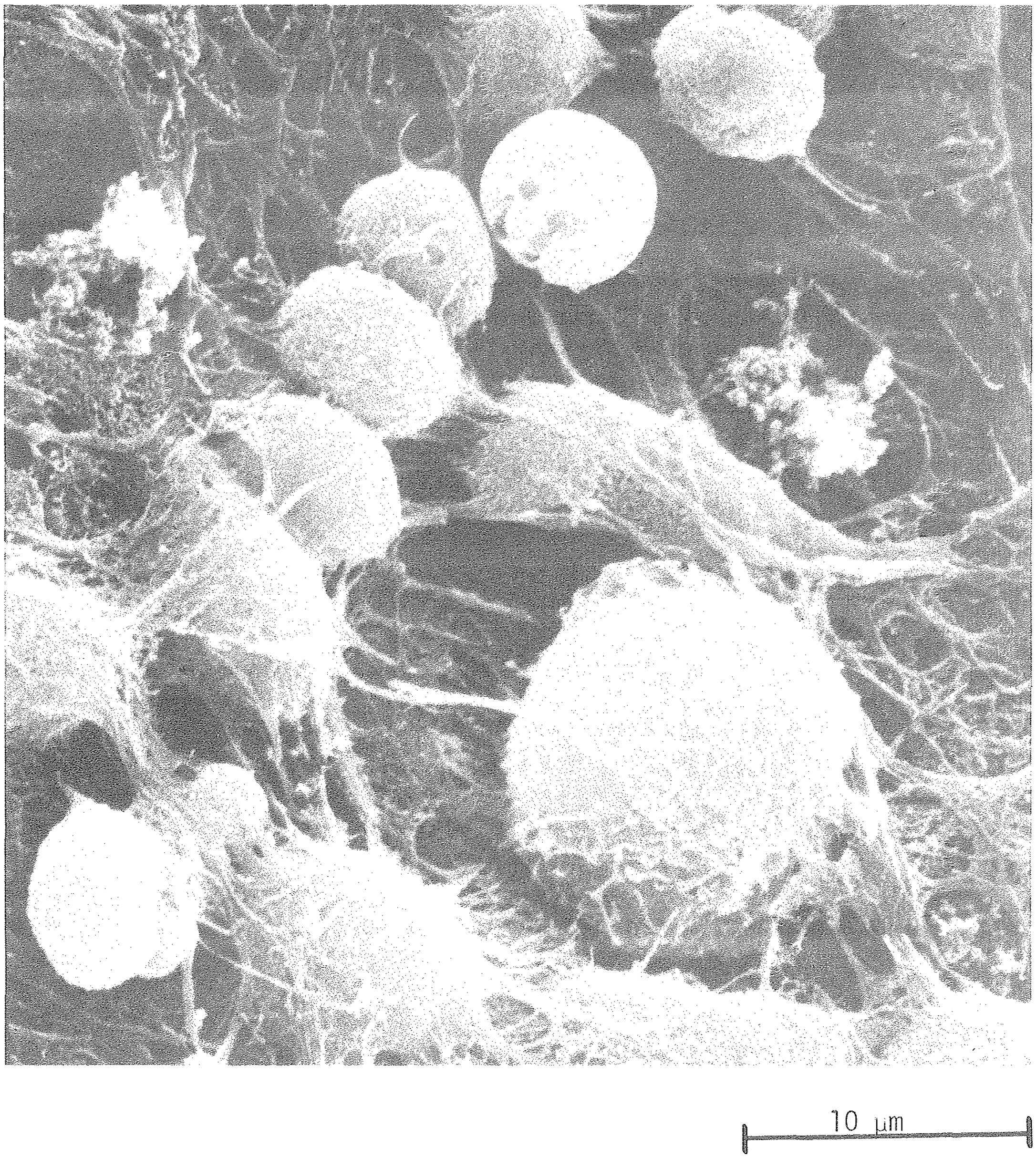

XBB 806-7681

Figure 5. SEM micrograph of Purkinje cell in a nest of granule cells from the rat cerebellum. Note the complicated morphology of the Purkinje cell plasma membrane.

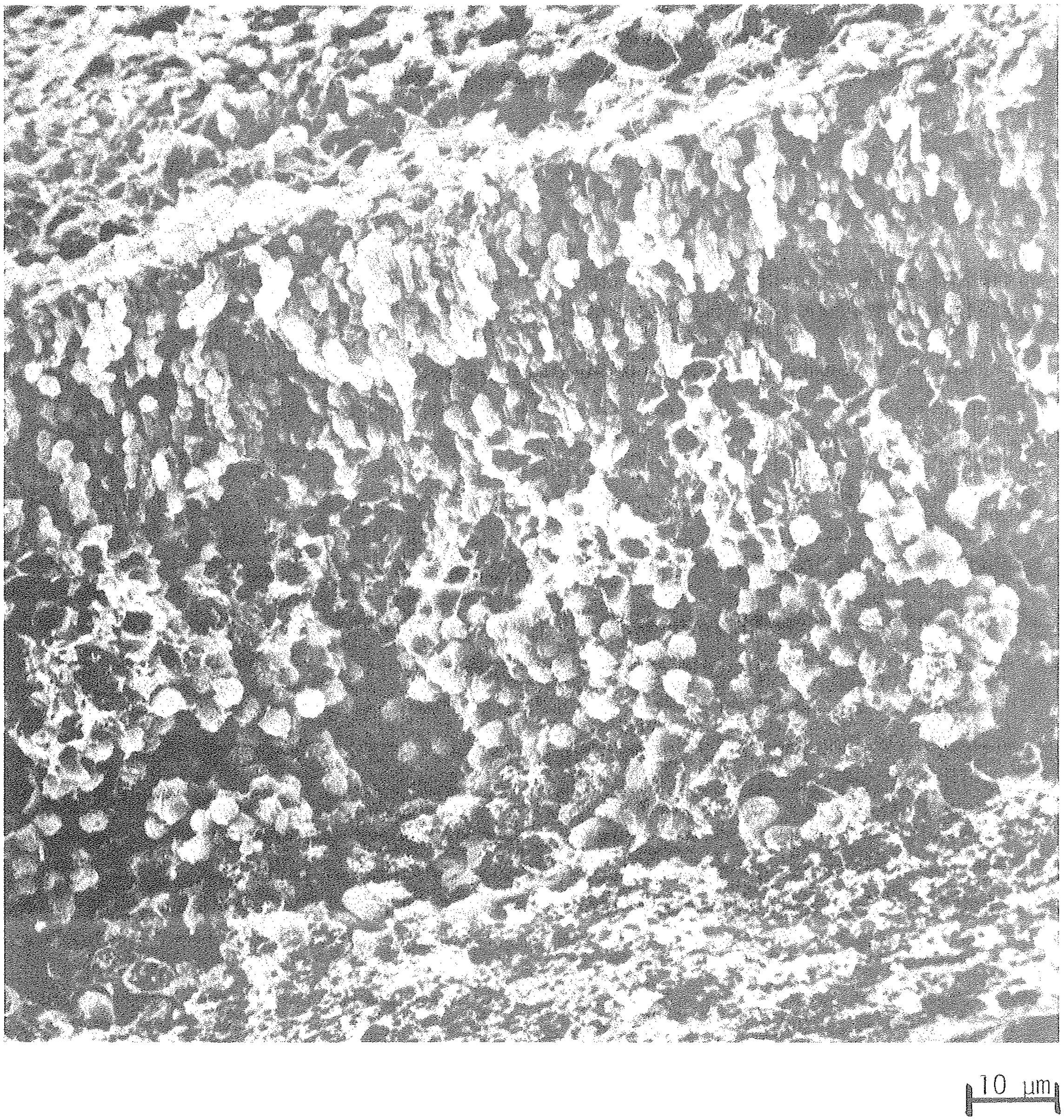

XBB 806-7682

Figure 6. SEM micrograph of rat retina in cross section. Toward the top of the micrograph is the rod and cone layer with remnants of pigment epithelium. The middle region is the nuclear layer, and the bottom region is the ganglion cell layer.

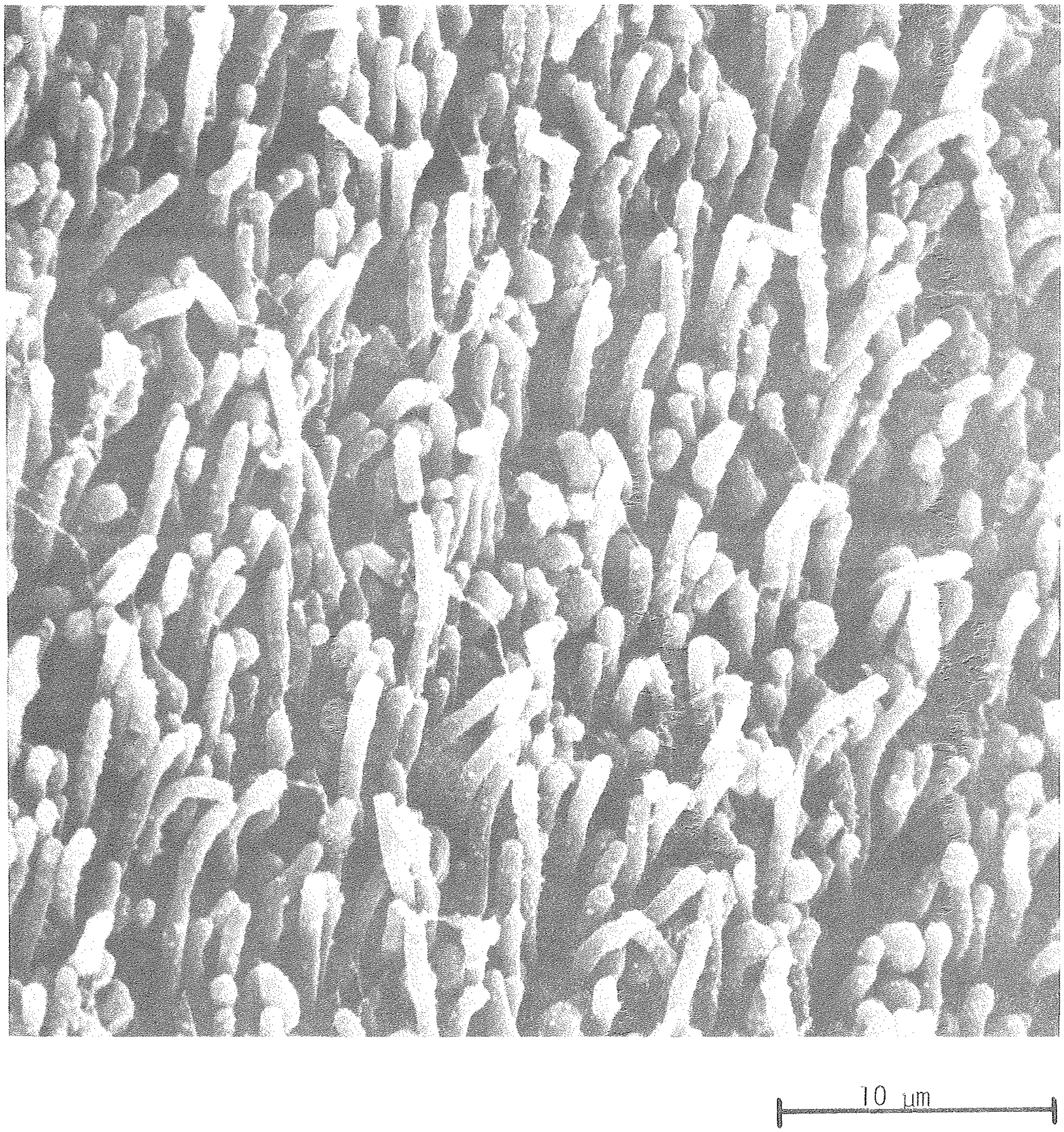

XBB 806-7680

Figure 7. SEM micrograph of rod outer segments from rat retina. Each outer segment measures near one micrometer in diameter.

outer segments are not tightly packed so that a fraction of the outer segment layer is cell free space. The retinas of other animals besides the rat might be more tightly packed, but for the purpose of detecting single particle lesions the rat retina appears inadequate.

The conclusions reached are that rat cerebellar cultures and retina tissue are not only morphologically complicated but contain intrinsic morphological details which might easily be misinterpreted as particle lesions. It is therefore essential to find a biological tissue that is more uniform and which does not contain structural details in the size range of the sought after particle lesions. A flat featureless tissue specimen would seem ideal for this examination, and one such tissue which is easily irradiated and excised from the rat is the cornea. The research reported here was conducted entirely on the rat cornea which proved to be a highly satisfactory tissue for the analysis.

A. Anatomy of the Eye

The anatomy of an eye is shown in Fig. 8 to help familiarize the reader with eye structures and in particular the location of the cornea. The main features of the eye which are relevant to this work are:

i. The living eye is readily removed from the anesthetized rat as a whole organ.

ii. The excised eye will maintain its normal shape during irradiation.

iii. The cornea is completely exterior to the eye and is thus accessible to study.

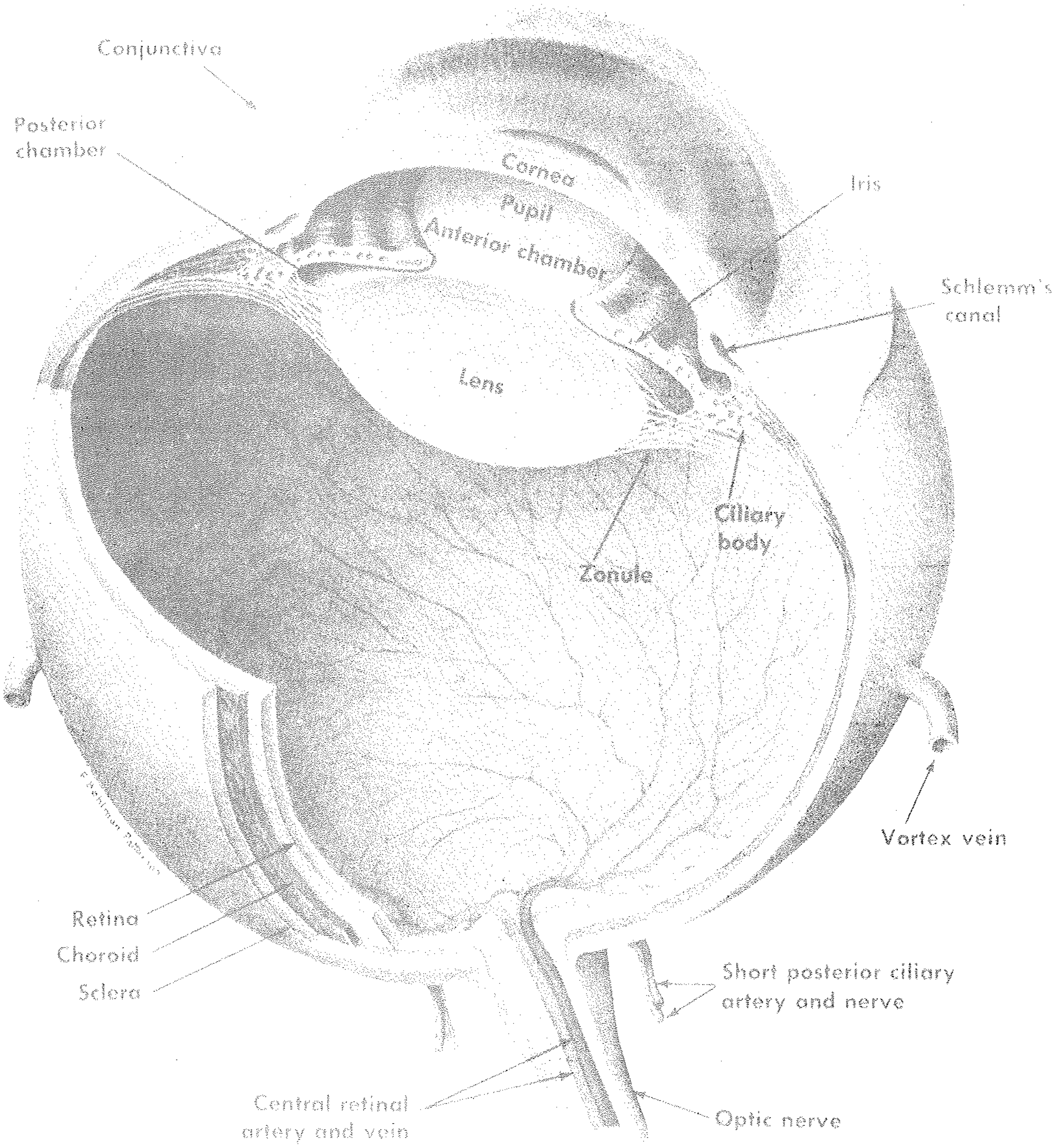

XBB 806-7667

Figure 8. The anatomy of a human eye. The major difference between the human eye and the rat eye used here is that the rat cornea occupies nearly half the globe surface area. Note that the cornea is anterior to the eye and can be exposed directly to irradiation.

iv. The anterior surface of the cornea has no blood supply but is normally fed by diffusion through anterior chamber fluid, a property which permits extended corneal life after excision when an appropriate bathing medium is employed.

The protocol for whole eye excision and handling during irradiation is given in Section V.

B. Anatomy of the Cornea

As illustrated in Fig. 8 the cornea is a transparent extension of the sclera. If we examine the cornea in cross section, as shown in Fig. 9, we can define several strata. The most exterior of the five major layers is really a continuation of the conjunctiva, and is composed of stratified squamous epithelium. Its thickness in the rat is around five to ten sheets of cells. The basal sheet of cells is of columnar form while the most exterior sheet is of flattened cells, those between the two sheets are polyhedral in varying degree.

Beneath the epithelium lies Bowman's Membrane, a structureless membrane dividing the epithelium from the substantia propria or stroma. It is firmly attached to the stroma and is thought to be a modification of that layer. Bowman's membrane is tough and inelastic.

The main body of the cornea is the substantia propria or stroma, and is composed of modified fibrous connective tissue in several lamellae. The lamellae contain many extracellular fibrils of collagen arranged in flat narrow bands to form an elastic meshwork. The stroma is responsible for overall maintenance of corneal shape and stability.

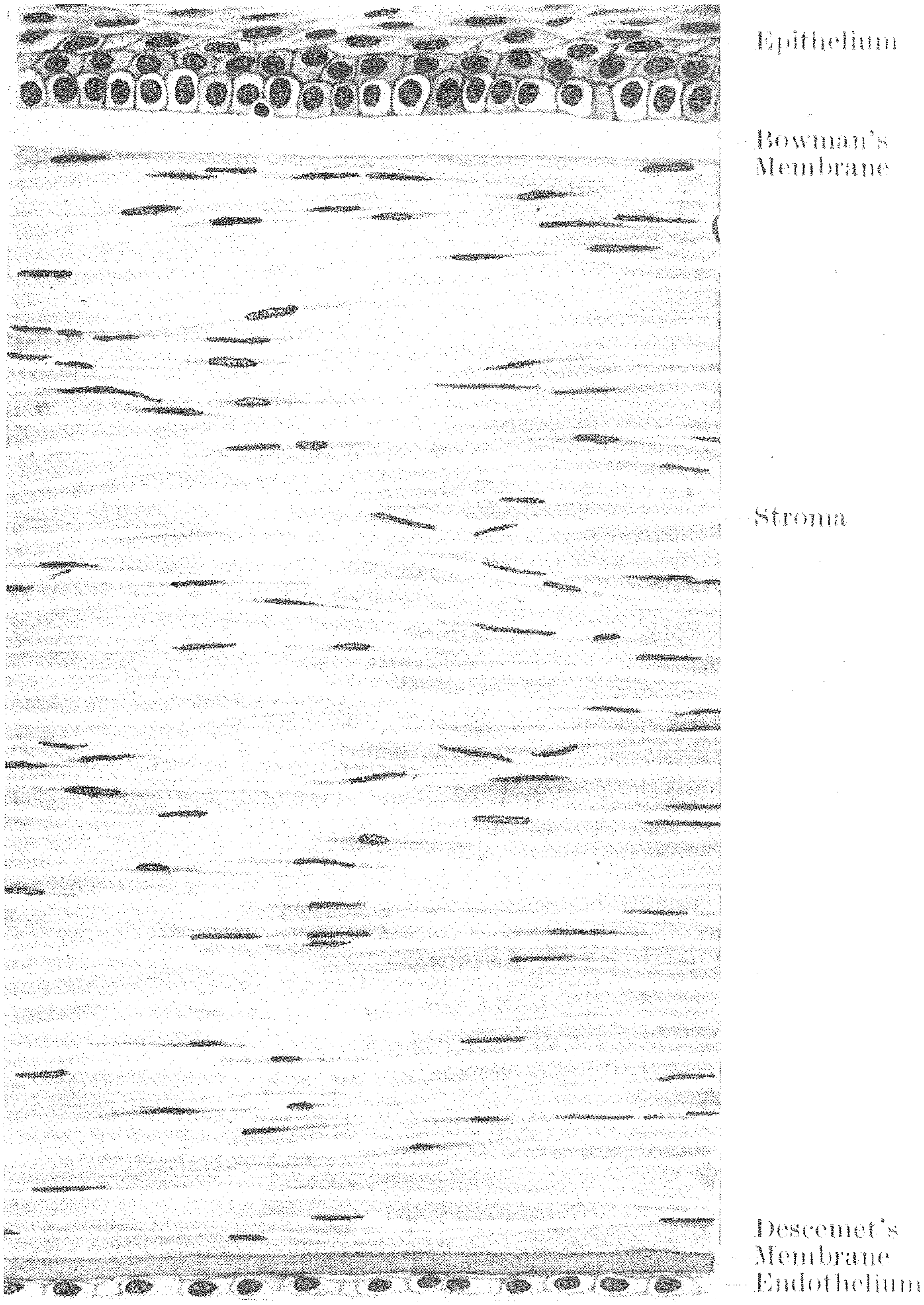

XBB 806-7668

Figure 9. The five major layers of the cornea. The epithelium is the anterior surface, the endothelium is the posterior surface, and Bowman's membrane, the stroma, and Descemet's membrane are layered in between.

Backing the stroma, but sharply defined, is another structureless somewhat elastic membrane known as Descemet's membrane. It is a smooth membrane with parallel surfaces and uniform thickness. This basement membrane probably derives from the endothelial layer beneath it.

The most interior layer of the cornea is the endothelium which is continuous with the anterior surface of the iris via Schlemm's canal as shown in Fig. 8. The endothelium comprises a single layer of rounded cells which bulge posteriorly into the anterior chamber of the eye. The anterior chamber is filled with fluid known as aqueous which bathes the endothelium.

C. Surface Morphology and Characterization of Corneal Epithelium

We turn now to the tissue of choice for this work, the rat cornea. In searching for heavy ion tracks in the cornea we must characterize the cornea morphology before and after irradiation. The instrument employed for this purpose throughout the analysis is the SEM in the secondary electron image mode of operation which will be detailed in part V.G.1. The significance of collecting data with the SEM in this way is that only surface morphology will be recorded. We can confine our tissue characterization then to a discussion of the exterior surface of the cornea, and in particular, only the outermost layer of squamous epithelial cells need be described.

The flat corneal epithelial cells of an adult rat consist of a continuous layer of cells which are 30 to 40 micrometers in diameter and a few micrometers thick. The anterior epithelial cells are so flat that the nuclei bulge at the surface and measure 8 to 10 micrometers in diameter (Blumcke and Morgenroth, 1967; Pfister, 1973). These cells resemble an over easy fried egg in appearance.

Except where cell desquamation is occurring, the anterior corneal surface is quite flat and morphologically simple. Figure 10 is an SEM micrograph of a control (non-irradiated) cornea. Boundaries between the plasma membranes of individual cells are readily discernible, and the cell nuclear outline is also visible. The corneal surface has no void space; each cell abuts with other cells everywhere along its perimeter. A higher magnification SEM micrograph of the same cornea shows a single epithelial cell, Fig. 11. The small bumps on the plasma membrane surface are microvilli. The bright flecks across the surface are artifacts due to media crystallization during chemical fixation (the subject of artifacts will be addressed in Section V.F.5.). An even higher magnification in Fig. 12 shows a region of contact between three cells. The cell contacts are smooth with no void space, so for the purpose of these experiments the entire anterior surface of the cornea can be regarded as a continuous sheet of plasma membrane. The worm-like structures on the plasma membranes are the microvilli, all of which have a characteristic width of about 0.2 micrometers (Pfister, 1973). This characterisitic width can be helpful as a reference dimension for high magnification micrographs.

We note that the anterior cornea has no prominent structures in the one to two micrometer size range. Nor does the anterior cornea have void spaces. Thus, the rat cornea comes close to satisfying the

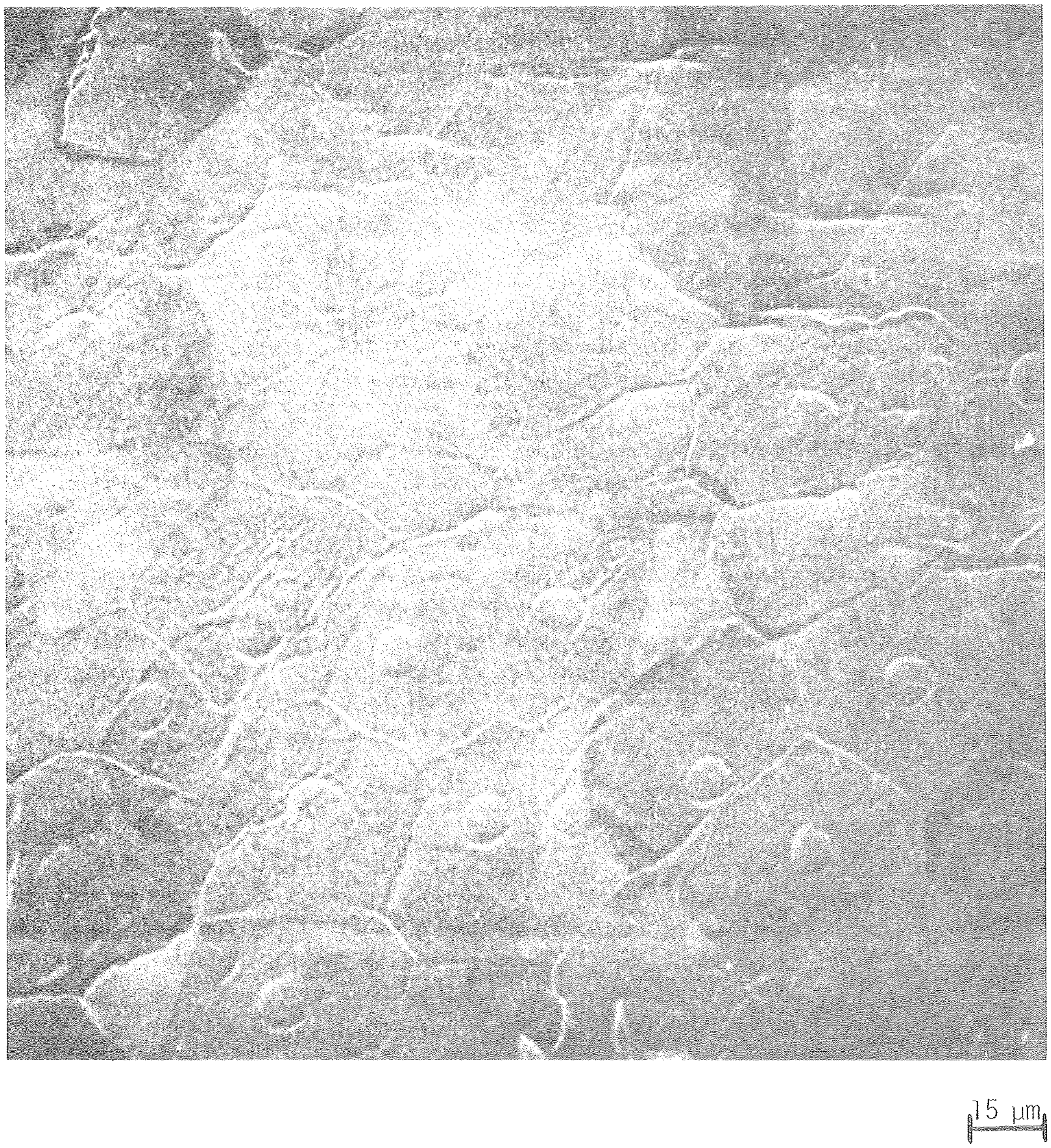

XBB 806-7677

Figure 10. SEM micrograph of adult rat corneal epithelium. Cell nuclei bulge at the surface with diameters of 8 to 10 μm. The cell diameters range from 30 to 40 μm. This is a control sample which was not irradiated.

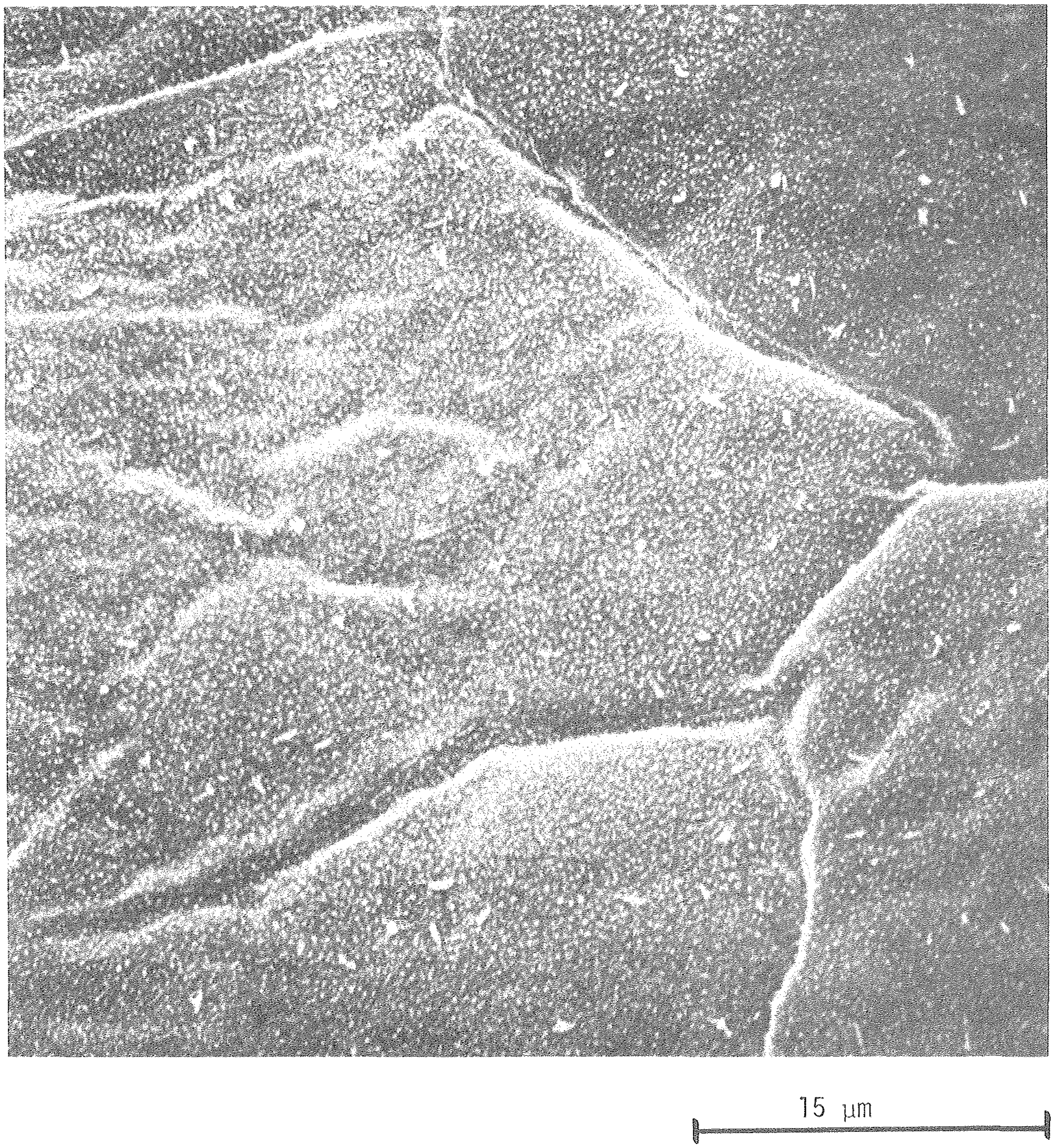

Figure 11. SEM micrograph of individual corneal epithelial cell. Borders between adjacent cells and the nuclear bulge are evident. Bright flecks are crystalline media. This sample was not irradiated.

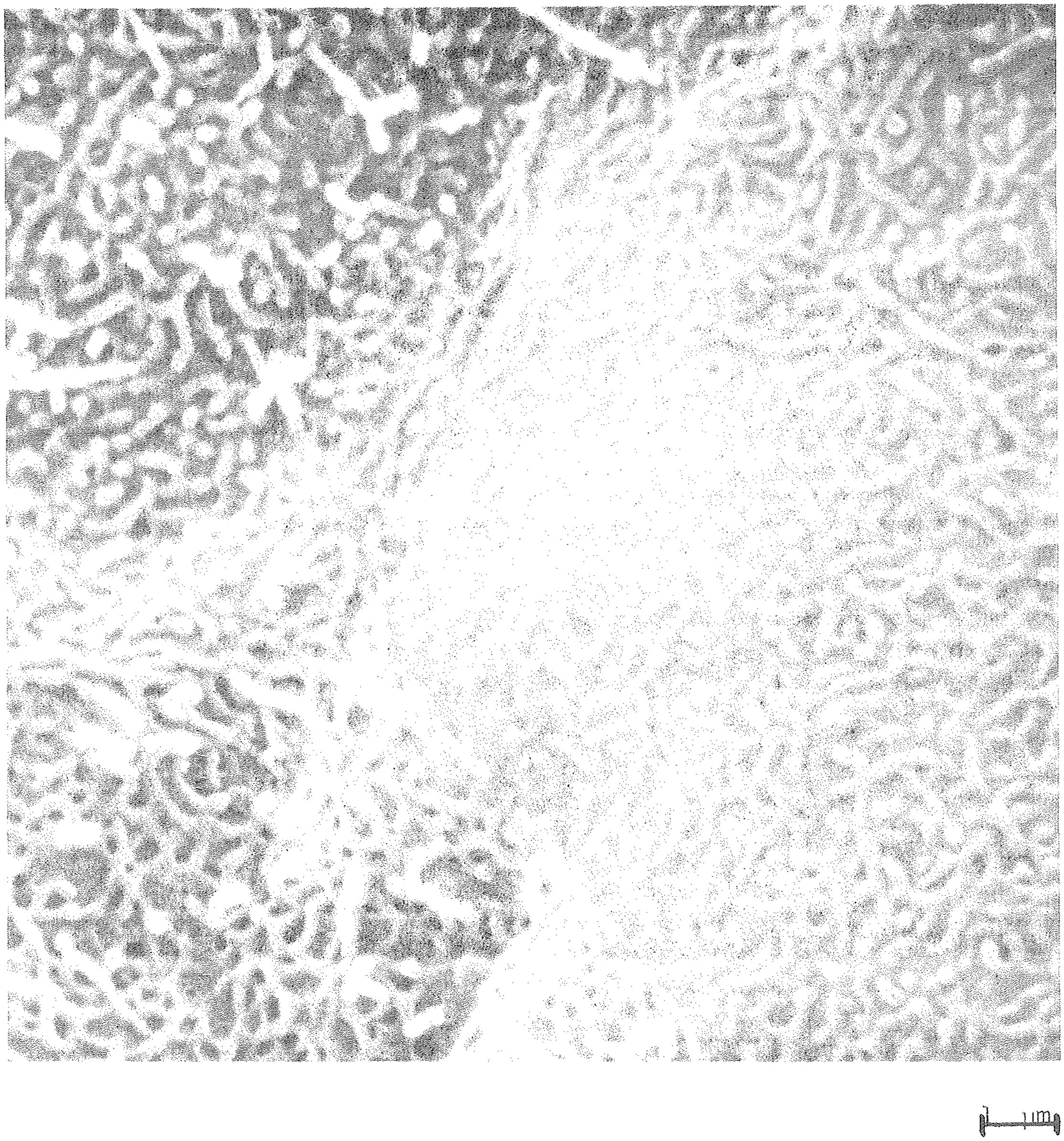

XBB 806-7679

Figure 12. SEM micrograph of plasma membranes of corneal epithelium. Three cells abut each other. The worm like structures are cell surface microvilli which have characteristic widths of 0.2 µm. This sample was not irradiated.

criteria for an ideal biological surface to serve as a detector of heavy ion tracks.

A few final remarks concerning desquamation on the anterior cornea are important. The corneal epithelium is a rapidly regenerating tissue requiring about seven to ten days for a young cell at the basal surface of the epithelium to move toward the anterior surface and undergo desquamation as an old cell (Freeman and Lai, 1978). During the aging process of an epithelial cell the surface concentration and length of plasma membrane microvilli fluctuate continually (Pfister, 1973). In general, epithelial cells undergoing desquamation have fewer and shorter microvilli than the younger cells beneath them. In viewing the micrographs presented in this work we will observe these fluctuations of plasma membrane microvilli.

Having discovered a suitable biological tissue for study we are prepared to begin experimentation.

V. EXPERIMENTAL METHODS AND TECHNICAL DETAILS

A. Overview and Approach

The goals of this work are to provide convincing evidence that an individual heavy ion can produce a lesion in biological tissue, and that the size of the lesion bears some direct relationship to the local energy deposited from the ionizing particle. The rat cornea, having been selected as a suitable tissue for study, was irradiated in the heavy ion beam, chemically fixed shortly after irradiation, and examined with the SEM. A series of x-ray exposed corneas was also examined for comparison with the heavy ion irradiated corneas. Both types of irradiated corneas were compared to control corneas which were not irradiated but which were otherwise identically treated. A total of 84 corneal samples were irradiated with heavy ions, 50 samples received x-ray exposure, and 52 samples were non-irradiated controls.

B. Sample Preparation Before Irradiation

The rats used in these experiments were five to six month old Wag-Rij albino males and females weighing about 300 grams each. Usually an hour before irradiation the rats were anesthetized until dead with ether vapors in a sealed bell jar. This required that the rats be subjected to ether for five to ten minutes. Immediately after their diaphram spasms subsided the rats were removed from the ether and layed on a surgical pad. Both whole eyes were enucleated with surgical scissors and dropped carefully into a beaker containing maintenance medium at room temperature. The whole eyes were stored in medium at room temperature up to the time of irradiation. If delays in obtaining the heavy ion beams were expected, then the beaker of eyes was cooled on crushed ice to slow the metabolism of the living eye cells. Forceps were used to grasp the optic nerve trunk in manipulating the eyes, so that the cornea was never touched. Utmost care was taken to ensure that the corneas would not receive mechanical damage.

The medium was mixed in 200 ml quantities under sterile conditions according to the following recipe:

50 ml fetal calf serum
50 ml minimum essential medium (mem)
100 ml Earl's balanced salt solution (bss)
2 grams glucose.

After the solution was mixed and just prior to use, the medium was oxygenated by shaking in air. This medium has been shown to sustain healthy rat tissue for periods up to several weeks (Raybourn, 1979). Quite likely, cells on the interior of the eye will suffer from lack of blood circulation, but the anterior surface of the cornea, being in direct contact with the oxygenated maintenance medium is expected to remain healthy for several hours at least.

To support the whole eyes during irradiation, the globe of the eye was punctured through the sclera with a No. 28 hypodermic needle. The eye could then be held by the needle during irradiation. Each eye was nested gently in a small tuft of cotton soaked in medium to keep the eye moist during irradiation. The corneas, however, were left uncovered but remained moistened by the capillary action of medium from around the sclera. All irradiated eyes were oriented so that the anterior cornea faced the irradiating beam.

C. Procedure for Controls, Etched Plastics, and Blind Experiments

For every irradiation experiment a series of control samples was run simultaneously,with the controls being manipulated in a manner identical to the handling of irradiated samples. While some samples were being irradiated, the controls were being exposed to air in a radiation free room. The controls were also chemically fixed alongside the irradiated samples. A total of 52 control corneas were analyzed for this work.

When plateau (recall Section III.A.1.) heavy ions were used, a sheet of red polycarbonate plastic was mounted behind each eye to receive the same radiation delivered to the sample. In this way there were two checks on the beam fluence: the usual calculation of fluence from a known dose (Section VII.A.) and the measurement of particle tracks in plastic. After irradiation the plastics were etched for three to six hours in 6N NaOH at room temperature. When periodic examination of the etched plastics under the light microscope revealed the presence of particle tracks, the etching was stopped and the plastics were washed in clean water.

To determine the particle beam fluence, each plastic was examined under a calibrated light microscope and the number of tracks per unit area was counted and expressed as number per cm^2. For low fluence beams (around $10^4/cm^2$) an area for counting was chosen to give at least 25 counts while for high fluence beams (around $10^8/cm^2$) an area was chosen to give at least 100 counts. At least four different counts were made for each plastic and the numbers were averaged. The beam fluence determined in this manner was taken to be a more accurate measure of fluence than calculations based on dose. When corneas were irradiated at the Bragg peak (recall Section III.A.1.) plastics behind the eye were not employed because the heavy ions did not penetrate through the eye, and plastics in front of the eye were not employed because this might stop the particles before they strike the eye. For the Bragg peak exposures, fluence was determined by the calculation method (Section VII.A.).

For example, Fig. 13 shows two light micrographs of plastic irradiated with 500 MeV/amu iron particles. The actual sample area of each micrograph is 0.22 cm^2. The top micrograph has a count of 24 giving a fluence of $24/0.22\ cm^2 = 109/cm^2$, a very low fluence. The bottom micrograph has a count of 32 giving a fluence of $32/0.22\ cm^2 = 145/cm^2$. The top and bottom micrographs were from different iron beam irradiations.

When higher fluence beams are recorded in plastics, etch times must be decreased. Etching plastics must be monitored carefully to ensure that etched tracks do not overlap. Defects in the plastic will produce etch pits which can be mistaken for particle tracks especially with high fluence beams (Fleischer, 1975), unless the plastic is placed at an oblique angle to the beam. Then the tracks have the distinct appearance of comets and can easily be counted. Figure 14 illustrates these points for two different exposures to a 530 MeV/amu silicon beam. The actual sample area in each micrograph of Fig. 14 is 0.09 cm^2. The

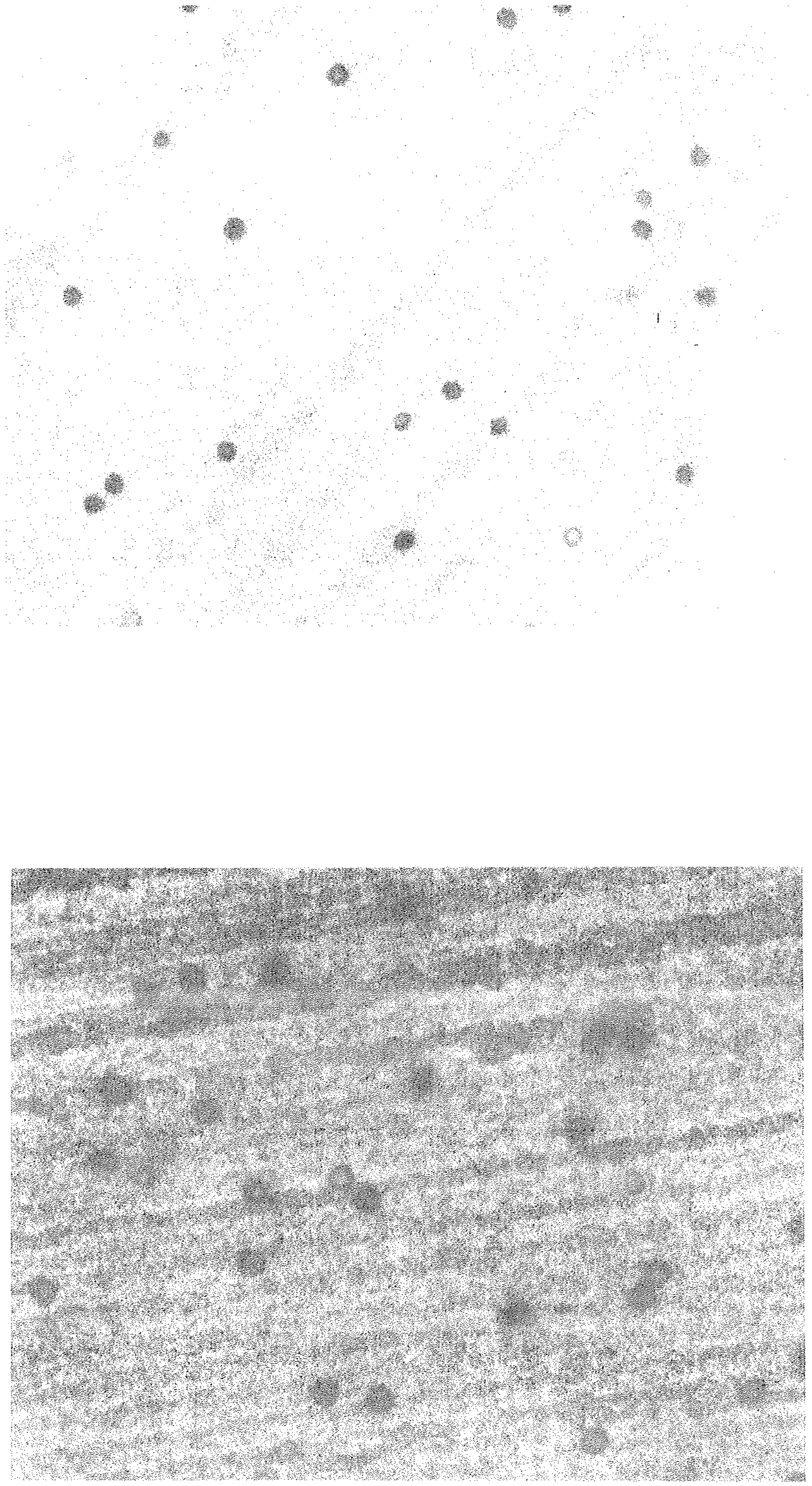

XBB 806-7672

Figure 13. Light micrographs of etched tracks in iron irradiated plastic. The actual sample area in each micrograph is 0.22 cm^2. The top micrograph has a fluence of 109/cm^2; the bottom has 145/cm^2. Top and bottom micrographs are from different experiments.

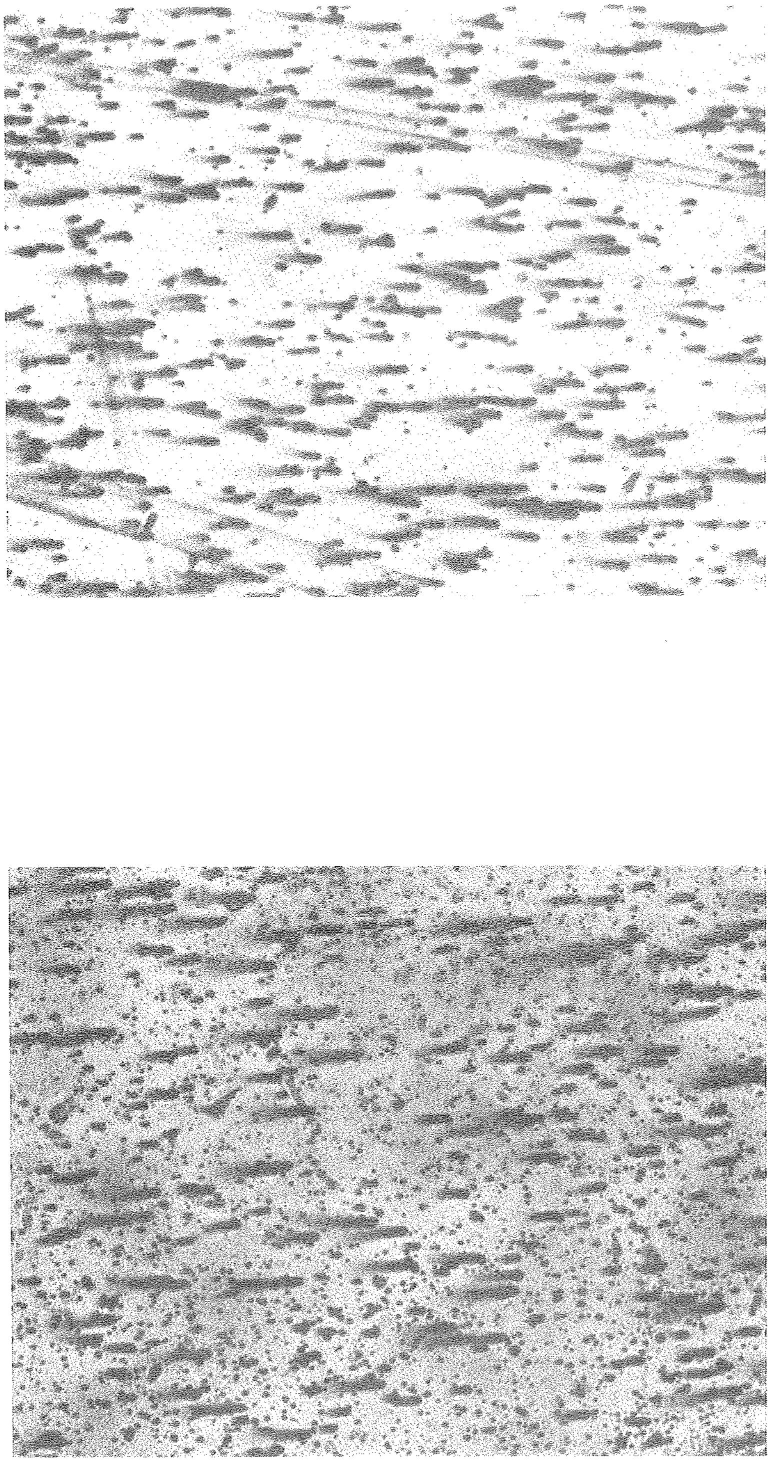

XBB806 7671

Figure 14. Light micrographs of etched tracks in silicon irradiated plastic. The actual sample area in each micrograph is 0.09 cm^2. The top micrograph has a fluence of 4.7 x 10^3/cm^2; the bottom has 3.1 x 10^3/cm^2. Top and bottom micrographs are from different experiments.

top micrograph has a count of 425 giving a fluence of 425/0.09 cm^2 = 4.7 x $10^3/cm^2$. The bottom micrograph has a count of 280 giving a fluence of 280/0.09cm^2 = 3.1 x $10^3/cm^2$. Note that the comet like particle tracks can be distinguished from the circular etch pits due to surface defects in the plastic.

Whenever possible in this work, etched plastics were employed to determine the fluence of the heavy ion beam which irradiated the rat corneas.

As a guard against my own interpretive preconception entering the examination of irradiated corneas, each corneal sample was coded by a laboratory partner. Irradiated corneal samples and non-irradiated controls were mixed together before the SEM analysis. Only after the SEM micrographs were recorded and commented upon were the samples decoded to determine which corneas were and were not irradiated. In this regard the SEM work was conducted as a blind examination.

D. Procedure for X-ray Exposed Corneas

Though microscopic membrane lesions were not expected to occur for cornea samples exposed to x-rays, it was important to run a series of experiments in which corneas received macroscopic doses of magnitude similar to the doses delivered to corneas by heavy ions. For equal macroscopic doses, if membrane lesions occur in heavy ion irradiated corneas but not in x-ray irradiated ones, then we can conclude that lesion formation is not a phenomenon related to macroscopic dose but rather is related to the microscopic distribution of energy density. This situation was born out by the data, as no lesions were observed in controls or x-ray irradiated corneas for macroscopic doses ranging from 10 to 100,000 rads.

For these experiments, a medical x-ray tube was operated at 150 kVp potential and 10 mA current. An aluminum filter of 0.040 inch (≈1 mm) thickness was used in addition to the inherent filtration for low dose rate exposures, and the filter was removed for high dose rate exposures. Dosimetry was done twice before each set of exposures and once following each set with a Victoreen dosimeter placed at the same location as the irradiated whole eye samples. The usual calibration, temperature and pressure corrections were made.

The dose in rads was then computed from:

Dose in rads = (0.94)(Victoreen meter reading in Roentgens).

For the low dose exposures a low dose rate was employed. At a focal spot to specimen distance of 25.5 cm, with the aluminum filtration in place, the dose rate was measured to be 400 rads per minute and was uniform across the 12 cm^2 sample area centered on the beam axis. For the high dose exposures a high dose rate was employed. At a focal spot to specimen distance of 18 cm, with the aluminum filtration removed, the dose rate was measured to be 6400 rads per minute and was uniform across the 12 cm^2 sample area centered on the beam axis. The following doses of X-rays were delivered to whole eyes with moistened corneas facing the beam:

Low Dose Range	High Dose Range
10 rads	10,000 rads
100	20,000
500	31,000
750	100,000
1000	
1250	
1500	

During irradiation the eyes were bathed in medium in a 30 mm petri dish lined with cotton. The exposure times ranged from a few seconds to about 16 minutes.

SEM analysis of 50 corneal samples which had received x-ray doses revealed no epithelial plasma membrane lesions. The x-ray irradiated corneal epithelia were indistinguishable from the non-irradiated controls as can be visualized by comparing the SEM micrographs of a typical control (Figs. 10, 11, and 12) with the SEM micrographs of x-ray irradiated corneal samples (Figs. 16-21 in Section VI.B). We are not suggesting that x-ray irradiation does not damage the corneal epithelial cells, but that ionizing photons do not produce plasma membrane lesions in a size range which would be morphologically apparent in SEM micrographs of samples prepared ten seconds post-irradiation.

E. Procedure for Heavy Ion Exposed Corneas

The heavy ion exposures of rat conreas were handled much the same way as the x-ray exposures, but since the heavy ion beam is horizontal rather than vertical a slightly more complicated procedure was adopted in order to maintain corneal wetting. The top surface of a styrofoam block was layered with a single sheet of cotton bandage material. The cotton was soaked in the medium described earlier (Section V.B.). Each whole rat eye was punctured straight through the sclera by a No. 28 hypodermic needle. The eyes were then mounted by sticking the needle with its skewered eye through the cotton into the styrofoam block. The eye was then adjusted down to the medium soaked cotton where it was wetted by capillary action. The styrofoam block with several mounted eyes was then taped to any upright in the beam path and oriented so that the corneas faced the beam.

For those runs with plateau energy particles, a sheet of polycarbonate plastic was situated behind each eye to record the beam fluence passing through the cornea during irradiation (see Section V.C.). Exposure times generally ranged from 1 minute to 2 minutes.

Three heavy ion accelerators were employed at Lawrence Berkeley Laboratory for this work: the 88 inch Cyclotron, the Super Hilac, and the Bevalac (Bevatron/Bevalac, 1977). The heavy ion beams utilized to irradiate corneas were carbon at 474 MeV/amu, neon at at 6 MeV/amu, argon at 3 MeV/amu, and iron at 500 MeV/amu and 600 MeV/amu. The details of each experiment with a particular beam will be presented in Section VI along with the SEM micrographs of the heavy ion irradiated corneas. The micrographs will demonstrate that individual heavy ions are indeed capable of generating lesions in the epithelial plasma membranes. A total of 84 cornea samples were irradiated with the heavy ion beam.

F. Sample Preparation after Irradiation

1. Chemical Fixation

As soon as possible after irradiation, the whole eyes were dropped in beakers of chemical fixative. The most rapid chemical fixation occurs at the outer surface of the eye. The slower fixation of the interior of the eye is due to diffusion rates. But only the outermost surface of the cornea is examined with the SEM, so that the slower fixation of the eye interior is not a hindrance. All cornea epithelia were undergoing chemical fixation within ten seconds post-irradiation.

The fixative solution contains 2.5 percent glutaraldehyde with 0.05 M sodium cacodylate buffer adjusted to pH = 7.2 by addition of an appropriate amount of hydrochloric acid. The measured osmolality of the solution is around 320 milliosmols which is comparable to physiological osmolality for rats. To make 200 ml of the fixative solution, dilute one 10 ml vial of 50 percent glutaraldehyde (Electron Microscopy Sciences) with 190 ml of purified water. Add 2.14 grams of sodium cacodylate powder (molecular weight = 214.02 g, Electron Microscopy Sciences) and stir the solution until the salt dissolves. The pH will be near 7.8. Adjust the pH downward by adding dilute HCl dropwise with stirring until the solution reaches pH = 7.2.

After the samples have been dropped in fixative at room temperature, the fixation beaker is placed in a refrigerator maintained at about 4°C. The two puncture holes in each eye sclera (resulting from the hypodermic needles used for holding the eyes during irradiation) help relieve osmotic pressure build-up in the eye which could stress the cornea. After one day of refrigerated fixation, the beaker is drained and replenished with fresh cold fixative. Following a total fixation time of three days the sample container is removed from the refrigerator and allowed to warm to room temperature.

The eye tissue is quite firm at this point. Each eye is poured out separately onto an inverted petri dish lid which has been filled shallowly with fixative. Break a piece of blue steel razor blade (e.g., Supreme Gold Bond) so that an acutely pointed tip is made. Grasp this blade piece with locking hemostats--this will be employed as a scalpel. Using No. 5 forceps to manipulate the eye so that the cornea is never touched, carefully dissect the cornea from the globe. A new blade should be used for each dissection. The cornea specimen is now ready for dehydration.

Other chemical methods have been employed successfully for the fixation of corneas (Spencer and Hayes, 1970; Freeman and Lai, 1978), and both of these methods use osmium tetroxide as a post fixative. For reasons discussed in Section VIII.D. osmium tetroxide is not used in this work, and the only chemical fixative employed here is glutaraldehyde.

2. Ethanol Dehydration

Sample dehydration is conducted at room temperature. Arrange several small beakers in a row and fill each with 100 ml of graded concentrations of ethanol: 30, 50, 70, 85, 90, 95, and 100 percent ethanol from left to right. Handling the corneas by their edges only, remove from the dissection petri dish and rinse by dipping in pure water. Start the dehydration in 30 percent ethanol for 20 minutes, then 50 percent for 20 minutes, 70 percent for 20 minutes, 85 percent for 15 minutes, 90 percent for 10 minutes, 95 percent for 5 minutes, and finally 100 percent for 5 minutes. While in 100 percent ethanol the rat corneas can be loaded onto screen trays for drying. It is important that the corneas remain completely covered with alcohol while being transported to the dryer.

3. Critical Point Drying

The corneal samples were dried from 100 percent ethanol in a Polaron liquid CO_2 critical point dryer. The duration of drying was one hour, and critical point is achieved at 38°C and a pressure of 1200 psi. In preliminary studies, some control corneas were dried in a freeze dryer for comparison with the critical point dried specimens. Since no difference between the two methods was observed and since the latter is less troublesome, the technique of CO_2 critical point drying was employed throughout this work. A detailed comparison of critical point drying and freeze drying is available elsewhere (Boyde, 1978).

4. Mounting and Sputter Coating

The corneas when removed from the critical point dryer are opaque, cream colored, and textured like plastic. They are ready for mounting on aluminum stubs which are compatible with the SEM. A layer of Pelco silver colloid glue was spread across the top of the aluminum stub, and the cornea specimen was placed in the glue with care taken not to touch or contaminate the anterior corneal surface. The samples on their stubs were stored overnight in a desiccator while the silver glue dried.

A thin layer of metal was deposited on the sample stub after the glue had been allowed to dry. In these experiments, the Hummer Sputter Coater by Technics was used to deposit a gold-palladium alloy layer of 40 to 60 nanometers thickness on each corneal specimen. Once the sample has been metal coated, it can be stored in a desiccator for several weeks before SEM with no observable sample degradation. No further sample preparation is needed.

5. Artifacts and Alternative Protocols

An artifact which will be evident in every SEM micrograph of a corneal surface is due to crystallization of salts from the medium. The amount of crystallization of medium was decreased when eyes were washed in pure water or sodium cacodylate buffer solution just prior to immersion in the chemical fixative. But since it was more important that irradiated samples were fixed within 10 seconds post-irradiation, the washing step was sometimes skipped. The crystals of medium always appear bright in the SEM micrographs, presumably because they are loosely attached to the cornea and cannot rapidly conduct away the charging effects of the SEM beam. The contaminating crystals are typically angular and somewhat larger than the plasma membrane microvilli. They do not interfere with our analysis of heavy ion tracks in the plasma membranes. No other artifacts due to sample preparation were observed.

An alternative fixation protocol that was not attempted in this work but which might work well is a modified Karnovsky fixation (Karnovsky, 1965). The Karnovsky protocol can be followed but with the omission of the step involving osmium tetroxide. The Karnovsky mixed aldehyde fixation is reported to have a greater diffusibility than glutaraldehyde alone and would be well suited for fixation of the deep interior of the eye. However, this type of penetrating fixation was not necessary in this work, since only the outer surface of the cornea was of interest.

G. Use of Scanning Electron Microscopy

1. Important Parameters

The data collecting instrument vital to the success of this research was the SEM operated in the secondary electron detection mode. Two SEM instruments were employed equally: the Coates and Welter Model 50, and the AMR 1000b. A full coverage of the workings of the SEM is not necessary for this work, but a comprehensive discussion of electron optics is available (Goldstein, 1975), and an extensive bibliography on the original papers in electron microscopy has been compiled (Parsons, 1970). In this work we are concerned with the resolution capabilities of the SEM and with how the electron beam interacts with the biological tissue sample. Much of the information presented in this section is taken from Hayes (Hayes, 1973).

The secondary electron detection mode of the SEM is appropriate, because the information sought after in this work is morphological in nature: we hope to view microstructural lesions on the plasma membranes of corneal epithelium. In a standard SEM, the two major limitations on resolution result from the limitations of a demagnified electron beam and the limitations imposed by the interaction volume generated when the energetic electron beam strikes the sample (Hayes, 1973). We will deal first with resolution limitations imposed by the demagnified electron beam.

Even in a system free of all lens aberrations, the minimum diameter of the probing beam is constrained by the Gaussian probe diameter d_o

$$d_o = \left[\left(\frac{4}{0.6\pi\alpha^2}\right)\left(\frac{i}{J_c}\right)\left(\frac{kT}{eV}\right)\right]^{1/2} = \frac{1.46}{\alpha}\left(\frac{ikT}{J_c eV}\right)^{1/2} \tag{81}$$

where α is the half-angle of convergence of the electron beam, i is the probe current, J_c is the emission current density at the cathode, eV is the energy of an electron in the beam, k is Boltzmann's constant, and T is the absolute temperature of the cathode. We see that a cold cathode with a high current density would be ideal, and these conditions are satisfied fairly well by the field emission source (Crewe, 1971). The Coates and Welter instrument employs a field emission source while the AMR instrument uses a lanthanum hexaboride (LaB_6) tip which also produces a high current density but runs hot.

In addition to the minimum beam diameter d_o imposed by electron optical considerations, there are aberrations due to the lenses which include spherical and chromatic aberrations and astigmatism. At present, astigmatism is an operator controlled adjustment though

AMR, Inc. has recently developed a semi-automated stigmator and has plans to fully automate the astigmatism correction (O'Loughlin, 1980). The expressions for the minimum electron beam diameter constrained by spherical and chromatic lens aberrations are

$$\text{spherical, } d_s = \frac{1}{2} C_s \alpha^3 \tag{82}$$

$$\text{chromatic, } d_c = C_c \left(\frac{\Delta V}{V}\right) \alpha \tag{83}$$

where C_s is the coefficient of spherical aberration, C_c is the coefficient of chromatic aberration, and $\frac{\Delta V}{V}$ is the fractional energy spread of the beam. Note the functional relationship of d_s and d_c to the half-angle of convergence α. The final minimum beam diameter is also determined by the diffraction limit with associated diameter given by

$$\text{diffraction, } d_f = \left(\frac{1.22}{\alpha}\right) \left(\frac{h}{m_e V}\right) \tag{84}$$

where h is Plank's constant, m_e is the electron mass, and V is the electron velocity. The quantity h/m_eV is the de Broglie wavelength of the electrons in the beam.

The total minimum electron beam diameter can be calculated by adding equations (81-84) in quadrature

$$d = \left[d_o^{\,2} + d_s^{\,2} + d_c^{\,2} + d_f^{\,2}\right]^{1/2}$$

$$= \left[\left(\frac{2.13}{\alpha^2}\right)\left(\frac{ikT}{J_c eV}\right) + \frac{C_s^{\,2}}{4}\alpha^6 + C_c^{\,2}\left(\frac{\Delta V}{V}\right)^2 \alpha^2 + \left(\frac{1.5}{\alpha^2}\right)\left(\frac{h}{m_e V}\right)^2\right]^{1/2} . \quad (85)$$

With an optimum value of α, a feasible minimum spot size is about 10 nanometers, and the point to point resolution is half that value at 5 nanometers for the secondary electron mode of SEM (Hayes, 1973). This resolution is certainly adequate for the analysis of this work in which a resolution of 50 nanometers would be satisfactory.

The other major consideration of resolution limitation is the manner in which the primary electron beam interacts with the sample. An in depth study of this complicated situation is given in (Goldstein, 1975). Since an electron from the primary beam can lose considerable kinetic energy in a single collision with another electron in the specimen, its trajectory through the specimen will be tortuous. This creates a volume of interaction in the specimen, and secondary electrons can be emitted from any location in the interaction volume. For low energy electron beams and high Z specimen materials the shape of the interaction volume will be cup-like, and for high energy electron beams in low Z materials the shape will be pear-like (Everhart, et al., 1972). Those secondary electrons which are emitted close enough to the specimen surface may escape the specimen and be collected as part of the signal; energetic secondary electrons can penetrate about 10 nanometers of material. This has the effect of averaging the signal intensity over an area which is larger than the beam spot size. Thus, the interaction volume can be a greater limitation to resolution than the spot size of the beam. The effective collection diameter is about 10 nanometers or more for an SEM in the secondary electron mode of operation (Hayes, 1973).

2. Sources of Artifacts

The local dose rate of an electron beam probing a sample can achieve values as high as a million rads per minute. If the beam is left in one location on the sample for a long enough duration, the sample can undergo severe degradation. This is particularly serious for high magnification work, because the beam will be scanning a smaller area of the sample thus concentrating the dose and consequently increasing the radiation damage. Figure 15 will demonstrate this point. A sample of rat cornea is scanned by the electron beam at six different magnifications beginning with the lowest magnification and progressing stepwise to the highest magnification spending ten minutes at each magnification step. The concentric rectangles are the scan frame perimeters for each magnification setting. Clearly, the corneal epithelium has been seriously damaged by the electron beam to the extent that a hole has been "burned" through the epithelium. Such artifactual holes and indentations would surely interfere with a search for membrane lesions on the corneal epithelium. But a skilled microscopist can easily avoid this pitfall by conducting most of the analysis at low magnification, using high magnification only when needed and then shooting the micrograph quickly. The corrections for astigmatism and focusing at high magnification can be accomplished on

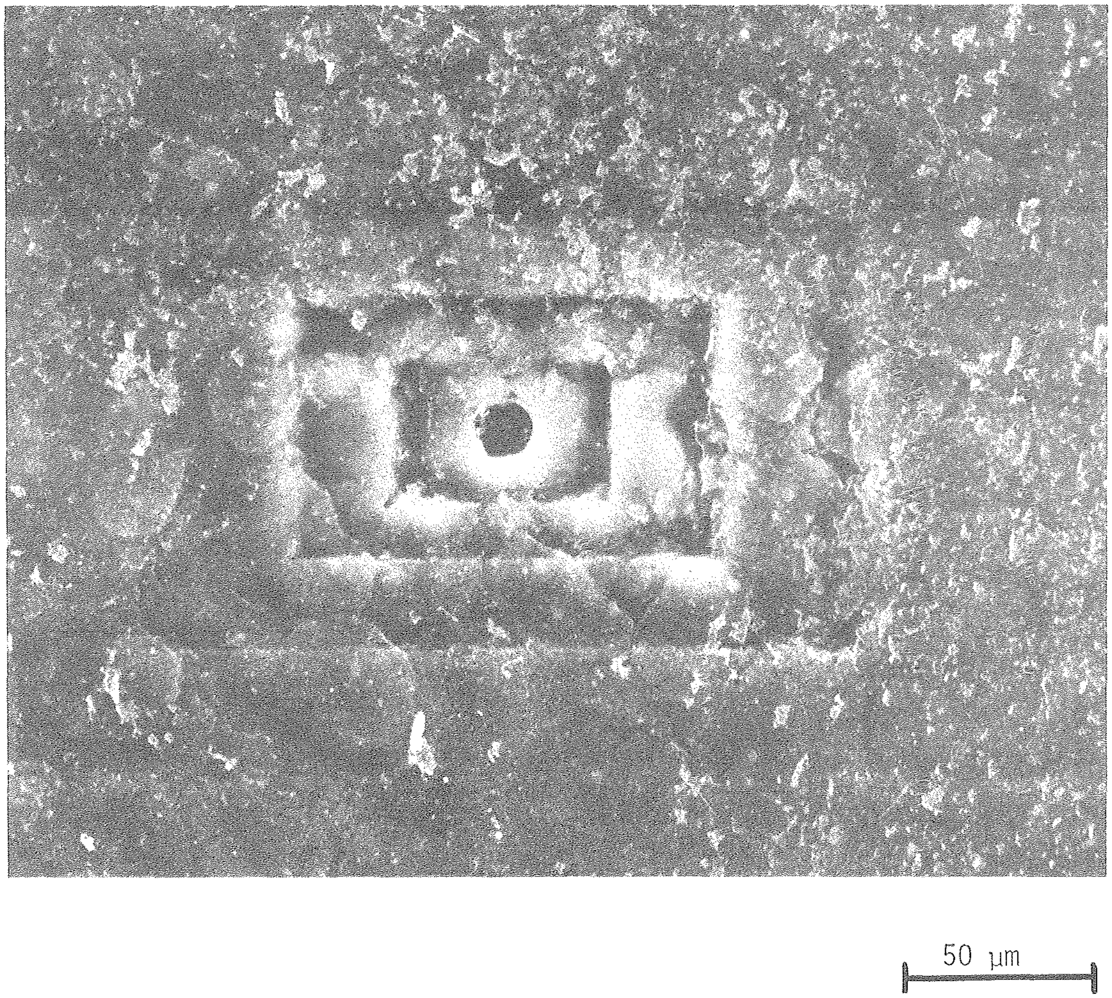

XBB806 7669

Figure 15. SEM micrograph of corneal epithelium showing radiation damage caused by the probing electron beam. Each rectangle is the perimeter of the scan frame for a particular magnification setting, the lowest magnification giving the largest frame. The sample was held for 10 minutes at each setting.

an area of the specimen which is not of interest before moving the specimen surface into position for the micrograph. Radiation damage by the electron beam was not a problem in this work.

It should be added that all of the SEM for this work was done at an accelerating voltage of 20 kV and a beam current around 20×10^{-12} amps.

VI. RESULTS FROM SEM

A. Controls

All of the controls were examined under SEM at three different magnifications for each area of interest. In most cases, the magnification settings were 250x, 500x, and 2000x. Fifty separate corneal specimens were scanned to generate 150 micrographs of non-irradiated rat corneal epithelium. Since the magnification settings are cumbersome when size is the parameter of concern, each SEM micrograph is displayed with a dimension bar in the lower right corner for size referencing. The dimension bar can always be measured to redetermine the image magnification if need arises.

It would be redundant to present all of the control micrographs, since they all look alike. Refer back to Figs. 10, 11, and 12 for examples of non-irradiated control corneas. Note in particular that the corneal epithelium is fairly smooth, that the epithelial cells are squamous with nuclei protruding, that the plasma membrane surface of an epithelial cell is covered with microvilli, and that there are no sporadic dents, bumps, or holes in the size range of a micrometer. Some measurements characteristic of the rat corneal epithelial cells are:

average cell diameter = 30 to 40 μm
average nuclear diameter = 8 to 10 μm
average microvilli diameter = 0.2 μm
average cell thickness = 2 μm.

B. X-ray Experiments

The protocol for the x-ray irradiation of corneal epithelium is detailed in Section V.D. The x-ray exposed corneas appear no different from the controls; there is no evidence of radiation induced membrane lesions in any of the x-ray exposed corneas even for x-ray doses of 100,000 rads.

Figures 16, 17, and 18 are a series of micrographs looking at the same corneal region but at different magnifications. The cornea in these three micrographs was given an x-ray dose of 500 rads. The bright speck in the center of Fig. 16 is a piece of contamination which was used in focusing the image. The patchwork appearance of the epithelium is due to varying degrees of cell surface microvilli. In the bottom left of the micrograph is the bright edge of a single cell caught in the process of desquamation. Figure 17 is a higher magnification of the same corneal sample with the contamination speck at center left. Here the overlapping arrangement of epithelium is more evident. We see no indication of membrane lesions at this magnification, so let us look at a single cell more closely. Figure 18 is a single epithelial cell of the same sample which received an x-ray dose of 500 rads. The nuclear region is located in the upper center of the micrograph. The borders of the cell are easily visible, and one can observe different concentrations of cell surface microvilli on adjacent cells. Even at this magnification we do not observe membrane lesions due to the irradiation with x-rays.

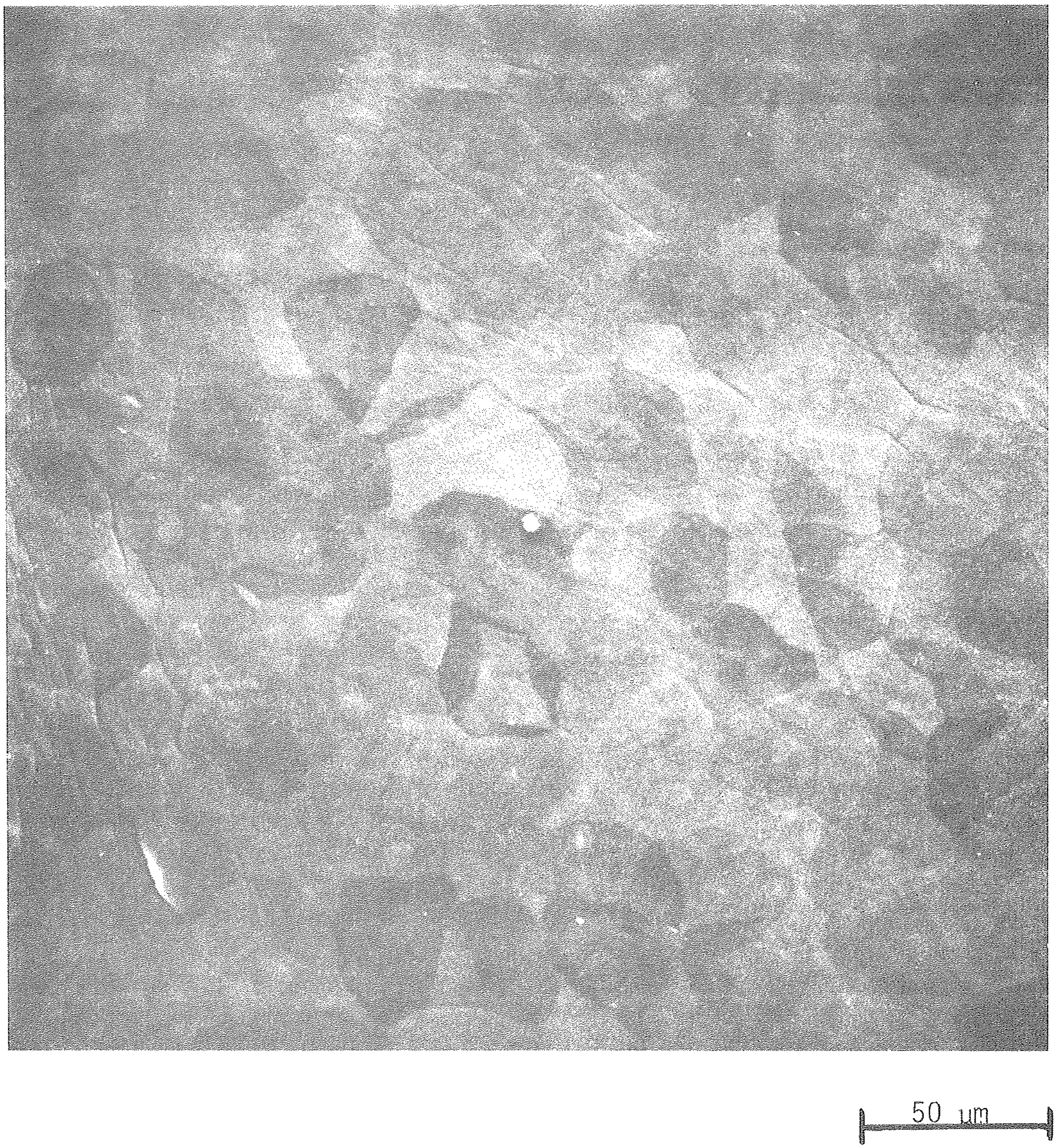

XBB 805-6604

Figure 16. SEM micrograph of corneal epithelium which received an x-ray dose of 500 rads. The central speck of contamination was used in focusing the image.

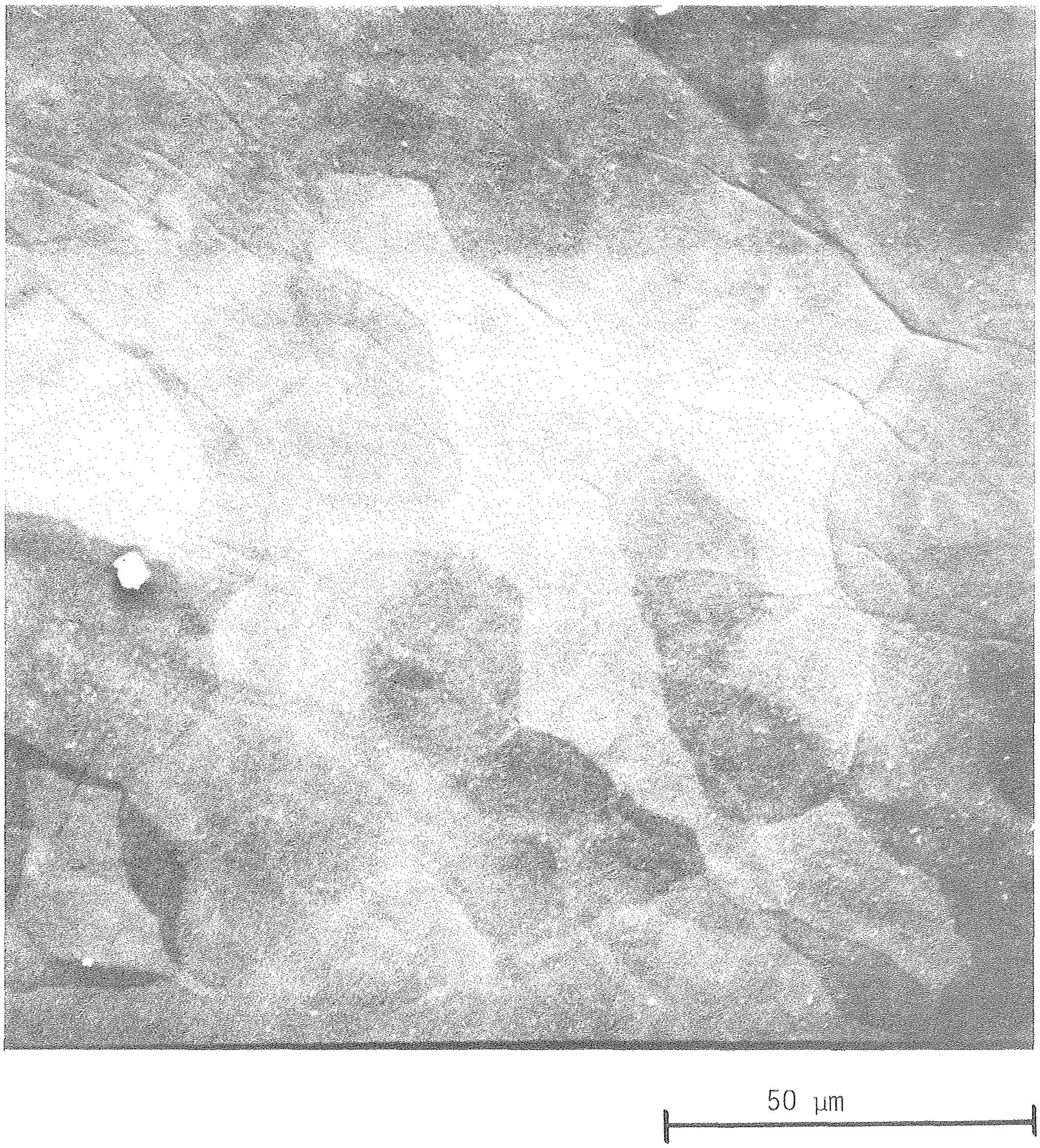

XBB 805-6605

Figure 17. SEM micrograph of corneal epithelium which received an x-ray dose of 500 rads. The speck at center left is contamination.

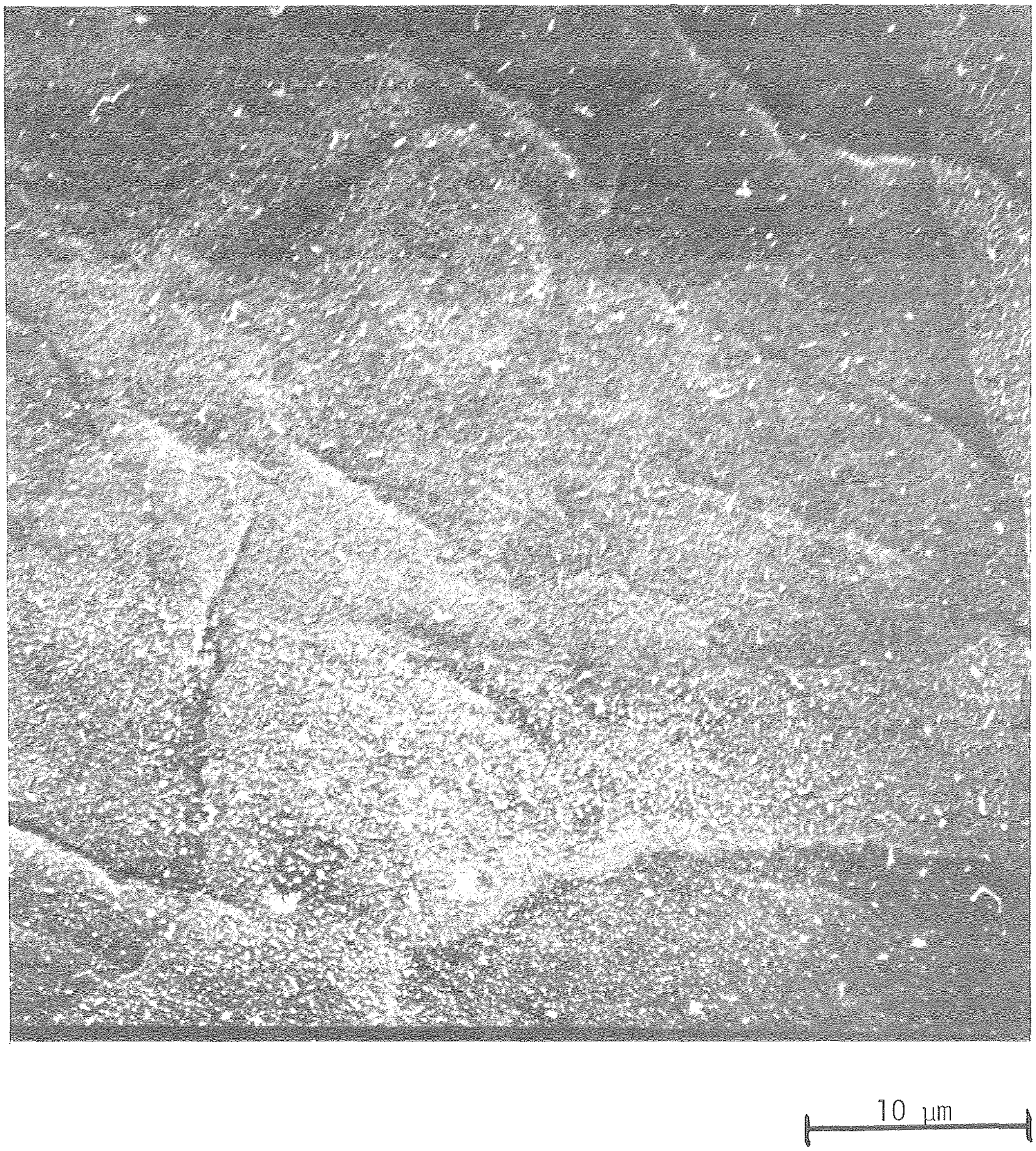

XBB 805-6606

Figure 18. SEM micrograph of a single corneal epithelial cell from a sample which received an x-ray dose of 500 rads. The nuclear bump is in the upper center. The bright specks are contamination crystals.

We now examine a series of micrographs for a cornea which received an x-ray dose of 100,000 rads, Figs. 19, 20, and 21. The low magnification micrograph, Fig. 19, shows several cells undergoing desquamation, and one cell toward the upper right has been shed nearly completely. Desquamation is normal for a healthy corneal epithelium, because the tissue is highly regenerative (Section IV.C.). The contaminating crystals of medium are larger in this image. A higher magnification of the desquamating cell region is shown in Fig. 20. A single cell from the same area is magnified in Fig. 21. The contamination crystals are quite apparent. The amount of surface microvilli is noticeably different from cell to cell, and this is a manifestation of differing cell ages (Section IV.C.). Again we do not observe any evidence of plasma membrane lesions for an x-ray dose as high as 100,000 rads.

We have seen micrographs for an x-ray dose of 500 rads and an x-ray dose of 100,000 rads to the cornea. Several other x-ray doses were delivered (Section V.d.), and the micrographs are all similar. In this work there is no observable plasma membrane effect due to x-rays when corneas are fixed within 10 seconds post-irradiation, and the irradiated rat corneas have the same appearance as the non-irradiated controls. We conclude that corneas do not immediately manifest microstructural damage as morphological changes when irradiated with x-rays and observed under SEM at the magnification levels used in this work. If we were to examine cells a few days post-irradiation rather than at 10 seconds as in this work, we might

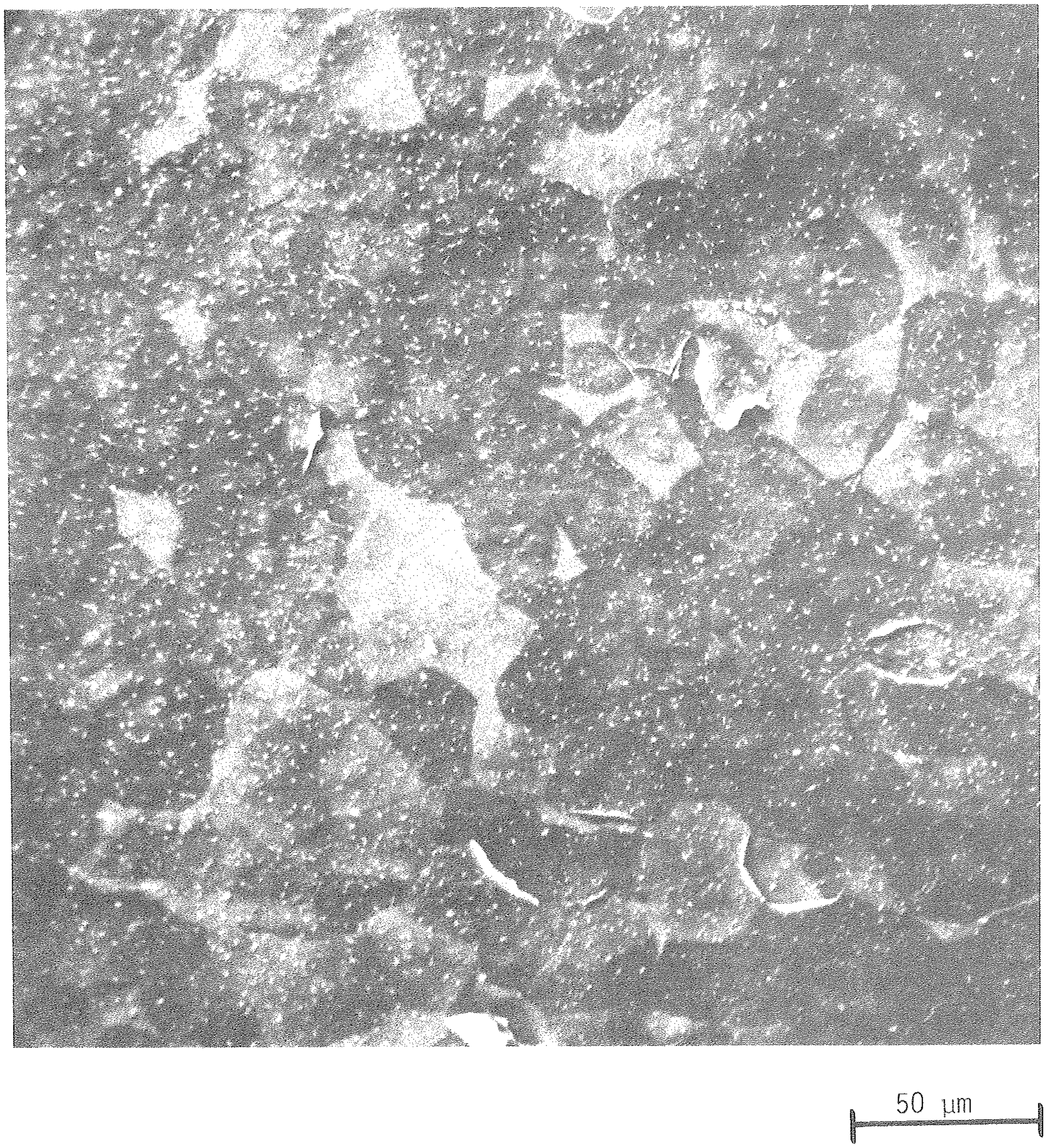

Figure 19. SEM micrograph of corneal epithelium which received an x-ray dose of 100,000 rads. Several cells are undergoing desquamation. Crystalline contamination is present.

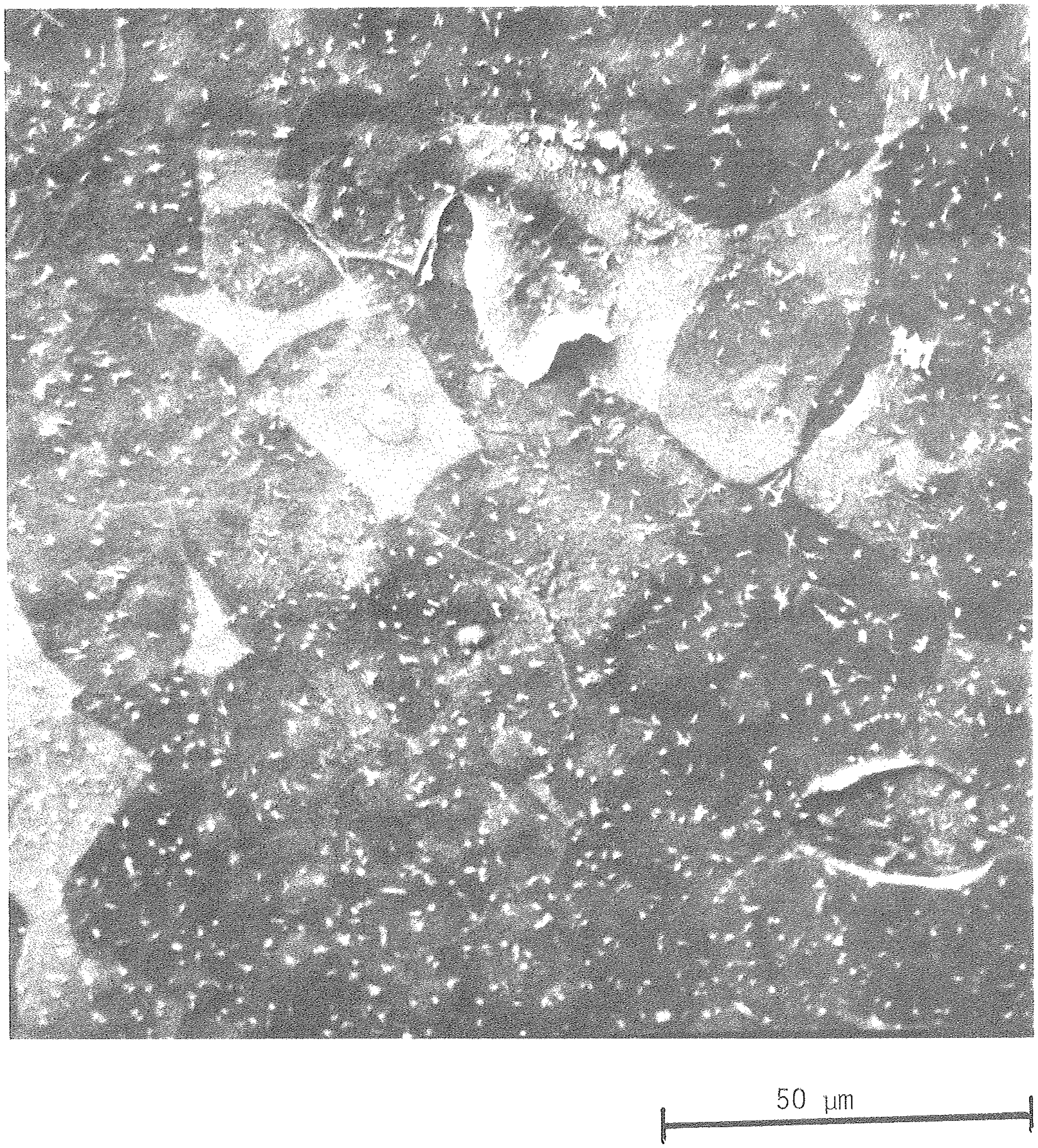

XBB805 6611

Figure 20. SEM micrograph of corneal epithelium which received an x-ray dose of 100,000 rads. A nearly desquamated cell is in the upper center.

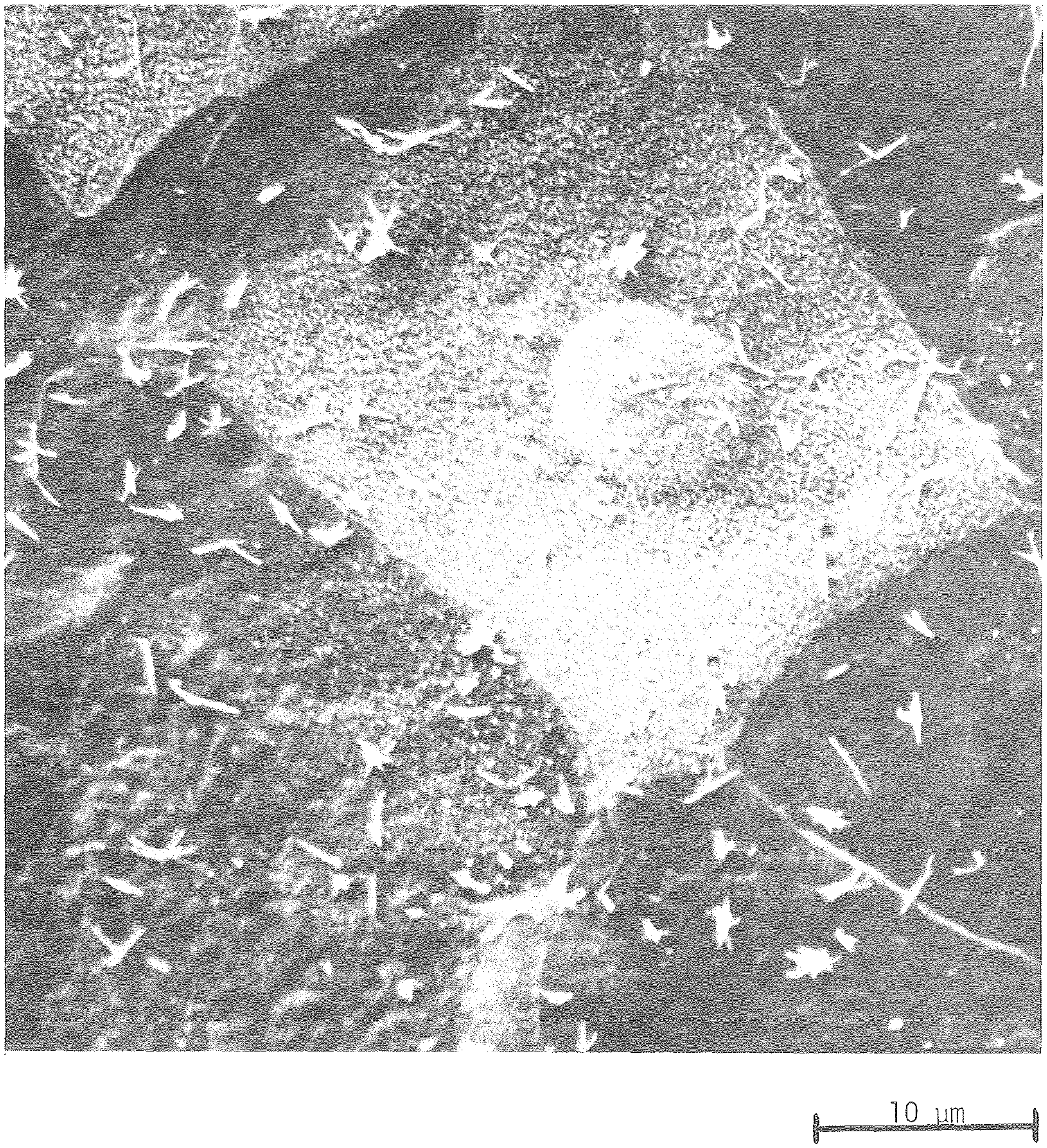

XBB 805 6610

Figure 21. SEM micrograph of a single corneal epithelial cell which received an x-ray dose of 100,000 rads. Note the differences in surface microvilli between cells. The contamination crystals are apparent.

discover some morphological indication of radiation damage because we know that 600 rads of x-rays is sufficient to kill mammalian cells. It is therefore important to consider the time scale of radiation damage in biological tissue, and this will be addressed in Section VIII.A.

C. Heavy Ion Experiments

A total of 84 corneal samples were irradiated by different heavy ions at various energies. The techniques employed in these experiments are discussed fully in Section V.E. Several SEM micrographs will be presented, but rather than displaying the usual three step magnification series, only the micrograph with a magnification well suited to display the membrane lesions will be chosen for reproduction here. Membrane lesions were indeed observed for nearly every heavy ion irradiation, and the diameter and surface concentration of membrane lesions were different for each heavy ion used.

Let us begin with a carbon beam experiment run at the LBL Bevatron. The energy of the beam was 474 MeV/amu, and the carbon atoms were fully stripped of their electrons giving each heavy ion a +6 charge. The carbon ions are in the plateau region of the Bragg curve, and polycarbonate plastic sheets were mounted behind each eye to record the beam fluence. The linear energy transfer (LET) of carbon ions at 474 MeV/amu is about 18 KeV/μm (see Section III.A.1. for discussion on LET), and this is a relatively low value. Upon scanning the corneal epithelial surface with the SEM, plasma membrane lesions were discovered. Figure 22 is a miocrograph of a membrane region in which

XBB 805-7685

Figure 22. SEM micrograph of a corneal epithelial cell plasma membrane which was irradiated with 474 MeV/amu carbon ions. The membrane lesions measure about 0.08 μm in diameter. Round bumps are microvilli and rod shapes are contaminant crystals.

several lesions are visible as small holes whose diameters measure about 0.08 μm. The round bumps are membrane microvilli, and the larger rod shapes are due to contamination by crystalline growth medium. All actual measurements in this section are tabulated with appropriate statistics in Section VII.A. and B.

A higher magnification of a different carbon irradiated sample is shown in Figure 23. Again the lesions measure about 0.08 μm in diameter. The beam fluence for this run was measured on the etched plastic to be about $10^8/cm^2$ or approximately 1 particle/μm^2. The surface concentration of membrane lesions is about $10^8/cm^2$ measured directly from the micrograph (Section VII.A.), and this agreement with beam fluence suggests that a single heavy ion generated a single lesion; the plasma membrane has suffered microstructural damage due to the heavy ion track. Let us summarize this run (data elaboration is in Sections VII.A. and B.):

Carbon Ions

Energy = 474 MeV/amu
Charge = +6
LET ≅ 18 KeV/μm
Fluence ≅ $10^8/cm^2$
Lesion ≅ 0.08 μm

The next two series of experiments were done with iron particles at 500 and 600 MeV/amu at the Bevalac. AT both these energies the heavy ions are in the plateau region of the Bragg curve, so plastic can be used to monitor the beam fluence. The LET of the fully stripped +26 charged iron particles is about 220 KeV/μm for the 500 MeV/amu particles and 180 KeV/μm for the 600 MeV/amu particles.

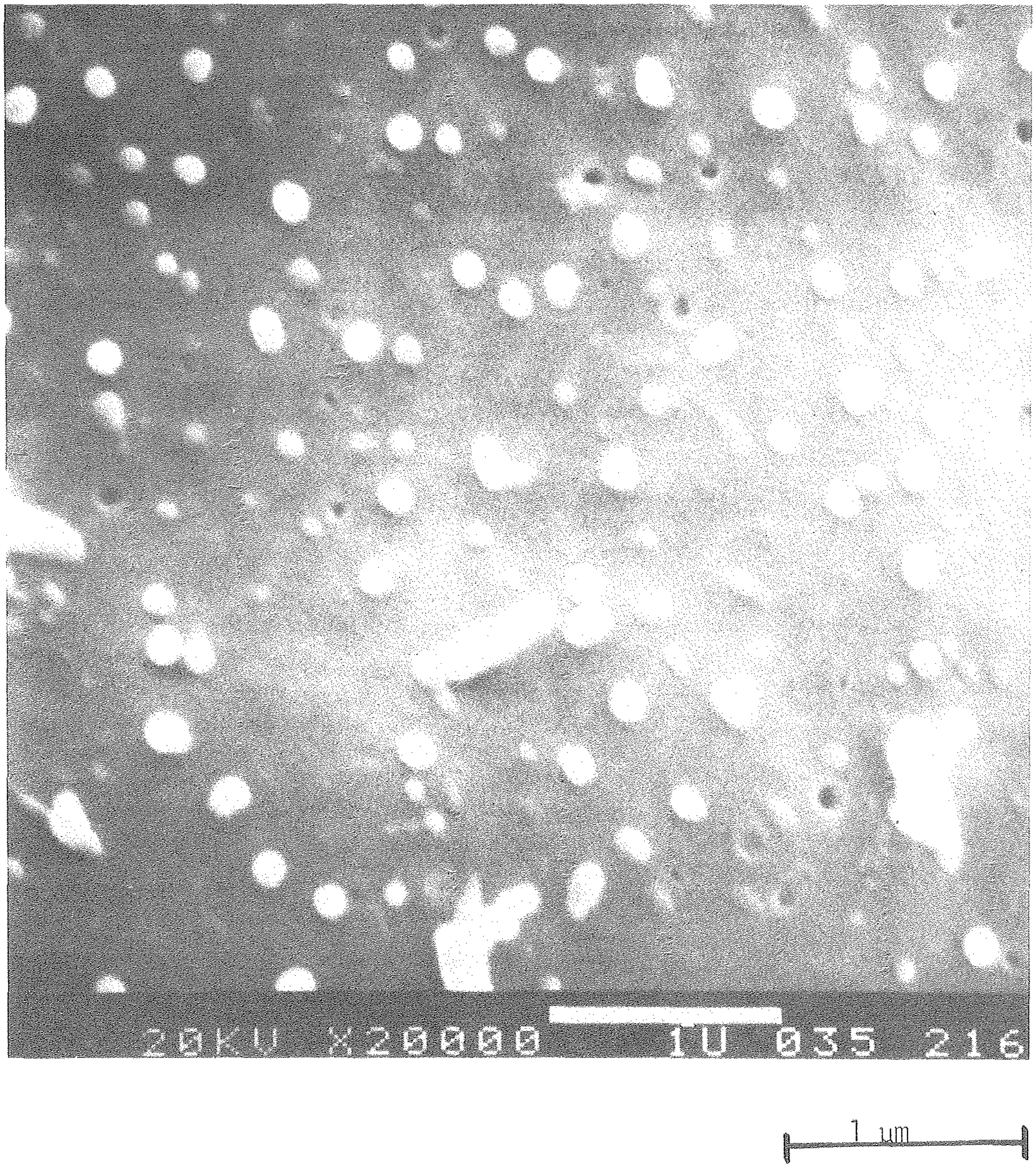

XBB805 6621

Figure 23. SEM micrograph of a corneal epithelial cell plasma membrane which was irradiated with 474 MeV/amu carbon ions. The membrane lesions measures about 0.08 μm in diameter.

Figure 24 is a micrograph of the plasma membrane surface with one prominent lesion presumably cuased by a single 500 MeV/amu iron particle. The lesion diameter measures about 1 μm. Unfortunately, the beam fluence for this run was only about $10^2/\text{cm}^2$, so that a good correlation between beam fluence and lesion concentration is not possible. We can suggest however that because the number of lesions per unit area of epithelium was low and since no such lesions occurred in control or x-ray irradiated samples, the lesions are likely the result of heavy ion bombardment.

Figures 25 and 26 are micrographs of lesions which occurred on corneal samples irradiated with iron at 600 MeV/amu. The beam fluence measured from the etched plastic was about $10^4/\text{cm}^2$, and with some difficulty a correlation could be made between the beam fluence and the surface concentration of membrane lesions. The lesions from 600 MeV/amu iron particles measure about 0.8 μm in diameter. (See Sections VII.A. and B. for actual data).

For both iron beam runs it is suggested that the observed membrane lesions are due to microstructural damage along the track of individual iron particles. Let us summarize the two iron runs:

<u>Iron Ions</u>

Energy	=	500 MeV/amu	600 MeV/amu
Charge	=	+26	+26
LET	≅	220 KeV/μm	180 KeV/μm
Fluence	≅	$10^2/\text{cm}^2$	$10^4/\text{cm}^2$
Lesion	≅	1.0 μm	0.8 μm

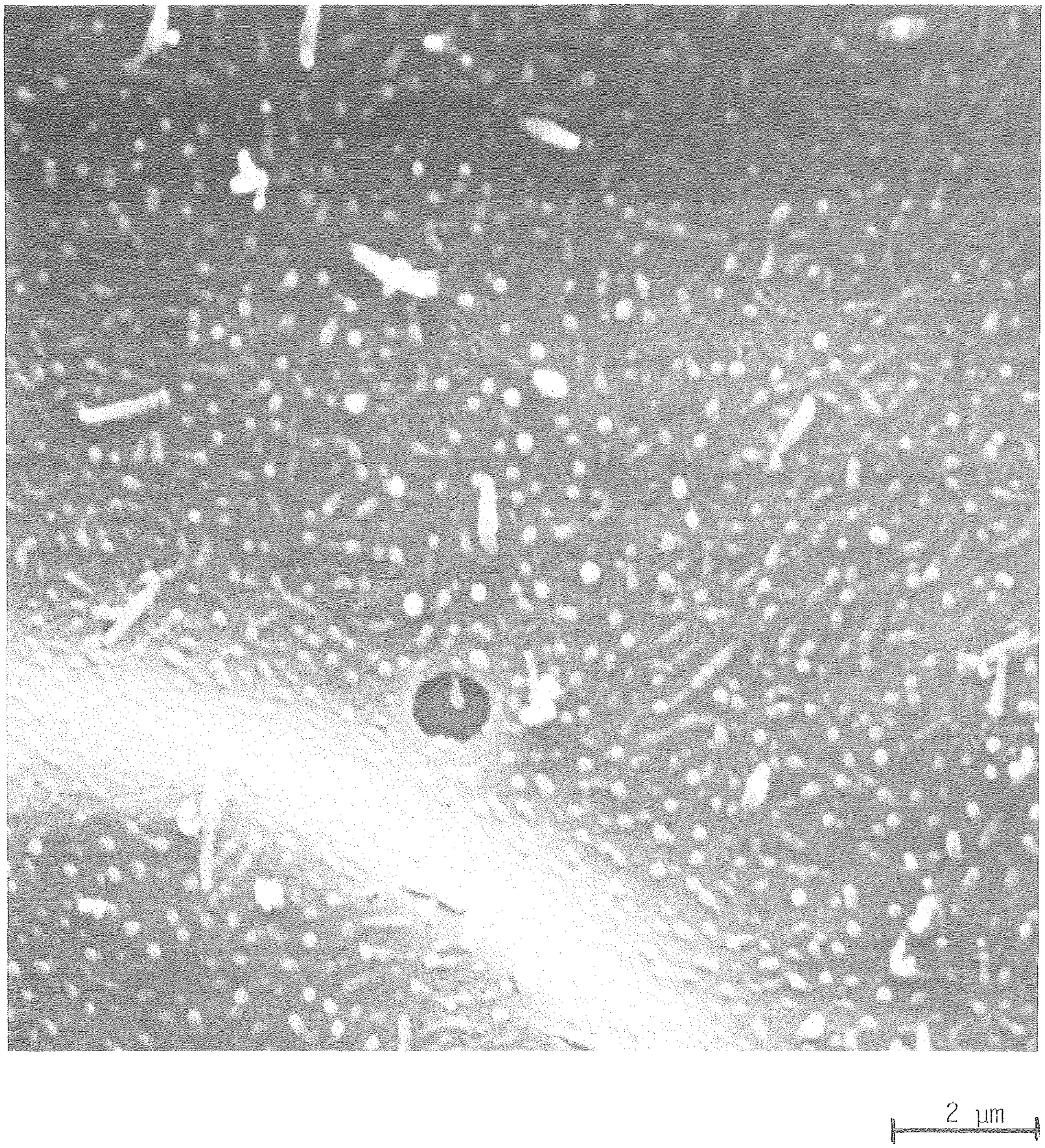

XBB 790-14743

Figure 24. SEM micrograph of plasma membrane of corneal epithelium irradiated with 500 MeV/amu iron particles. Lesion diameter measures 1 μm.

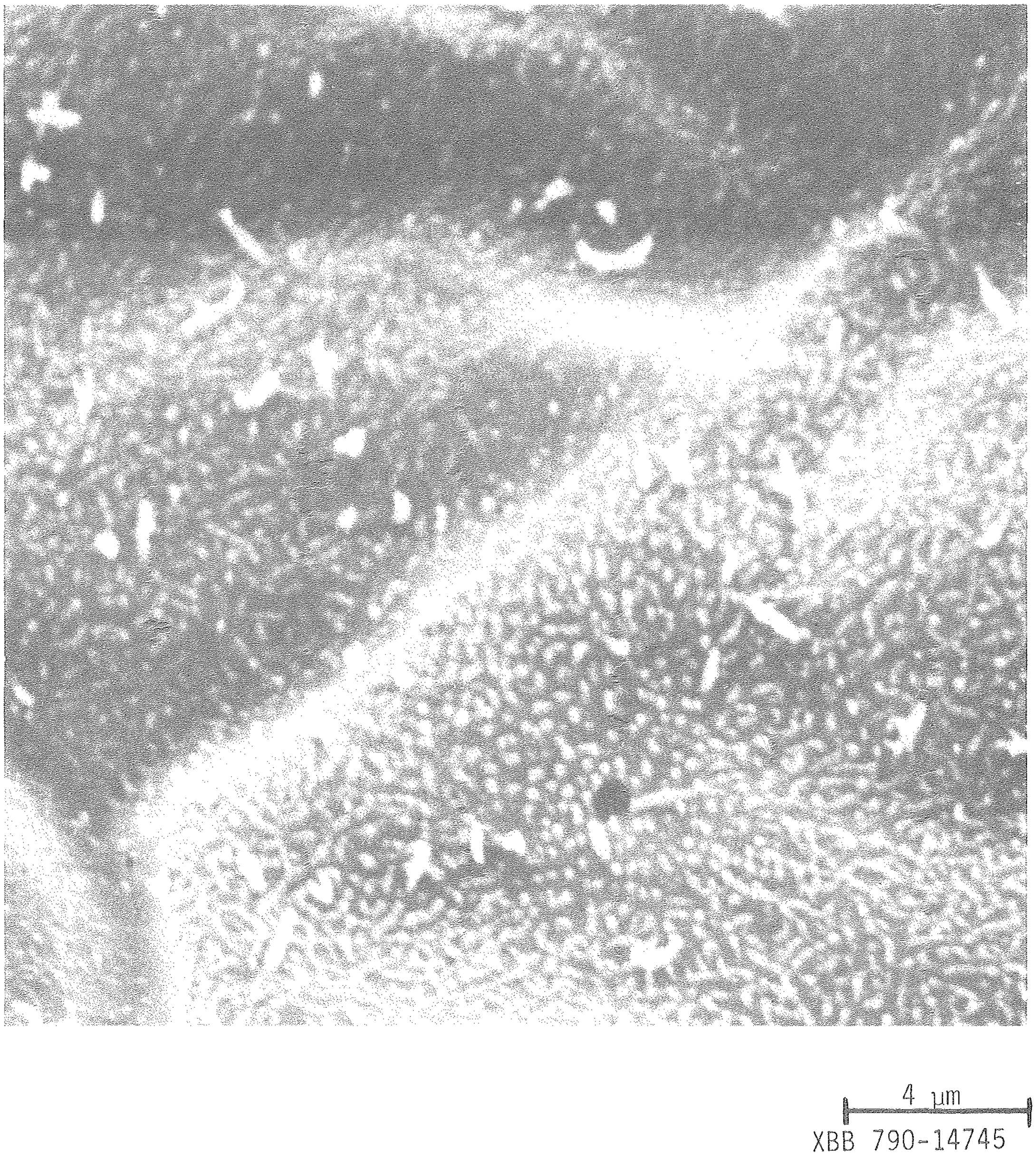

Figure 25. SEM micrograph of cornea irradiated with 600 MeV/amu iron particles. The lesion diameter measures 0.8 μm.

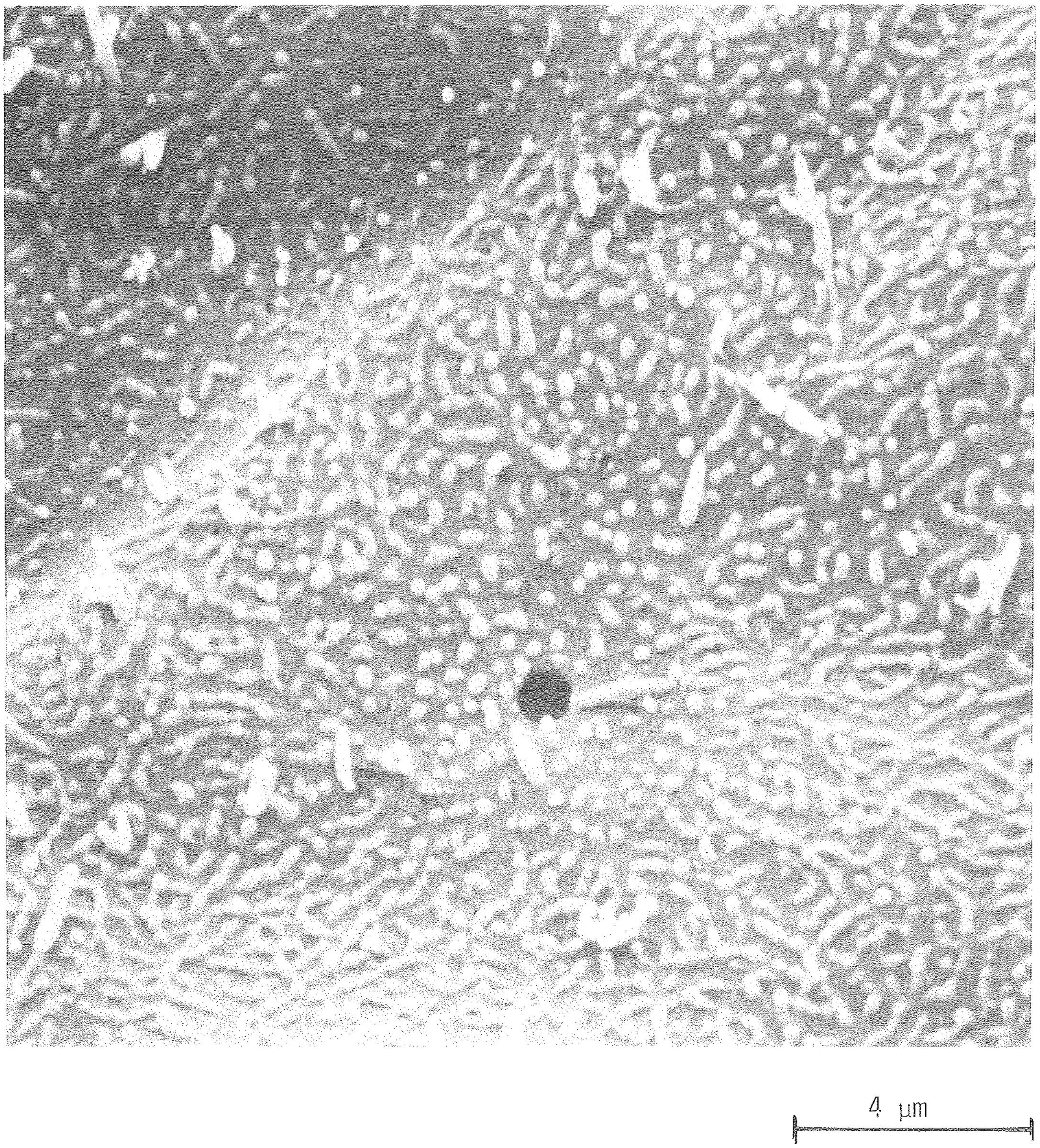

XBB 790-14744

Figure 26. SEM micrograph of cornea irradiated with 600 MeV/amu iron particles. The lesion diameter is 0.8 μm.

Another experiment used the LBL Super Hilac to accelerate neon particles to irradiate the corneas. Here the energy was initially 8.5 MeV/amu, but by the time the neon particles reach the sample the energy is closer to 6 MeV/amu. Because these particles are moving much more slowly than the previous beams, they have time to pick-up a few electrons. Each neon ion had a partial charge of about 8.7. The LET for these particles is about 600 KeV/μm. The neon ions at 6 MeV/amu will penetrate only a few micrometers into the eye, so that plastic cannot be employed to measure beam fluence. Plastic in front of the eye might stop the particles before they reach the eye. Instead the fluence was determined from the known dose by the calculation method detailed in Section VII.A. This calculation gave a beam fluence for neon of about $10^4/\text{cm}^2$. Approximately one membrane lesion every 10,000 μm^2 (this is equivalent to one lesion in a square area 100 μm on a side) of epithelial surface was present, and this is equivalent to a fluence of $10^4/\text{cm}^2$ (see Section VII.A. for details).

Figure 27 displays a single epithelial lesion in a neon irradiated cornea. The lesions from 6 MeV/amu neon ions were rather large and typically measured about 2.5 μm in diameter.

Figures 28 and 29 also show membrane lesions due to irradiation with 6 MeV/amu neon. These lesions are about 2.5 μm in diameter. Because of an excellent agreement between the neon beam fluence and the surface concentration of membrane lesions (Section VII.A.), we conclude that each 2.5 μm lesion is due to an individual neon ion. Let us summarize the results for neon:

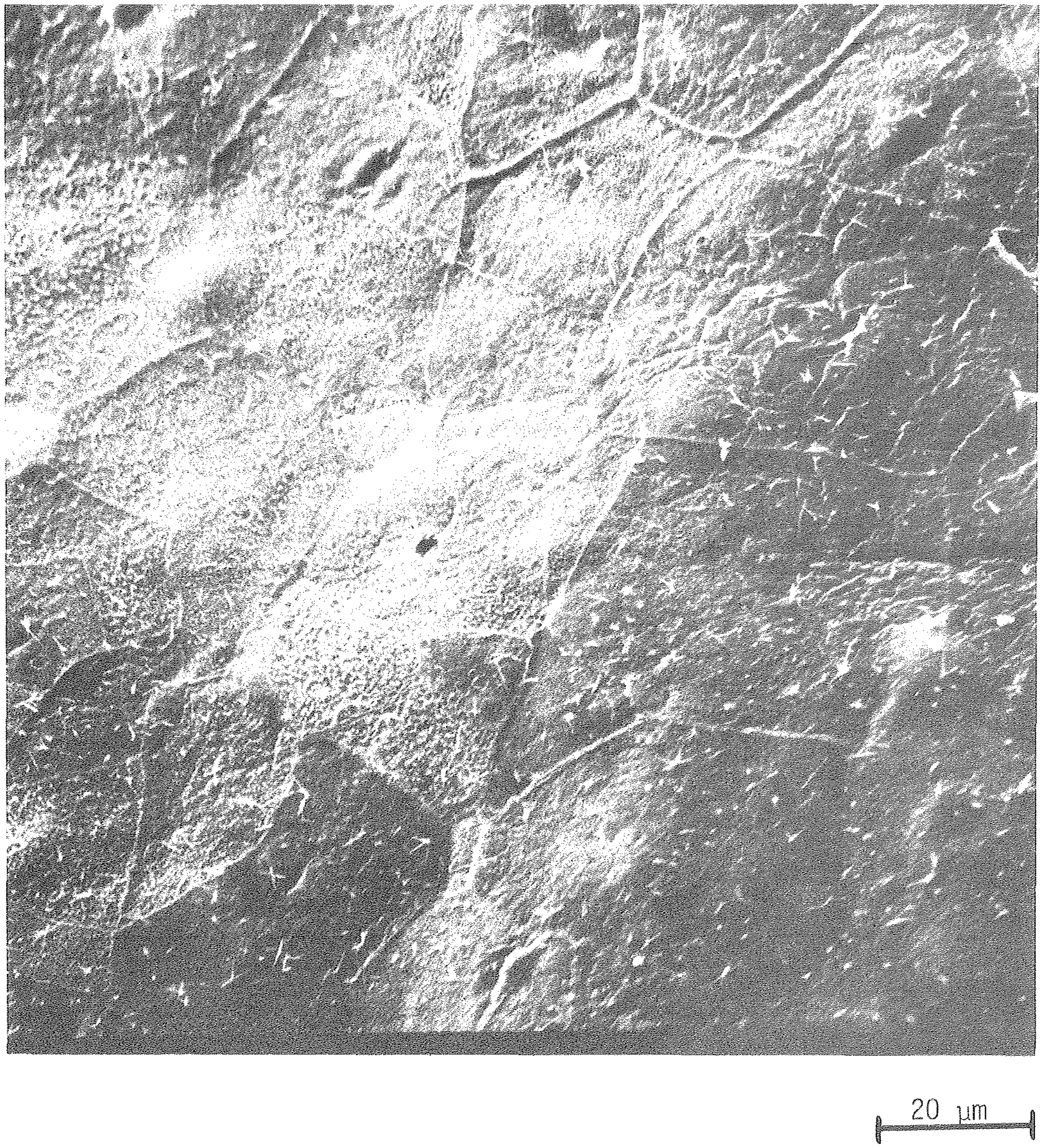

XBB 805-6618

Figure 27. SEM micrograph of cornea irradiated with 6 MeV/amu neon particles. Lesion diameter is 2.5 μm.

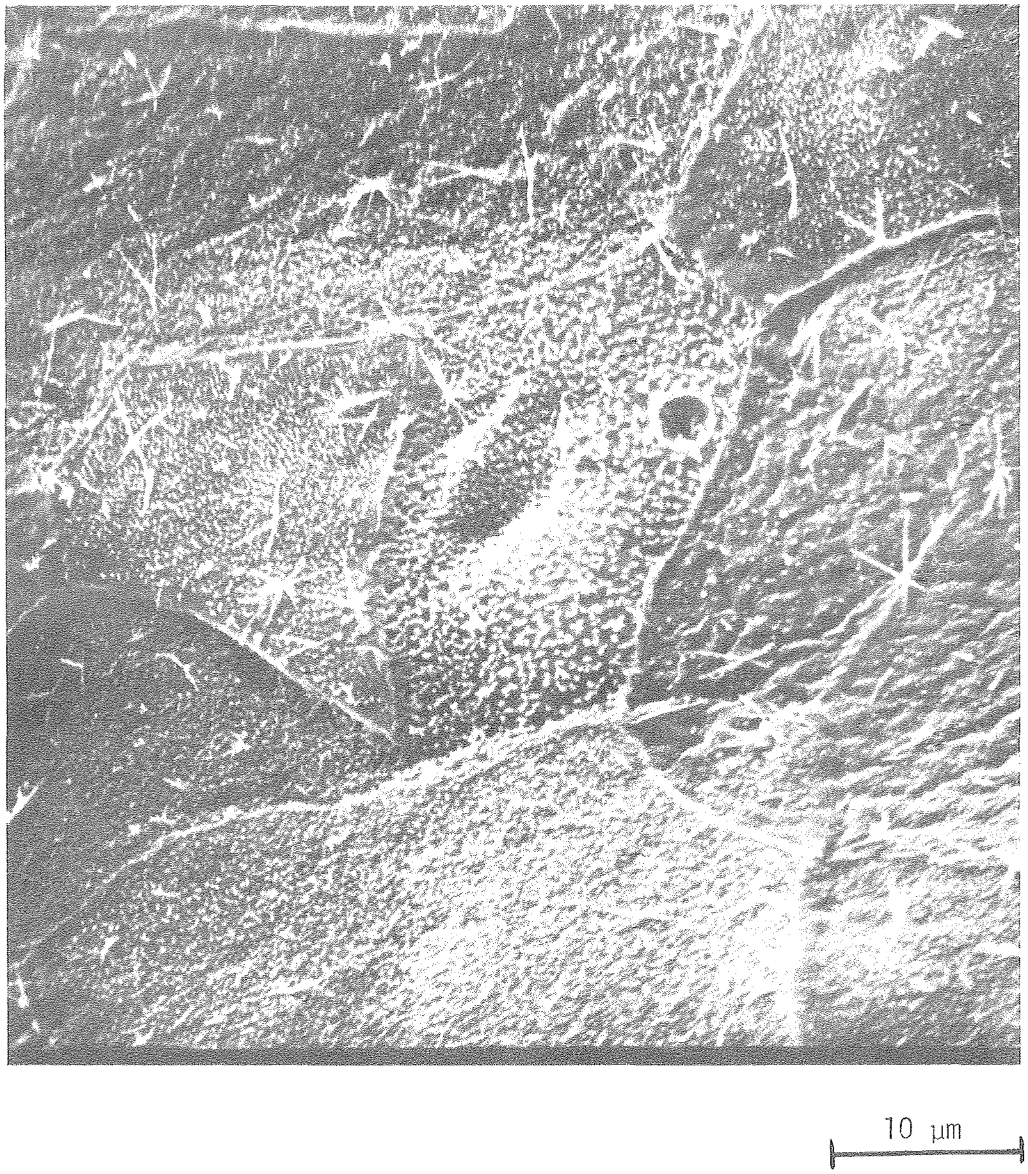

XBB 805-6617

Figure 28. SEM micrograph of cornea irradiated with 6 MeV/amu neon particles. Lesion diameter measures 2.5 μm.

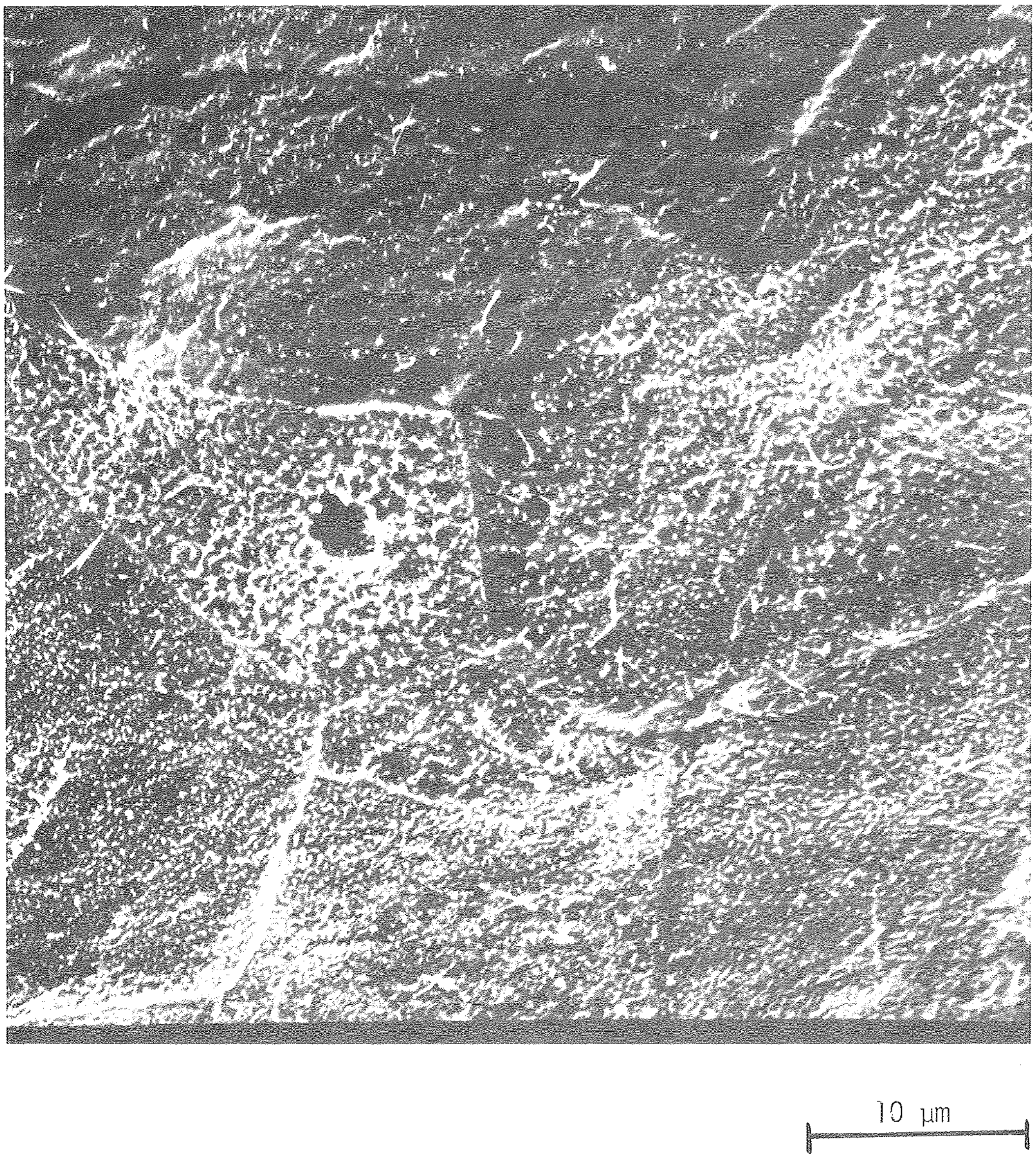

XBB 805-6614

Figure 29. SEM micrograph of cornea irradiated with 6 MeV/amu neon particles. Lesion diameter measures 2.5 µm.

Neon Ions

Energy = 6 MeV/amu
Charge = +8.7
LET ≅ 600 KeV/μm
Fluence ≅ $10^4/cm^2$
Lesion ≅ 2.5 μm

The most dramatic results were obtained with argon from the Super Hilac. Again the particle energy is initially 8.5 MeV/amu, but by the time the ion strikes the sample its energy is reduced to 3 MeV/amu. The LET for 3 MeV/amu argon ions is near 1800 KeV/μm, and the partial charge remaining on the ion is about 15.6. The fluence was calculated from the dose to be $10^6/cm^2$ (Section VII.A.).

Figure 30 illustrates several lesions in the corneal epithelium. These lesions are enormous measuring about 5 μm in diameter, roughly half the diameter of an epithelial cell nucleus. Toward the center of the micrograph are two well outlined nuclei for size reference. The lesions appear to be dents rather than holes as were found in the previous experiments, and this topic will be examined in Section VIII.C.

We can count about one membrane lesion every 100 μm^2, corresponding to a surface concentration of $10^6/cm^2$ as measured from the cornea micrograph. Since this figure agrees with the beam fluence, the conclusion seems inescapable that a single argon ion is generating a single membrane lesion. This is statistically verified in Section VII.

Figures 31 and 32 are higher magnifications of membrane lesions to show their dent-like structure more clearly.

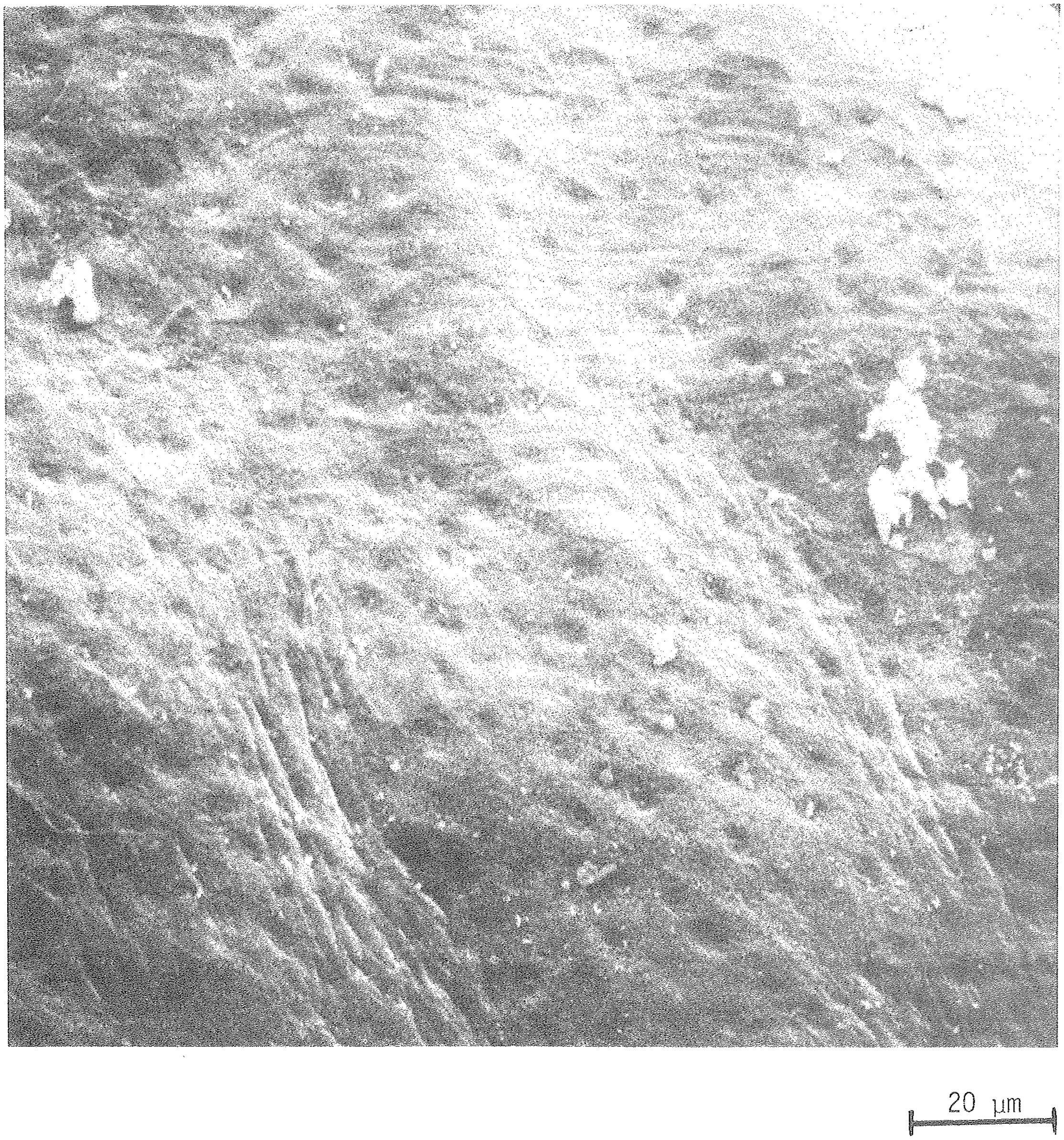

XBB 806-7689

Figure 30. SEM micrograph of cornea irradiated with 3 MeV/amu argon particles. Lesion diameters measures about 5 µm.

XBB806 7690

Figure 31. SEM micrograph of cornea irradiated with 3 MeV/amu argon particles. Lesion diameter measures about 5 μm.

XBB 790-14734

Figure 32. SEM micrograph of cornea irradiated with 3 MeV/amu argon particles. Lesion diameter is about 5 μm.

A micrograph with a different orientation and from a different sample irradiated under the same conditions as above helps visualize the heavy ion lesions, Fig. 33. Epithelial cell perimeters and nuclear outlines are well delineated. Again the lesions are about 5 μm in diameter.

Figure 34 is an enlargement of Fig. 33 to show more detail of the dent-like lesions caused by irradiation with argon ions.

A different run with the same argon beam yielded similar results, Fig. 35. The surface concentration of plasma membrane lesions is easily counted to give about one lesion every 100 μm^2 or $10^6/cm^2$ which is approximately the same as the beam fluence. Thus a one to one correspondence between heavy ions in the beam and lesions in the cornea is implied. The lesion diameters are 5 μm in this sample as in the previous argon samples. Let us summarize the results for argon.

Argon Ions

Energy = 3 MeV/amu
Charge = +15.6
LET ≅ 1800 KeV/μm
Fluence ≅ $10^6/cm^2$
Lesion ≅ 5 μm

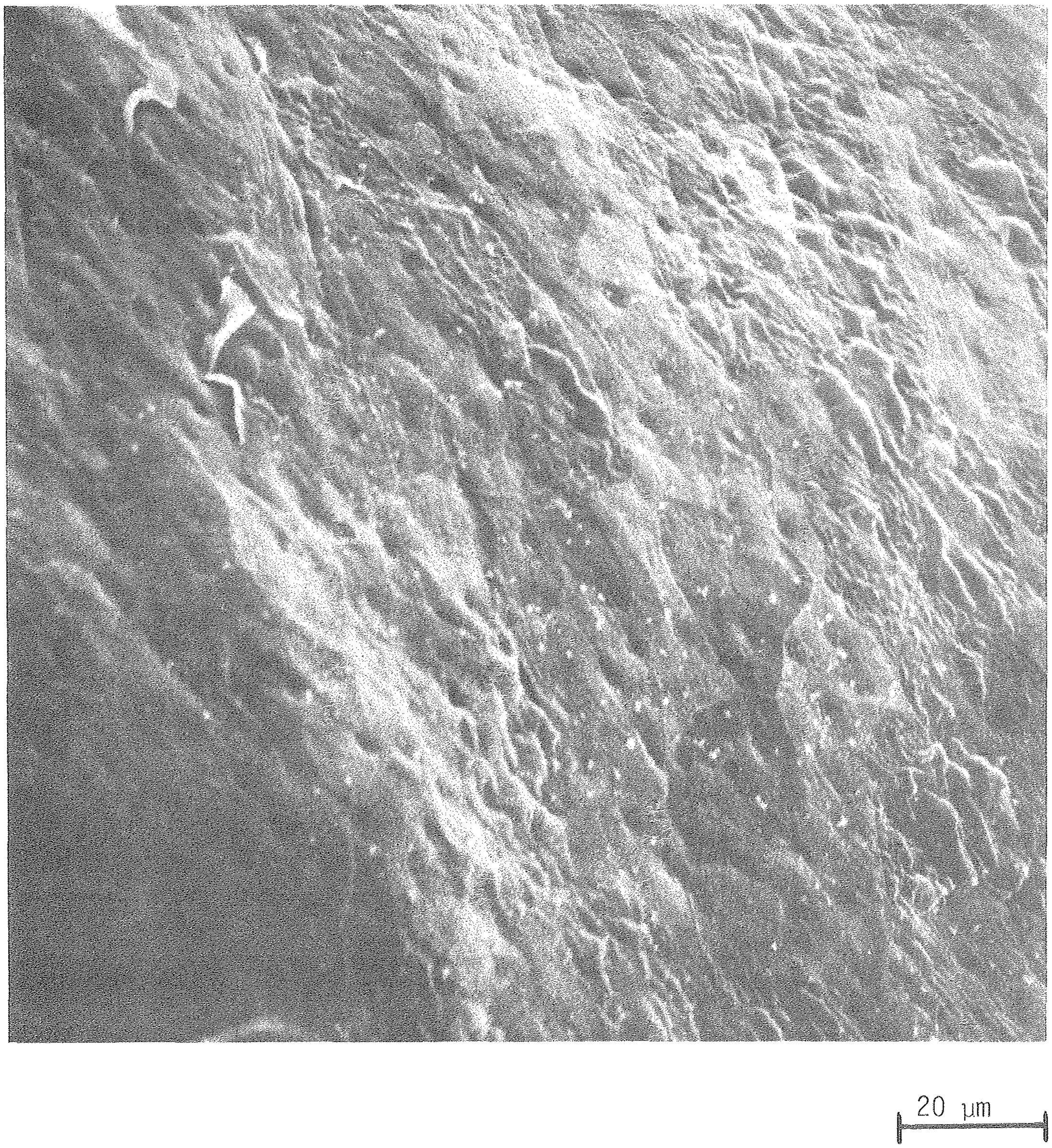

XBB806 7688

Figure 33. SEM micrograph of cornea irradiated with 3 MeV/amu argon particles. Lesion diameter is about 5 μm.

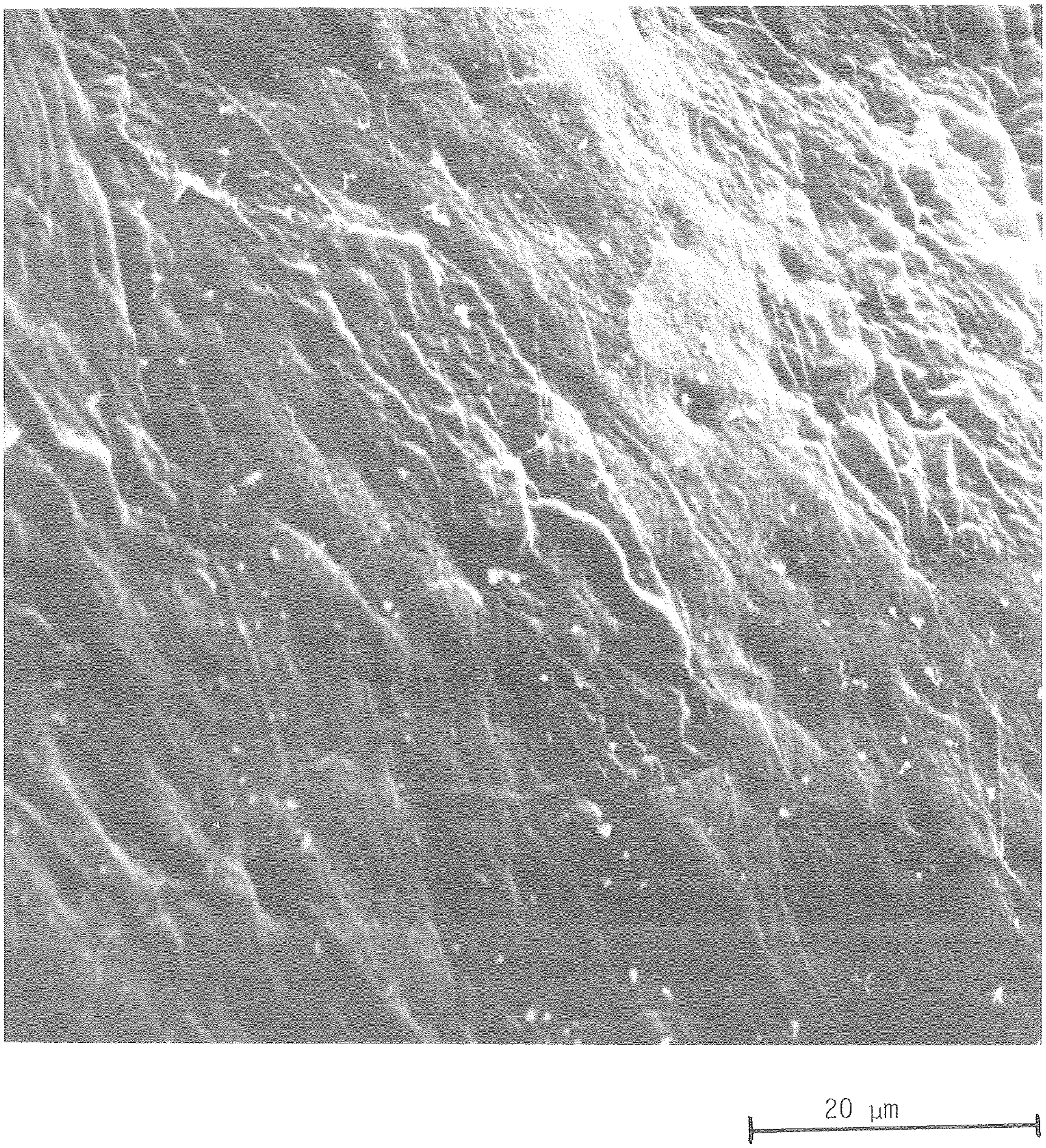

XBB806 7687

Figure 34. SEM micrograph of cornea irradiated with 3 MeV/amu argon particles. Lesion diameter is 5 μm.

XBB790-14737

Figure 35. SEM micrograph of cornea irradiated with 3 MeV/amu argon particles. Lesion diameters measures 5 μm. Note the relative size of nuclei and whole epithelial cells compared to the heavy ion lesions.

VII. ANALYSIS

A. Fluence Correlation

It is essential that we examine the raw data and compute appropriate statistics before stating any firm conclusions. This section displays in tabular format the data for calculated particle fluences, measured particle fluences using plastic, measured membrane lesion concentrations, and measured membrane lesion diameters. These data are quantitated by use of the appropriate statistics which can be found in any statistical analysis textbook (e.g., Dixon and Massey, 1969). The most basic statistical formulae employed here include:

$$\text{arithmetic mean } \bar{X} = \frac{1}{N} \sum_{i=1}^{N} X_i \tag{86}$$

$$\text{variance } S^2 = \frac{1}{N-1} \sum_{i=1}^{N} (X_i - \bar{X})^2 \tag{87}$$

$$\text{standard deviation } S = \left| \sqrt{S^2} \right| \quad , \tag{88}$$

where X_i are the individual measurements and N is the total number of measurements in each data set. Because our data sampling was as random as possible (Section V.C.), our calculated means $\bar{X}$ and variances S^2 will be unbiased estimates of the true means and variances. We assume that the data are distributed normally.

Additionally we will establish 95% confidence levels for every calculated mean, so that the confidence interval will have a 95% likelihood of including the true mean. This calculation is complicated by the fact that we do not know the true standard deviation of any of our data sets, although the calculated standard deviation S is the best estimate of the true standard deviation. To overcome this difficulty, we use the t distribution which is similar to the normal distribution but with greater dispersion. Tables of the t distribution are available in most textbooks of statistical tables (e.g., Fisher and Yates, 1963). With these tables and the calculated standard deviation S we can determine the 95% confidence interval by the expression:

$$95\,\%\text{confidence interval} = \bar{X} \pm t_{N,\alpha} \frac{S}{\sqrt{N}} \qquad (89)$$

where $t_{N,\alpha}$ is a function of the total number of measurements N and the desired level of confidence α. In most cases, $N = 4$, but some data sets have $N = 5$ and $N = 6$. The values of the t distribution which apply are:

$t_{N,\alpha} = 3.18 \quad , \quad N = 4$

$t_{N,\alpha} = 2.78 \quad , \quad N = 5$

$t_{N,\alpha} = 2.57 \quad , \quad N = 6$

Let us proceed to examine the data.

Table 1 displays the measured surface concentrations of membrane lesions for corneas irradiated with carbon, iron, neon, and argon particles. $N = 4$ samples were taken for carbon, iron, and neon irradiations, while $N = 6$ samples were taken for argon. The mean, variance,

Table 1

Trial i	Surface Concentration of Membrane Lesions Carbon 474 MeV (x10^8/cm^2)	Iron 600 MeV (x10^4/cm^2)	Neon 6 MeV (x10^4/cm^2)	Argon 3 MeV (x10^5/cm^2)
1	1.8	0.82	0.83	0.46
2	0.92	0.94	0.68	0.61
3	0.93	1.0	0.70	0.68
4	0.98	0.75	0.79	0.80
5				0.58
6				0.83
	N = 4	N = 4	N = 4	N = 6
Mean X	1.2 x 10^8 cm^{-2}	8.8 x 10^3 cm^{-2}	7.5 x 10^3 cm^{-2}	6.6 x 10^5 cm^{-2}
Variance S^2	1.9 x 10^{15} cm^{-4}	1.3 x 10^6 cm^{-4}	5.1 x 10^5 cm^{-4}	2.0 x 10^{10} cm^{-4}
St. Dev. S	4.3 x 10^7 cm^{-2}	1.1 x 10^3 cm^{-2}	7.2 x 10^2 cm^{-2}	1.4 x 10^5 cm^{-2}
95% Conf. Interval	1.2 ± 0.68 x10^8 cm^{-2}	8.8 ± 1.7 x10^3 cm^{-2}	7.5 ± 1.1 x10^3 cm^{-2}	6.6 ± 1.5 x10^5 cm^{-2}

standard deviation, and 95% confidence interval for each run are also tabulated.

The data in Table 1 were collected with the assumption that errors in measuring areas on electron micrographs were negligible. Is this a fair assumption? The error in measuring areas with a good ruler was less than area ±0.2%. The electron microscope magnification was calibrated with a diffraction grating of known grid spacing placed on the specimen stage and photographed at magnifications used in this work. Moreover, an internal magnification check is possible since the microvilli on the cornea surface are known to have approximately constant diameters of 0.2 micrometers (Pfister, 1973). Thus, squaring the calibrated magnification and dividing that number into the measured micrograph area gives the actual area on the specimen to within ±0.2%. When standard deviations of the mean counts per unit area are on the order of 20% of the mean (see Table 1), the errors introduced in measuring areas are indeed negligible. Consequently, data collection for Table 1 is a problem in counting statistics, and the statistical formulae used here are therefore appropriate.

To evaluate the statistical hypothesis that each cornea membrane lesion is a result of a single heavy ion, we will compare the data in Table 1 for the surface concentration of membrane lesions with the data in Table 2 for the concentration of particle tracks in plastic. More specifically, the means of both populations for the four experiments will be subjected to a statistical test to determine whether to accept or reject the hypothesis that the two means for each experiment represent the same population. We will perform the statistical test following some discussion of data in Table 2.

For those cases discussed in Section VI.C. in which etched plastics were employed, the fluence of the heavy ion beam could be measured directly as shown in Table 2 for carbon and iron. Several determinations were made for each beam fluence simply by counting the surface concentration of etched tracks in different areas of the same plastic. The areas were selected at random but in the central region of irradiation, and the counts per unit area were converted to counts per cm^2 as a measure of the actual heavy ion beam fluence. As mentioned earlier in this section, we assume that the error in measuring areas is negligible compared to the standard deviation of counting. The light microscope employed here was calibrated with a standard calibration slide prepared by Carl Zeiss, Inc.

The fluence of the low energy neon and argon beams was determined by calculation from the measured dose (Section VI.C.). The ionization chamber or secondary electron dosimeters were calibrated with a Faraday cup before each series of experiments, so the doses registered by the dosimeters were taken to be fairly accurate. After any particular run, the dose received by the corneal specimen was recorded and used to calculate the total beam fluence which had irradiated the specimen. Knowing the dose in rads, the stopping power for the particular heavy ion in water σ, and the conversion factor from ergs to electron volts, we can calculate the approximate beam fluence from the equation

Table 2

Trial i	Concentration of Tracks in Plastic Carbon 474 MeV ($x10^8/cm^2$)	Iron 600 MeV ($x10^4/cm^2$)	Neon 6 MeV ($x10^4/cm^2$)	Argon 3 MeV ($x10^6/cm^2$)
1	2.0	0.79		
2	1.6	1.1	No data from plastic	No data from plastic
3	2.3	0.87		
4	0.97	0.95		
5	1.6			
6				
	N = 5	N = 4	N = 1	N = 1
Mean X	1.7×10^8 cm^{-2}	9.3×10^3 cm^{-2}	8.3×10^3 cm^{-2}	8.7×10^5 cm^{-2}
Variance S^2	2.5×10^{15} cm^{-4}	1.8×10^6 cm^{-4}	unknown	unknown
St. Dev. S	5.0×10^7 cm^{-2}	1.3×10^3 cm^{-2}	unknown	unknown
95% Conf. Interval	1.7 ± 0.62 $x10^8$ cm^{-2}	9.3 ± 2.1 $x10^3$ cm^{-2}	unknown	unknown

$$\text{fluence} = \frac{\text{Dose in rads} \times 10^2}{(\sigma \text{ in MeV cm}^2/\text{g})\ (1.602 \times 10^{-6} \text{ erg/MeV})}\ \text{cm}^{-2} \quad . \tag{90}$$

The fluence determined in this way should be correct to within fluence ±20%. The error in equation (90) arises from beam fragmentation, inaccuracies in measuring dose, and inaccuracies in the stopping power term (Howard, 1980). Only one dose measurement was made for each run, so that only a single determination of the beam fluence was possible for neon and argon runs. In particular, the doses for neon and argon were 0.8 rad and 250 rad corresponding to calculated fluences of 8.3×10^3 cm^{-2} and 8.7×10^5 cm^{-2}, respectively. These fluences are entered in the mean row of Table 2 though we realize they are not mean values but single determinations. The other statistical parameters for neon and argon cannot be determined straightforwardly.

We will employ a two-sided test to decide whether pairs of the four experiment populations in Tables 1 and 2 have the same mean. Since the true standard deviations are not known, we again make use of the t distribution and calculate our statistic as

$$t = \frac{\left|\bar{X}_1 - \bar{X}_2\right|}{S_p(1/N_1 + 1/N_2)^{1/2}} \tag{91}$$

where S_p is a pooled root-mean-square estimate of the true standard deviation given by

$$S_p = \frac{\left[(N_1-1)S_1{}^2 + (N_2-1)S_2{}^2\right]^{1/2}}{N_1 + N_2 - 2} \quad .$$

With the data in the tables we compute the statistic t for the four irraidation experiments and obtain the following values:

Carbon $t = 1.6$
Iron $t = 0.6$
Neon $t = 1.0$
Argon $t = 1.4$

In determining the t values for neon and argon we did not need to know values for the standard deviation S from Table 2, since with $N = 1$ that term in the equation for S_p is zero anyway. We establish rejection criteria at a 95% level of confidence by going to the t distribution table (Fisher and Yates, 1963) to set our rejection levels with $N_1 + N_2 - 2$ degrees of freedom. The following rejection levels apply:

Carbon , reject if $t > 2.37$
Iron , reject if $t > 2.45$
Neon , reject if $t > 3.18$
Argon , reject if $t > 2.57$

Since none of the calculated t values exceed the rejection levels, we conclude with a 95% level of confidence that for each of the four experiments the means of the paired populations are the same. With this good agreement between the number of heavy ions per cm^2 and the number of membrane lesions per cm^2

along with the fact that no lesions were found in the 52 non-irradiated controls or the 50 x-ray irradiated samples, we have formidable evidence that a single heavy ion is generating at least one membrane lesion along its track.

B. Lesion Daimeter Correlation with LET

Having established that a corenea membrane lesion is due to a single heavy ion, we can further inquire if the size of the membrane lesion bears a particular relationship to the particle LET. We can address this question with the statistical method of linear regression analysis. Specifically, we will conduct a linear regression of lesion diameter (the dependent variable Y_i) on the LET (the independent variable X_i). For each value of LET we have a population of measurements for lesion diameter, and for each population of lesion diameters we can compute an arithmetic mean $\bar{Y}_x$, variance S^2, and standard deviation S. These data are provided in Table 3.

For a linear regression, the regression curve is defined as an equation for a straight line;

$$\bar{Y}_x = \bar{Y} + b\,(X_i - \bar{X}) \quad , \qquad (92)$$

Table 3

Trial i	Measured Membrane Lesion Diameters Carbon LET=18 keV/μm (μm)	Iron LET=180 keV/μm (μm)	Neon LET=600 keV/μm (μm)	Argon LET=1800 keV/μm (μm)
1	0.085	0.80	2.7	5.4
2	0.064	0.83	2.6	5.0
3	0.084	0.79	2.3	6.1
4	0.077	0.81	2.0	4.7
5	0.084		2.8	4.6
6	0.085			

	N = 6	N = 4	N = 5	N = 5
Mean Y	0.08 μm	0.81 μm	2.5 μm	5.2 μm
Variance S^2	6.9×10^{15} μm^2	0.3×10^{-3} μm^2	0.11 μm^2	0.38 μm^2
St. Dev. S	0.0083 μm	0.017 μm	0.33 μm	0.61 μm
95% Conf. Interval	0.08 ± 0.009 μm	0.81 ± 0.027 μm	2.5 ± 0.41 μm	5.2 ± 0.76 μm

where $\overline{Y}_x$ is the mean lesion diameter at a particular value of LET, $\overline{Y}$ is the mean of all measured values of lesion diameter, X_i is the particular LET of interest, $\overline{X}$ is the mean of all LET values, and b is the line slope given by (Dixon and Massey, 1969)

$$b = \frac{\Sigma X_i Y_i - \Sigma X_i \Sigma Y_i / N}{\Sigma X_i{}^2 - (\Sigma X_i)^2 / N} \quad , \tag{93}$$

and N here equals the number of Y_i. For this work there are four values of LET: 18, 180, 600, and 1800 keV/μm. The values of lesion diameter are in Table 3, and we observe that N = 20. Let us compute the appropriate sums.

For LET	For Lesion Diameters
$\Sigma X_i = 12{,}828$	$\Sigma Y_i = 41.91$
$\Sigma X_i^2 = 18,\ 131,\ 544$	$Y_i^2 = 168.45$
$\overline{X} = 641.4$	$\overline{Y} = 2.10$

$$\Sigma X_i Y_i = 54,\ 470.02$$

$$N = 20$$

These values permit a calculation of the regression line slope b from equation (93) as

$$b = \frac{54{,}470.02 - (12{,}828)(41.91)/20}{18{,}131{,}544 - (12{,}828)^2/20} = 2.8 \times 10^{-3} \quad .$$

We can now write equation (92) as our regression line

$$\bar{Y}_X = 2.10 + (2.8 \times 10^{-3})(X_i - 641.4) \quad . \qquad (94)$$

Substitution of the four values of LET (X_i) into equation (94) yields the four values for mean lesion diameters which occur on the regression line at the four LET values:

LET (X_i)	Mean Lesion Diameter ($\bar{Y}_X$)
18 keV/μm	0.36 μm
180	0.81
600	2.0
1800	5.3

By comparing these calculated regression values with the measured values in Table 3, we realize that at the 95% level of confidence our statistical test for a linear relationship between LET and lesion diameter has failed. Consequently, the linear regression analysis allows us to conclude that we do not have sufficient evidence for the statistical hypothesis that lesion diameter increases linearly with particle LET.

To help summarize the data presented in this and the previous sections, Fig. 36 is a simplified tabulation. The numbers in Fig. 36 are rounded for easier presentation. The particle velocity values in the summary table were calculated from equation (68).

C. The Meaning of Dose

The units used to express energy deposition in matter by the action of ionizing radiation of any type are the gray and the rad:

1 gray = 100 rad
1 rad = 100 erg/g.

These dose units express the amount of energy deposited in a unit mass of material (or unit volume of material when multiplied by the material density) and are macroscopic quantities. We have seen from this research that for heavy ion irradiation of biological tissue a macroscopic measure of dose can be misleading. The dose to biological tissues by heavy ions is a highly complicated microscopic phenomenon with adjacent microdomains of high and low energy deposition (Luxton, et al, 1979). We should, therefore, avoid using macroscopic units in describing this microscopically inhomogeneous phenomenon (Grahn, 1973).

Heavy Ion	Energy $\frac{\text{MeV}}{\text{amu}}$	LET $\frac{\text{keV}}{\mu}$	Relative	Charge Q	Velocity $V \times 10^{10}$ cm/sec	Q^2/V^2 $\times 10^{-20}$	Relative	Lesion diameter μ	Relative
CARBON	474	18	1	6	2.25	7.1	1	0.08	1
IRON	600	180	10	26	2.4	117	16	0.8	10
NEON	6	600	33	8.7	0.52	280	39	2.5	31
ARGON	3	1800	100	15.6	0.52	832	117	5	63

XBL807-3446

Figure 36. Summary table of data for heavy ion irradiation of corneas with information on subsequent lesion formation. Note a somewhat linear relationship between LET and lesion diameter.

VIII. DISCUSSION

A. The Time Scale of Phenomena

The time scale of radiobiological events is of particular importance in studying radiation damage to biological tissue, since living tissue is constantly in a state of flux. Radiation damage will have differing manifestations depending on the time after the initial energy deposition at which the tissue is examined, and of course the method of examination will govern the nature of the revealed damage. SEM in the secondary electron mode of operation gives us information on the 3-dimensional configuration of surfaces; thus SEM is an appropriate tool for examining the morphological alterations occurring in tissues following heavy ion irradiation. But we must realize that any observed damage is at best a picture of surface morphology at the time the specimen is chemically fixed; we cannot easily extrapolate to predict how the damage would appear at any other time unless we fully understand the time frame in which various modifying mechanisms operate. We must also know how our specimen preparation techniques modify the radiation damage before we can quantitate the problem.

To help elucidate this complex situation, Fig. 37 shows a time scale ranging from 10^{-18} seconds to 10^{12} seconds displaying some of the known radiobiological events in their approximate time domains. The corneal samples examined in this work were all chemically fixed at about ten seconds post-irradiation. We see from Fig. 37 that all sorts of radiation damage modifying events have already transpired: initial energy deposition, decay to vibrational and rotational states,

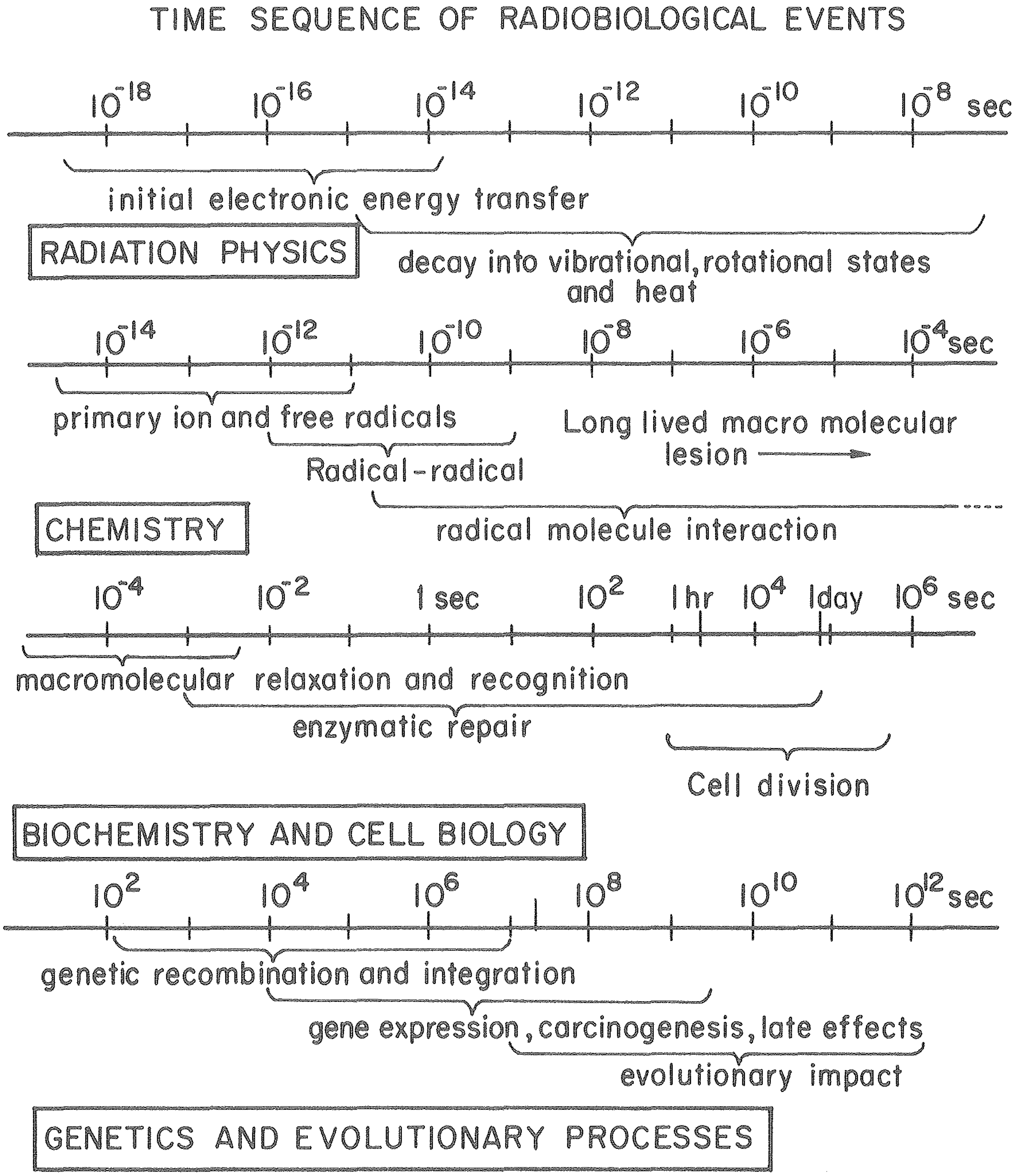

XBL793-3312

Figure 37. Time sequence of radiobiological events. (Tobias, et al, 1980).

thermalization, primary ion interactions, free radical generation and interactions, macromolecular lesion formation, and enzymatic repair. The morphological manifestation of radiation damage at ten seconds represents a composite and presently incalculable product of all these radiobiological mechanisms. In this work we discussed only diffusion, Section III.A.2., in order to explain one mechanism by which energy structure in a heavy ion track is modified in a fluid system. We have not given a comprehensive picture of track formation in biological tissue prior to the 10 second point, but have have shown qualitatively that heavy ions do generate morphologically observable membrane lesions along their tracks which are fixed at that time. The fate of such membrane lesions and their effects in living biological tissues remain to be explored.

B. Lesion Size vs. Core and Penumbra Calculations

In Section III.A.2. we discussed several theories for the energy structure of a heavy ion track. One issue on which the track theories had good agreement concerned the approximate diameters of particle track cores and penumbras. The consensus from the literature was that in general for energetic heavy ions, the core diameters were on the order of nanometers and the penumbra diameters were on the order of micrometers (Brandt and Ritchie, 1974; Magee and Chatterjee, 1977, 1979, 1980). The data from Section VII.B. in Table 3 suggest that the membrane lesions are too large to derive directly from core energy densities but are similar in diameter to particle track penumbras. The membrane lesion diameters therefore may reflect the extent to which delta rays radially penetrated the plasma membrane. But in addition to the initial energy deposition from delta rays, several other mechanisms could increase the lesion diameter prior to chemical fixation as mentioned in the previous section.

C. Holes and Dents

Two types of heavy ion induced corneal epithelium plasma membrane lesions were illustrated in the data, holes and dents (Figs. 22-35). The holes always occurred for Bragg plateau or low LET heavy ion irradiation, and the dents arose from Bragg peak or high LET particles. It is not known why this situation prevails. Perhaps the membrane holes result from chemical action during sample preparation (see the following Section). A close examination of the membrane holes discloses that each hole is bounded by an annulus or slight swelling of the plasma membrane around the perimeter of the hole. Each hole passes completely through the plasma membrane to the cytoplasm, so that the lesion constitutes a missing patch of membrane. The only conceivable way a membrane hole could persist requires solidification of the membrane near the hole; otherwise, any hole should rapidly reseal.

D. Chemical Amplification

Standard EM chemical fixation protocols for biological tissue often involve the use of osmium tetroxide as a primary fixative or as a post-fixative following pre-fixation with aldehydes (Karnovsky, 1965). It is thought that osmium tetroxide predominantly crosslinks membrane unsaturated lipids at the sites of double bonds while aldehydes, in particular glutaraldehyde, predominantly crosslink cell proteins (Litman and Barrnett, 1972). The chemical fixation protocol employed in this work did not use osmium tetroxide but relied upon glutaraldehyde as the only chemical fixative (Section V.F.1.). We might expect then, that the epithelial plasma membrane proteins were tethered by glutaraldehyde but the membrane lipids were either poorly fixed or not fixed at all. Because lipids interact locally with membrane proteins, it is possible that lipids are fixed indirectly by their attachment to proteins which have been crosslinked.

As a heavy ion strikes the membrane surface leaving an energy deposit along its track, it seems likely that large membrane proteins in the vicinity of the particle track will become fragmented (Butts and Katz, 1967). Supposing that fragmented proteins are less efficiently fixed by glutaraldehyde than intact proteins, then following chemical fixation those regions corresponding to the particle track will be unstable compared to the surrounding membrane material. In this way, the track region could become predisposed to undergo morphological change during subsequent preparation procedures.

After chemical fixation the corneal samples were dehydrated in ethanol and critical point dried in liquid CO_2 (Section V.F.2. and 3.). Both ethanol and liquid CO_2 can dissolve lipids, so that during sample dehydration and drying the lipids in the particle track will be preferentially extracted. This process would give rise to morphologically distinguishable membrane lesions, including holes.

It is suggested that heavy ion lesions in corneal plasma membranes become visible for SEM after chemical etching during sample preparation. This is reminiscent of track detection in plastics by chemical etching. Although the track diameter in plastics is often altered during chemical fixation, much basic radiological data has come from the use of etched plastics (Fleischer, 1975). It is hoped that a similar outcome will apply to the membrane lesions even though we realize that chemical amplification has probably taken place.

IX. CONCLUDING REMARKS

A. Summary

This work demonstrates that heavy ion irradiation of biological tissue causes microstructural damage to plasma membranes. Since the surface concentration of membrane lesions was always in agreement with the irradiating heavy ion beam fluence, it is clear that each heavily ionizing particle is capable of generating a membrane lesion and that each lesion can be visualized by SEM following fixation at 10 seconds post irradiation. The amount of energy deposited locally in the particle track, as measured by LET, was not linearly proportional to the ensuing membrane lesion diameter, but lesion size did increase with LET. These lesions were not observed in non-irradiated controls or x-ray irradiated samples, and it is concluded that lesion formation is both peculiar to and characteristic of heavy ion irradiation of biological tissues.

B. Importance and Ramifications

This work is not the only line of research which indicates that heavy ions leave tracks in biological tissue. A very recent study has shown that opacifications in the lense of the eye correspond to a delayed effect of heavy ion radiation tracks (Worgul, 1979). Studies on the irradiated drosophilla brain in cross section yield evidence that heavy ions generate tracks of vacuoles inside neural cells (Miquel, 1979). But the data presented here for heavy ion irradiation of rat corneal epithelium probably constitute the most convincing argument that a single heavy ion can produce a single lesion in biological tissue. This finding is not surprising if we temper our thinking with the theoretical underpinnings of Section III.A.2., and yet the finding meets with considerable skepticism. This attitude is both a precautionary measure and a potential danger.

If this work is eventually verified by other workers to the extent that the track effect becomes "established," then we will have to reconsider the risk factors involved in subjecting humans to medical treatment by heavy ions or exposing humans to cosmic rays in space. We will also be forced to measure radiation dose by heavy ions in a way which accounts for the microdose distributions in living tissues.

APPENDIX A

The equation of a hyperbola is central to the discussion on Rutherford's scatter formula, so let us proceed through this basic formulation. In rectangular coordinates the equation of a hyperbola is

$$\frac{X^2}{a^2} - \frac{y^2}{c^2 - a^2} = 1 \qquad \text{(A1)}$$

where

$$a^2 = \frac{1}{4} \left\{ \left[(x - c)^2 + y^2\right]^{1/2} - \left[(x + c)^2 + y^2\right]^{1/2} \right\}^2 . \qquad \text{(A2)}$$

Figure A1 will help clarify the interpretation of these equations. Refer to this figure for the notation used here. The length of line segment r' is

$$r' = \left[(x - c)^2 + y^2\right]^{1/2} \qquad \text{(A3)}$$

and the length of line segment r is

$$r = \left[(x + c)^2 + y^2\right]^{1/2} . \qquad \text{(A4)}$$

The difference between line segments r' and r at any point on the hyperbola is always equal to ± 2a (Johnson and Kiokemeister, 1965):

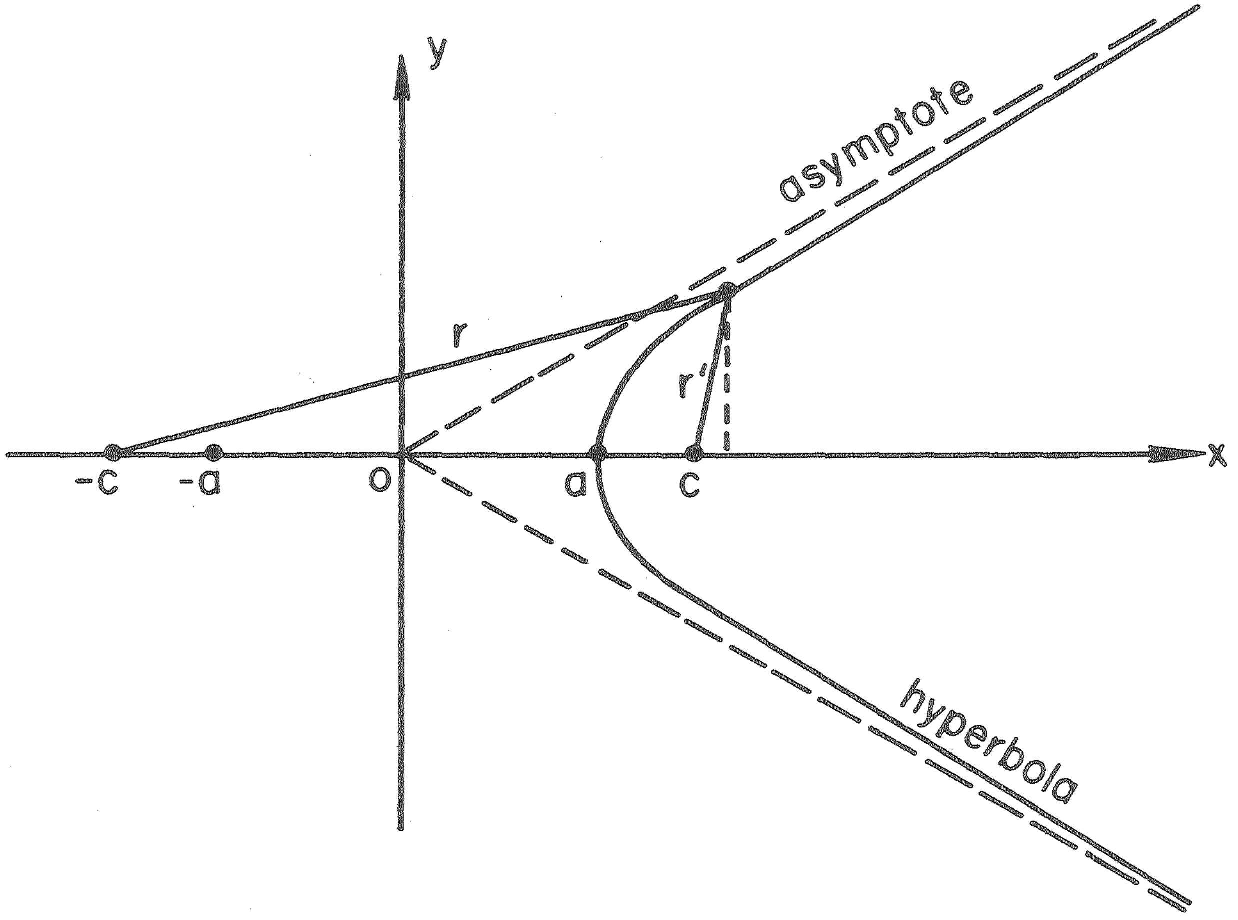

XBL806-3405

Figure A1. The hyperbola in rectangular coordinates showing distances r and r', the foci -C and C, and vertices -a and a. Only the right hyperbola is shown.

$$\pm 2a = r' - r \quad . \tag{A5}$$

Substitution of equations (A3) and (A4) into equation (A5) and squaring both sides yields equation (A2). The points at $-c$ and c on the x-axis are called the foci of the hyperbola, the zero point of the coordinates is called the center, and the points at $-a$ and a are called the vertices. Oftentimes equation (A1) is written as an explicit function of y

$$y = \pm \frac{b}{a} \left(x^2 - a^2\right)^{1/2} \tag{A6}$$

where

$$b = \left(c^2 - a^2\right)^{1/2} \quad . \tag{A7}$$

At this point it is convenient to change from rectangular to polar coordinates, and this is accomplished by substitution in equation (A1) of

$$x = r \cos\theta$$

and $y = r \sin\theta$.

Figure A2 illustrates the hyperbola in polar coordinates and defines the angle θ. The equation for the hyperbola can also be found

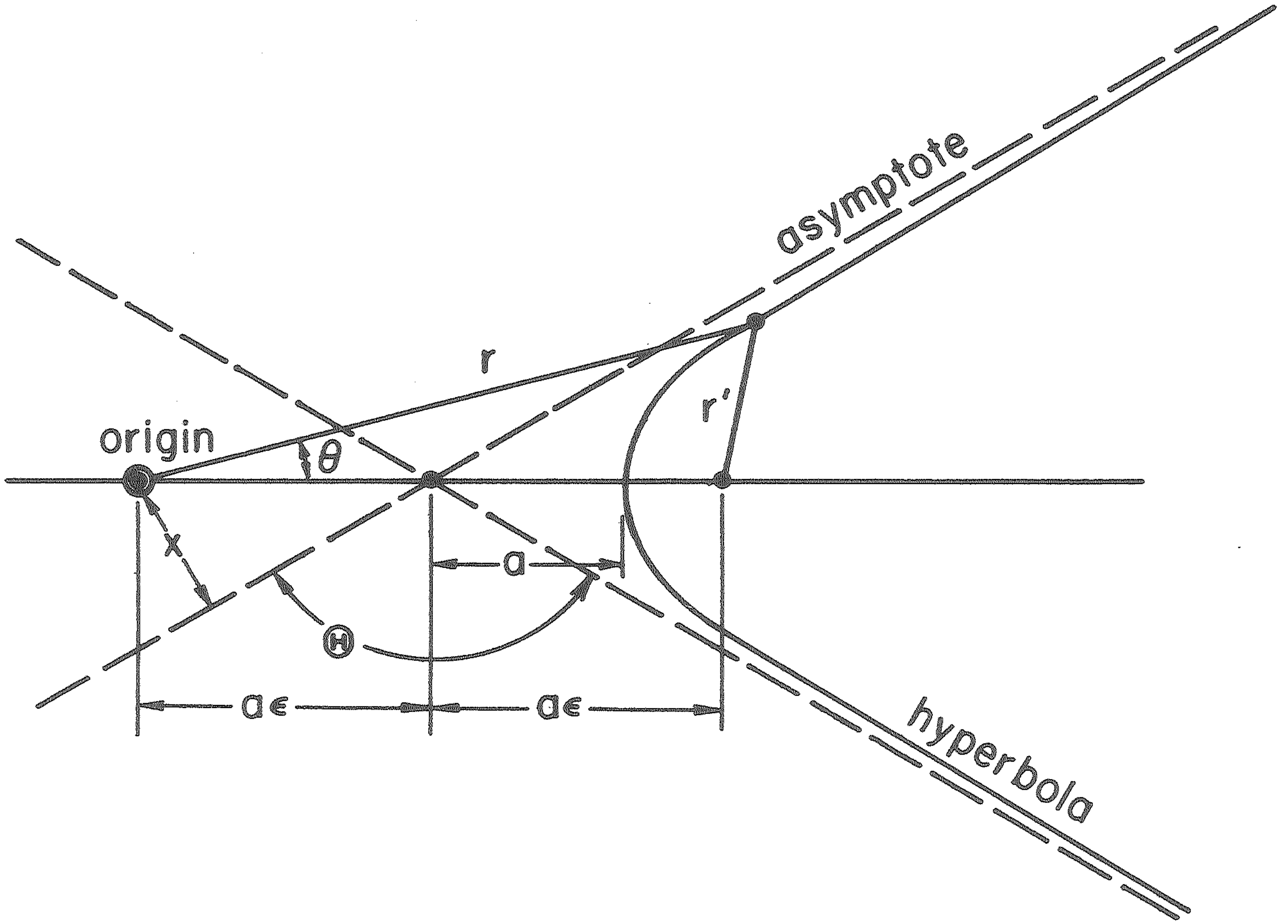

XBL806-3406

Figure A2. The hyperbola in polar coordinates showing the distances r and r', the vertex a, the foci aε, and the deflection angle Θ. Only the right hyperbola is shown.

directly from Fig. A2 rather than laboriously working through the substitution suggested above by remembering that

$$\pm 2a = r' - r \quad .$$

Upon rearranging terms to solve for r' we have two equations

$$r' = r - 2a \tag{A8}$$

and $r' = r + 2a$. (A9)

Equations (A8) and (A9) can be squared to give, respectively,

$$(r')^2 = r^2 - 4ar + 4a^2 \tag{A10}$$

and $(r')^2 = r^2 + 4ar + 4a^2$. (A11)

The law of cosines from Fig. A2 is

$$(r')^2 = r^2 + (2a\varepsilon)^2 - (2r)(2a\varepsilon)\cos\theta \tag{A12}$$

and this expression pertains only to the hyperbola defined by equation (A8) which is the right hyperbola shown in Fig. A2. The left hyperbola which is not shown is defined by equation (A9) and has the law of cosines given by

$$(r')^2 = r^2 + (2a\varepsilon)^2 + (2r)(2a\varepsilon)\cos\theta \quad . \tag{A13}$$

Equations (A10) and (A12) and equations (A11) and (A13) can be equated to eliminate $(r')^2$ and upon rearrangement yield, respectively,

$$\text{right hyperbola, } r = \frac{a(1 - \varepsilon^2)}{1 - \varepsilon\cos\theta} \tag{A14}$$

$$\text{left hyperbola, } r = \frac{a(\varepsilon^2 - 1)}{1 - \varepsilon\cos\theta} = \frac{-a(1 - \varepsilon^2)}{1 - \varepsilon\cos\theta} \quad . \tag{A15}$$

The hyperbola approaches the asymptotes at $r = \infty$, and this occurs at an angle which makes the denominators of equations (A14) or (A15) approach zero

$$\cos\theta_\infty = \frac{1}{\varepsilon} \tag{A16}$$

or $\theta_\infty = \cos^{-1}(1/\varepsilon)$

where ε is called the eccentricity.

The hyperbola of Fig. A2 and equation (A14) will be shown in part III.A.1. to correspond to the trajectory of a charged particle during an elastic collision with a particle of the same signed charge: the right hyperbola is for the repulsive coulombic force. Equation (A15) will similarly be shown to correspond to the trajectory of a charged particle during an elastic collision with a particle of the opposite signed charge: the left hyperbola is for the attractive coulombic force.

REFERENCES

1. Barkas, W. H. and Berger, M. J., (1964), Tables of Energy Losses and Ranges of Heavy Charged Particles, NASA SP-3013, NTID, Washington, D. C.
2. Beatrice, E. S., (1980), Letterman Research Center, San Francisco, California, private commuinication.
3. Behrnetz,S., (1976), Application of Track Formation Theory to Calibration of Photometric Measurements on Cosmic Ray Tracks in Nuclear Emulsion, Nucl. Inst. and Meth., 133:113.
4. Berger, M. J. and Seltzer, S. M., (1966), Additional Stopping Power and Range Tables for Protons, Mesons, and Electrons, NASA SP-3036, NTID, Washington, D. C.
5. Bethe, H. A., (1930), Ann. Physik, 5:325.
6. Bevatron/Bevalac Users Handbook, (1977), Division of Biology and Medicine, Lawrence Berkeley Laboratory, Berkeley, California.
7. Blass, G. A., (1962), Theoretical Physics, Ch. 7, Meredith Publishing Co., New York.
8. Bloch, F., (1933a), Ann. Physik, 16:285.
9. Bloch, F., (1933b), Z. Physik, 81:363.
10. Blumcke, S. and Morgenroth, K., (1967), The Stereo Ultrastructure of the External and Internal Surface of the Cornea, J. Ultrastruct. Res., 18:502.
11. Bohr, N., (1913a), On the Theory of the Decrease of Velocity of Moving Electrified Particles on Passing Through Matter, Phil. Mag., 25:10.

12. Bohr, N., (1913b), On the Constitution of Atoms and Molecules, Phil. Mag., 26:1.

13. Bohr, N., (1915), On the Decrease of Velocity of Swiftly Moving Electrified Particles in Passing Through Matter, Phil. Mag., 30:581.

14. Boyd, A., (1978), Pros and Cons of Critical Point and Freeze Drying for SEM, SEM, 2:303.

15. Brandt, W. and Ritchie, R. H., (1974), Physical Mechanisms in Radiation Biology, CONF-721001, NTIS, U. S. Dept. of Commerce, Virginia.

16. Butts, J. J. and Katz, R., (1967), Theory of RBE for Heavy Ion Bombardment of Dry Enzymes and Viruses, Rad. Res., 30:855.

17. Chase, G. D. and Rabinowitz, J. L., (1967), Principles of Radioisotope Methodology, 3rd ed., Ch 7, Burgess Publishing Co., Minnesota.

18. Chatterjee, A., Maccabee, H. D., and Tobias, C. A., (1973), Radial Cutoff LET and Radial Cutoff Dose Calculations for Heavy Charged Particles in Water, Rad. Res., 54:479.

19. Crewe, A. V., (1971), A High Resolution Scanning Electron Microscope, Scientific American, 224(4):26.

20. Diamond, M. C., (1980), Neuro-Anatomy Dept., U. C. Berkeley, private communication.

21. Dixon, W J. and Massey, F. J., (1969), Introduction to Statistical Analysis, 3rd ed., McGraw-Hill Book Co., New York.

22. Evans, R. D., (1955), The Atomic Nucleus, Ch. 18, 22, and Appendix B, McGraw-Hill Book Co., Inc., New York.

23. Everhart, T. E., Herzog, R. F., Chung, M. S., and Devore, W. J., (1972), Electron Energy Dissipation Measurements in Solids, Proceedings of the Sixth International Conference on x-ray Optics and Microanalysis, Univ. of Tokyo Press, Japan.

24. Fisher, R. A. and Yates, F., (1963), Statistical Tables for Biological, Agricultural and Medical Research, 6th ed., Oliver and Boyd Ltd., London.

25. Fleischer, R. L., Price, P. B., and Walker, R. M., (1975), Nuclear Tracks in Solids, U. C. Press, California.

26. Fowles, G. R., (1962), Analytical Mechanics, Ch. 8, Holt, Rinehart and Winston, New York.

27. Freeman, R. D. and Lai, C. E., (1978), Development of the Optical Surfaces of the Kitten Eye, Vision Res., 18:399.

28. Garcia, J. D., (1969), Ejected Electron Distributions, Phys. Rev., 177:223.

29. Gasiorowicz, S., (1974), Quantum Physics, Ch. 24 and 25, John Wiley and Sons, Inc., New York.

30. Glaser, D. A. and Rahm, D. C., (1955), Characteristics of Bubble Chambers, Phys. Rev., 97:474.

31. Glaser, D. A., Rahm, D. C., and Dodd, C., (1956), Bubble Counting for the Determination of the Velocities of Charged Particles in Bubble Chambers, Phys. Rev., 102:1653.

32. Goldstein, J. I., (1975), Electron Optics, Ch. 2, and Beam-specimen Interaction, Ch. 3, Practicle Scanning Electron Microscopy, Plenum, New York.

33. Grahn, D., ed., (1973), HZE Particle EFfects in Manned Space Flight, Space Committee, Nat. Acad. Sci., New York.

34. Hasegan, D., Apostol, A., and Nicolae, M., (1978), Track Width of Slow Heavy Ions in Nuclear Emulsion by Photometric Measurements, Nucl. Track Det., 2:141.

35. Hayes, T. L., (1973), Scanning Electron Microscopy Techniques in Biology, in Advanced Techniques in Biological Electron Microscopy, ed. by Koehler, J. K., Springer-Verlag, New York.

36. Henriksen, T., (1966), Production of Free Radicals in Solid Biological Substances by Heavy Ions, Rad. Res., 27:676.

37. Howard, J., (1980), LBL Biomedical Division, personal communication.

38. Jensen, M. and Mathieson, O., (1976), Measured and Calculated Absorptance of Tracks of Fast Heavy Ions in Ilford G5 Nuclear Emulsion, Physica Scripta, 13:75.

39. Jensen, M., Larsson, L., Mathieson, O., and Rosander, R., (1976), Experimental and Theoretical Absorptance Profiles of Tracks of Fast Heavy Ions in Nuclear Emulsion, Physica Scripta, 13:65.

40. Johnson, R. E. and Kiokemeister, F. L., (1965), Calculus with Analytic Geometry, 3rd ed., Allyn and Bacon, Inc., Massachusetts.

41. Kahn, D., (1953), Phys. Rev., 90:503.

42. Karnovsky, M. J., (1965), A Formaldehyde-Glutaraldehyde Fixative of High Osmolality for Use in Electron Microscopy, J. Cell Bio., 27:137A.

43. Katz, R. and Kobetich, E. J., (1968), Formation of Etchable Tracks in Dielectrics, Phys. Rev., 170:401.

44. Katz, R. and Kobetich, E. J., (1969), Particle Tracks in Emulsion, Phys. Rev., 186:344.

45. Katz, R., Sharma, S. C., and Homayoonfar, M., (1972), Nucl. Instr. Methods, 100:13.

46. Katz, R. and Butts, J. J., (1965), Phys. Rev., 137:B198.

47. Kobetich, E. J. and Katz, R., (1968a), Phys. Rev., 170:391.

48. Kobetich, E. J. and Katz, R., (1968b), Phys. Rev., 170:405.

49. Kobetich, E. J. and Katz, R., (1969), Nucl. Instr. Methods, 71:226.

50. Litman, R. B. and Barrnett, R. J., (1972), The Mechanism of the Fixation of Tissue Components by Osmium Tetroxide via Hydrogen Bonding, J. Ultra. Res., 38:63.

51. Luxton, G., Fessenden, P., and Hoffmann, W., (1979), Microdosimetric Measurements of Pretherapeutic Heavy Ion Beams, Rad. Res., 79:256.

52. Lyman, J. T., (1967), in Biomedical Studies with Heavy Ion Beams, UCRL-17357, NTIS, U. S. Dept. of Commerce, Virginia.

53. Magee, J. L. and Chatterjee, A., (1977), in Biological and Medical Research with Accelerated Heavy Ions at the Bevalac, LBL-5610, NTIS, U. S. Dept. of Commerce, Virginia.

54. Magee, J. L. and Chatterjee, A., (1979), Chemical Track Effects in Condensed Systems and Implications for Biological Damage, presented at the International Congress of Radiation Research, Japan.

55. Magee, J. L. and Chatterjee, A., (1980), Radiation Chemistry of Heavy Ion Tracks, Part 1, J. Phys. Chem., in press.

56. Malachowski, M. J., (1978), The Effects of Ionizing Radiation on the Light Sensing Elements of the Retina, PhD. Dissertation, LBL-5683, Lawrence Berkeley Laboratory, California.

57. Mamoon, A. M., (1969), Effects of Ionizing Radiations on Myelin Formation in Rat Brain Cultures, PhD. Dissertation, UCRL-19481, Lawrence Berkeley Laboratory, California.

58. Miquel, H., (1979), Microlesions Induced in Drosophilla Brain by Single Hits of 10 MeV Krypton, Mini-Lesion Symposium, presented at LBL, Nov. 8.

59. Mozumder, A. and Magee, J. L., (1972), Radiation Chemistry in Condensed Phases, in Physical Chemistry: An Advanced Treatise, Ch. 13, COO-38-877, NTIS, U. S. Dept. of Commerce, Virginia.

60. Nagle, D. E., Hildebrand, R. H., and Plano, R. J., (1956), Hydrogen Bubble Chamber Used for Low-Energy Meson Scattering, Rev. Sci. Inst., 27:203.

61. Nikolaev, V. S. and Dmitriev, I. S., (1968), On the Equilibrium Charge Distribution in Heavy Ion Beams, Phys. Let., 28A:277.

62. Northcliffe, L. C. and Schilling, R. F., (1970), Range and Stopping-Power Tables for Heavy Ions, Nuclear Data Tables, A7:233, Academic Press, New York.

63. O'Loughlin, G., (1980), AMRAY Inc., Massachusetts, private communication dated 07/01/80.

64. Paretzke, H. G., (1979), Track Structure Calculations and Their Accuracy, presented at the International Congress of Radiation Research, Japan.

65. Parsons, D. F., (1970), Some Biological Techniques in Electron Microscopy, Ch. 1, Academic Press, New York.

66. Pfister, R. R., (1973), The Normal Surface of Corneal Epithelium: a Scanning Electron Microscope Study, Invest. Ophthalmo., 12:654.

67. Pierce, T. E. and Blann, M., (1968), Phys. Rev., 173:390.

68. Pless, I. A. and Plano, R. J., (1956), Negative Pressure Isopentane Bubble Chamber, Rev. Sci. Inst., 27:935.

69. Plesset, M. S. and Zwick, S. A., (1952), A Nonsteady Heat Diffusion Problem with Spherical Symmetry, J. App. Phys., 23:95.

70. Plesset, M. S. and Zwick, S. A., (1954), The Growth of Vapor Bubbles in Superheated Liquids, J. App. Phys., 25:493.

71. Pomerantz, M. A., (1971), Cosmic Rays, Ch. 3, Van Nostrand Reinhold Co., New York.

72. Raybourn, M. S., (1979), Lawrence Berkeley Laboratory, California, private communication.

73. Richtmyer, F. K., Kennard, E. H., and Cooper, J. N., (1969), Introduction to Modern Physics, McGraw-Hill Book Co., New York.

74. Ritchie, R. H., Hamm, R. N., Turner, J. E., and Wright, H. A., (1978), The Interaction of Swift Electrons with Liquid Water, paper presented in Brussels, Oak Ridge National Laboratory Publication, Tennessee.

75. Rutherford, E., (1906a), Phil. Mag., 11:166.

76. Rutherford, E., (1906b), Phil. Mag., 12:134.

77. Segre, E., ed., (1959), Experimental Nuclear Physics, Part 2, John Wiley and Sons, New York.

78. Seitz, F., (1958), On the Theory of the Bubble Chamber, Phys. Fluids, 1:2.

79. Setlow, R. B. and Pollard, E. C., (1962), Molecular Biophysics, Ch. 10, Addison-Wesley Publishing Co., Inc., Massachusetts.

80. Silk, E.C.H. and Barnes, R. S., (1959), Phil. Mag., 4:970.

81. Spencer, W. H. and Hayes, T. L., (1970), Scanning and Transmission Electron Microscopic Observations of the Topographic Anatomy of Dendritic Lesions in the Rabbit Cornea, Invest. Ophthalmo., 9:183.

82. Spiegel, M. R., (1967), Applied Differential Equations, Ch. 2, Prentice-Hall, Inc., New Jersey.

83. Tobias, C. A., Alpen, E. A., Blakely, E. A., Castro, J. R., Chatterjee, A., Chen, G.T.Y., Curtis, S. B., Howard, J., Lyman, J. T., and Ngo, F.Q.H., (1979a), Radiobiological Basis for Heavy-ion Therapy, in Treatment of Radioresistant Cancers, Elsevier/North-Holland Biomedical Press, Netherlands.

84. Tobias, C. A., Benton, E. V., and Capp, M. P., (1978), Heavy Ion Radiography, in Recent Advances in Nuclear Medicine, Volume 5, Chapter 3, Grune and Stratton, Inc., New York.

85. Tobias, C. A., Chatterjee, A., Malachowski, M. J., Blakely, E. A., and Hayes, T. L., (1979b), Tracks in Condensed Systems, presented at the International Congress of Radiation Research, Japan.

86. Tobias, C. A., Blakely, E. A., Ngo, F.Q.H., and Yang, T.C.H., (1980), The Repair-Misrepair Model of Cell Survival, in Radiation Biology in Cancer Research, Raven Press, New York.

87. Wheeler, J. A. and Ladenburg, R., (1941), Phys. Rev., 60:754.

88. Williams, E. J., (1945), Revs. Mod., Phys., 17:217.

89. Williamson, C. and Boujot, J. P., (1962), Tables of Range and Rate of Energy Loss of Charged Particles of Energy 0.5 to 150 MeV, Rapport CEA No. 2189, Centre D'Etudes Nucleaires De Saclay, Premier Ministre Commissarait A L'Energie Atomique, France.

90. Wilson, J. G., (1951), The Principles of Cloud-Chamber Technique, Ch. 1, 2, and 7, Cambridge University Press, England.

91. Wilson, C.T.R., (1897), Philos. Trans., 189:265.

92. Wilson, C.T.R., (1899), Philos. Trans. 192:403.

93. Worgul, B., (1979), Recent Progress on Lense Effect from Argon Particles, Mini-Lesion Symposium, presented at LBL, Nov. 8.